Stability of antigorite serpentinite and geochemical exchange with oceanic crustal rocks during ultrahigh-pressure subduction-zone metamorphism (Lago di Cignana Unit, Italian Western Alps)

Mattia Gilio, Marco Scambelluri, Samuele Agostini, Marguerite Godard, Daniel Peters, Thomas Pettke

To cite this version:

Mattia Gilio, Marco Scambelluri, Samuele Agostini, Marguerite Godard, Daniel Peters, et al.. Stability of antigorite serpentinite and geochemical exchange with oceanic crustal rocks during ultrahigh-pressure subduction-zone metamorphism (Lago di Cignana Unit, Italian Western Alps). Journal of Petrology, 2019, 60 (6), pp.1229-1262. 10.1093/petrology/egz030 . hal-02349539

HAL Id: hal-02349539

https://hal.umontpellier.fr/hal-02349539v1

Submitted on 6 Nov 2020

Stability of antigorite serpentinite and geochemical exchange with oceanic crustal rocks during ultrahigh–pressure subduction–zone metamorphism (Lago di Cignana Unit, Italian Western Alps)

Journal:	*Journal of Petrology*
Manuscript ID	Draft
Manuscript Type:	Original Manuscript
Date Submitted by the Author:	n/a
Complete List of Authors:	Gilio, Mattia; Universita degli Studi di Genova Dipartimento di Scienze della Terra dell'Ambiente e della Vita; Universita degli Studi di Pavia Dipartimento di Scienze della Terra e dell Ambiente Scambelluri, Marco; University of Genova, Dipartimento di Scienze della Terra dell'Ambiente e della Vita Genova Agostini, Samuele; Istituto di Geoscienze e Georisorse, Consiglio Nazionale delle Ricerche (CNR), Via Moruzzi, 1, 56124 Pisa, Italy Godard, Marguerite; CNRS, Géosciences Montpellier, Université de Montpellier Peters, Daniel; University of Bern, Institute of Geological Sciences; Institut de Recherche en Astrophysique et Planetologie Pettke, Thomas; University of Bern, Institute of Geological Sciences
Keyword:	subduction, serpentinite, oceanic crust, ultrahigh-pressure metamorphism, fluid-rock exchange, element transfer, Lago di Cignana, Ti-chondrodite

Stability of antigorite serpentinite and geochemical exchange with oceanic crustal rocks during ultrahigh–pressure subduction–zone metamorphism (Lago di Cignana Unit, Italian Western Alps).

Mattia Gilio[1,2*], Marco Scambelluri[1,3], Samuele Agostini[3], Marguerite Godard[4], Daniel Peters[5,6], Thomas Pettke[5]

[1]Dipartimento di Scienze della Terra e dell'Ambiente e della Vita, Università degli Studi di Genova, corso Europa 26, 16132 Genova, Italy

[2]Dipartimento di Scienze della Terra e dell'Ambiente, Università degli Studi di Pavia, via Ferrata 1, 27100 Pavia, Italy

[3]Instituto di Geoscienze e Georisorse, Consiglio Nazionale delle Ricerche, via Moruzzi 1, 56124 Pisa, Italy

[4]Géosciences Montpellier, Université Montpellier 2, cc60, Place Bataillon, 34095 Montpellier, France

[5]Institute of Geological Sciences, University of Bern, Baltzerstrasse 3, 3012 Bern, Switzerland

[6]Institut de Recherche en Astrophysique et Planétologie, Observatoire Midi-Pyrénées, 14 Avenue Belin, 31400 Toulouse, France

Keywords

Subduction; serpentinite; oceanic crust; ultrahigh-pressure metamorphism; fluid-rock exchange; element transfer; Lago di Cignana; Ti-chondrodite

Abstract

The Lago di Cignana Unit is a coesite– and diamond–bearing ophiolite recording Alpine ultrahigh–pressure (UHP) metamorphism at 600 °C–3.2 GPa (~110 km depth). This Unit is tectonically sandwiched between two ophiolitic slices: the eclogitic Zermatt–Saas Zone (540 °C–3.2 GPa) and the blueschist Combin Zone (400 °C–0.9 GPa) along a tectonic structure joining high–pressure (HP) units recording a ~1.2 GPa (40 km) pressure difference. So far, the Zermatt–Saas Zone has been attributed to HP conditions and the mechanism driving exhumation and accretion of the UHP Lago di Cignana Unit in its present structural position is not fully understood. Here we show that the top of the Zermatt–Saas Zone consists of a thin sliver of UHP serpentinites (the Cignana serpentinite), lying on top of a homogeneous unit (the Zermatt serpentinite). The Zermatt and the Cignana serpentinites underwent different pressure–temperature paths during the Alpine subduction history. The serpentinite enveloping the UHP Lago di Cignana Unit shows a first crystallization of olivine + Ti–clinohumite in rocks and veins at about 2.0 GPa and 450–500 °C. A second generation of veins include Ti–chondrodite formed at higher PT conditions of about 3.0 GPa and 600–650 °C, comparable to the UHP event recorded by the nearby eclogite and metasediments of the Lago di Cignana Unit. Type 1 and type 2 veins are both overgrown by later stage Ti–clinohumite.

The mineral association antigorite + olivine + Ti–clinohumite/chondrodite is thus stable in serpentinites at U HP conditions in the coesite and diamond facies. Furthermore, the trace element and isotopic compositions of the Cignana serpentine suggest geochemical exchange with the nearby crustal rocks of the Lago di Cignana Unit. This geochemical imprint is different from the one recorded by the Zermatt serpentinite, which only records oceanic hydration and underwent subduction in a close system environment. This implies that the UHP serpentinite enveloping Cignana was tectonically juxtaposed with the Cignana crustal rocks during the prograde subduction history, exchanging fluid–mobile trace elements and modifying its pristine oceanic isotopic signature. The crustal UHP Cignana rocks and the associated UHP serpentinite were exhumed together along the major discontinuity separating the Zermatt and the Combin Zones, which may represent a fossil plate interface active during the exhumation stages.

INTRODUCTION

Serpentinites are considered as key rocks affecting the geochemical cycles of fluid mobile elements and tectonics in subduction zones (**Spandler and Pirard, 2013**; **Deschamps et al., 2013**; **Kendrick et al., 2017**). Due to their ability to transfer water (**Ulmer and Trommsdorff, 1995**) and fluid mobile elements to great depths, they have been referred to as 'sponges' (**Deschamps et al., 2011**), whose behaviour during hydration and dehydration processes controls the geochemical and physical properties of subducting slabs and overlying mantle (**Reynard, 2013**; **Rüpke et al., 2004**). Increasing importance is now given to interface domains between subducting and overlying plates, where serpentinite is part of tectonic mélanges atop the slab (**Bebout, 2007; Scambelluri et al., 2014**), forms thick tectonic slices detached from slabs and accreted to the plate interface (**Angiboust et al., 2014**; **Guillot et al., 2015**; **Cannaò et al., 2016**), or derives from hydration of supra–subduction mantle (**Guillot et al., 2001**; **Bostock et al., 2002**; **Savov et al., 2005; Ryan et al., 2014**). From a geophysical point of view, architecture and lithologies of the subduction plate interface are uncertain due to limited resolution in geophysical screening of deep subduction environments. Several models for the plate interface environment tried to integrate field/structural and petrological/geochemical studies with geophysical investigations of present day subduction zones (**Ranero & Sallares, 2004**; **Bebout, 2007**; **Brovarone et al., 2013**; **Agard et al., 2009**; **Angiboust et al., 2009**; **2014**; **Bostock, 2013**). These models suggest the plate interface is a sharp contact between oceanic crust and mantle wedge, which preserves distinct lithological domains, or coincides with a mechanical and metasomatic melange zone. One of these models for deep (80 km) environments describes this plate interface as consisting of decoupled slices of coherent oceanic crust and metasediments associated with thick portions of serpentinized slab mantle (**Angiboust et al., 2009, 2014**). This implies complex geometries with strain partitioning and deformation accumulated in 100–500 m thick serpentinite shear zones enveloping less deformed bodies of oceanic crust and metasediments (**Guillot et al., 2001**; **Angiboust et al., 2011; 2012b; 2014**). Understanding such geometries and the processes involved during subduction and exhumation is vital to characterize the timing of coupling–decoupling of different oceanic slices and their accretion at the plate interface.

The interest in serpentinites increased in the mid–1990s, based on the discovery of widespread ocean floor serpentinization (**Cannat et al., 1995**) and the stability of antigorite to eclogite–facies conditions (**Ulmer & Trommsdorff, 1995**; **Scambelluri et al., 1995; Schmidt & Poli, 1998**). This led to investigations on the role of subducted serpentinized mantle in water and fluid–mobile element recycling to arc magmas (**Scambelluri et al., 2004, 2014**; **Scambelluri & Tonarini, 2012**; **Deschamps et al., 2011, 2013**; **John et al., 2011**; **Kendrick et al., 2011**; **Debret et al., 2013a, 2013b; Cannaò et al., 2015, 2016; Rüpke et al., 2004; Iwamori, 1998**) and its involvement in exhumation tectonics (**Hermann et al., 2000; Schwartz et al., 2001**). Serpentinites are reliable tracers of geochemical interactions and metasomatism in subduction zones (**Hattori et al., 2005; Deschamps et al., 2011, 2013; Scambelluri & Tonarini, 2012; Scambelluri et al., 2015; Cannaò et al., 2015, 2016; Lafay et al., 2013**). Serpentinites acquire their peculiar geochemical (e.g. B, U/Cs, As, Sb; **Kodolányi et al., 2012**; **Peters et al., 2017**) and isotopic (e.g. marine $^{87}Sr/^{86}Sr$, $\delta^{11}B$) characteristics during the main oceanic serpentinization event, and these may variably evolve during their subduction. The study of subducted serpentinites and associated oceanic crust and metasediments can be a powerful tool to reconstruct geometry and architecture of fossil subduction systems (**Scambelluri & Tonarini, 2012; Cannaò et al., 2015, 2016; Scambelluri et al., 2014, 2015**).

Serpentinized mantle can host up to 13 wt.% of water to HP and UHP depth (**Ulmer & Trommsdorff, 1995**). Dehydration reactions like antigorite + brucite → olivine + H_2O, and antigorite → olivine + orthopyroxene + chlorite + H_2O release substantial amounts of water in subduction zones, triggering element exchange between serpentinites and adjacent rocks. Although these reactions can provide reliable temperature constraints (**Sanchez–Vizcaino et al., 2005; Scambelluri et al., 2004, 2014**), the steep slopes of dehydration reactions in a pressure versus temperature plot prevent accurate pressure estimates (**Ulmer & Trommsdorff, 1995**). To the contrary, the transition from Ti–Clinohumite to Ti–Chondrodite (2.6–3.0 GPa for 500–650 °C), helps to constrain the pressure attained during high–pressure (HP) metamorphism of serpentinite (**Shen et al., 2015**).

Serpentinite and de-serpentinization fluid compositions help to unravel element exchange and fluid–pathways in HP subduction settings. The HP ophiolites of Zermatt–Saas Zone (**Figure 1**) and the associated ultrahigh–pressure (UHP) oceanic crust of the Lago di Cignana Unit (**Figures 1 and 2**), are suitable locations to investigate fluid exchange under UHP subduction conditions. The Zermatt–Saas Zone (ZSZ) is a slice of eclogite–facies oceanic crust (**Ernst & Dal Piaz, 1978; Bucher et al., 2005; Angiboust et al., 2009**) in contact with the continental Monte Rosa Nappe at the bottom and the blueschist–facies metaophiolites of the Combin Unit at the top. The top of the ZSZ hosts several tectonic slices of different ages, pressure–temperature evolution and provenance (Teodulo, Etirol–Levaz, Allalin Gabbro; **Bucher & Grapes, 2009; Skora et al., 2015**). One of these slices, the Lago di Cignana Unit (LCU), was subducted to more than 90 km depth (3.2 GPa – 550 °C) during the Eocene and retains the highest recorded pressures amongst HP ophiolites in the Alpine–Himalayan orogenic system (**Figure 1; Reinecke, 1998; Groppo et**

al., 2009; Frezzotti et al., 2011). As such, it represents a good proxy for studying the fluid pathways and the tectonic coupling of different rock units within the plate interface during UHP metamorphism.

There is strong debate about whether the Zermatt–Saas Zone was a coherent tectonic unit during its subduction–exhumation cycle. Several structural and petrologic studies suggest that this is the case, also based on original stratigraphic contacts preserved (**Angiboust et al., 2009; Beltrando et al., 2010; Tartarotti et al., 2017**). Other work indicates that the Zermatt–Saas Zone is a stack of different slices which followed distinct subduction–exhumation paths (**Li et al., 2004**; **Bucher and Grapes, 2009; Groppo et al., 2009; Rebay et al., 2012; Zanoni et al., 2016; Skora et al., 2015**). **Skora et al. (2015)** evaluated and discussed Lu–Hf ages from various slices in the Zermatt–Saas Zone and suggested an early subduction of the units at its structural top (50 Ma; Lago di Cignana, Pfulwe, and Chamois), followed by a largely coeval peak metamorphism at around 43–39 Ma.

Classic petrologic work has reconstructed the evolution of the Zermatt Saas Zone from basaltic eclogites, often ignoring (for a lack of viable geobarometers) the tectonic history and PT evolution of the surrounding serpentinites. Using simple thermodynamic modelling on Zermatt serpentinites directly underlying the Lago di Cignana Unit, **Rebay et al. (2012)** reports peak estimates up to 2.7 GPa. Following these results, **Zanoni et al. (2016)** suggested that such PT estimates may point to a domain of UHP conditions. Nonetheless, PT estimates on basaltic eclogites suggest the Zermatt–Saas zone was equilibrated at an overall lower P (Angiboust et al., 2009). Furthermore, it has remained unclear whether an antigorite + olivine + Ti–clinohumite system will survive UHP conditions ($P \geq 3.0$ GPa), because this assemblage was never found in natural sample but only observed in experimental work (**Ulmer and Trommsdorff, 1995**).

In this work, we sampled serpentinites at increasing distance from the UHP Lago di Cignana Unit (**Figure 2**) to test whether the transition from the UHP Cignana Unit to the surrounding serpentinite is accompanied by a change in PT conditions recorded by serpentinites and/or by a change in their trace element (TE) and isotopic (Sr and Pb) composition. Our goal is to compare the geochemical and isotopic imprint of the ZSZ and the Cignana serpentinites, verify whether element exchange occurred between the crustal UHP Cignana rocks and the surroundings serpentinites and if so, at which conditions it took place. This will shed light on the nature and behaviour of the plate interface during the Alpine subduction cycle.

GEOLOGIC AND PETROLOGIC BACKGROUND

The Piemonte Ophiolite Nappe is the remnant of the Mesozoic Piemontese ocean, subducted and incorporated into the Alpine orogen. In the Valtournenche area (Aosta Valley, Italy), the Piemonte Ophiolite Nappe consists of a pile of tectonic slivers commonly divided into Combin Zone on top, and Zermatt–Saas Zone at the bottom (**Bearth, 1967**). The high–pressure ophiolite units from Valtournenche and Aosta Valley are overlain by the continental Dent Blanche klippe (blueschist–facies) and Sesia-Lanzo (eclogite–facies) units. The Combin Unit represents the sedimentary transition between the Piemonte ocean and the European continental margin (**Figure 1**). It consists of metamorphic conglomerates, quartzites, dolostones, and sedimentary breccias, containing slices of serpentinized mantle peridotite equilibrated in epidote–blueschist facies during the Eocene (300–450 °C and ~0.9 GPa; ~44 Ma; **Reddy et al., 1999**).

The Zermatt–Saas Zone represents a subducted remnant of the Mesozoic Tethys. It consists of: (1) serpentinized mantle peridotite (**Li et al., 2004; Rebay et al., 2012**), (2) portions of oceanic crust (Fe–Ti and Mg–Al gabbros and metabasalts) strongly re–equilibrated in eclogite, blueschists and greenschists facies (**Bucher et al., 2005**) and subordinate oceanic metasediments (Mn–rich quartzites, calc–schists and marbles; **Bearth & Schwander, 1981**). Previous work on Zermatt serpentinite, performed by **Rebay et al. (2012)** and **Zanoni et al. (2012)** showed that this area underwent a complex tectonic and metamorphic history, from oceanic hydration to Alpine subduction. The authors distinguished three main deformation events, related to deformation–induced recrystallization of antigorite and metamorphic olivine during the prograde (D1), peak (D2), and retrograde (D3) metamorphic event. D1 develops an antigorite foliation (S1). Olivine + Ti–clinohumite + magnetite veins cut the S1 foliation and are, in turn, deformed and stretched along an olivine–bearing foliation (S2). Late crenulation (D3) and open folding deforms the pervasive HP S2 foliation and develops a weak, antigorite + chlorite foliation (S3). Zircon crystals associated with the HP S2 foliation in serpentinite gave an age of about 65.5 Ma (**Rebay et al., 2017**).

The central section of the ZSZ shows concordant metamorphic peak conditions (540 ± 20 °C and 2.3 ± 0.1 GPa; **Figure 3**; **Angiboust et al., 2009**) and ages (41–38 Ma, **Skora et al., 2015**). To the contrary, the top–section of the ZSZ, in contact with the Combin Unit, shows greater complexity. Here, oceanic and continental slices of different provenance, PT histories, and metamorphic ages occur within olivine– and Ti–clinohumite–bearing serpentinites (Etirol–Levaz, **Beltrando et al., 2010**; Pfulwe, **Skora et al., 2015**; Allalin Gabbro, **Bucher & Grapes, 2009**; Teodulo Glacier Unit, **Weber & Bucher, 2015**; Lago di Cignana Unit, **Groppo et al., 2009; Frezzotti et al., 2011**; **Reinecke, 1998**). One of these slices of metasediments and eclogites, the Lago di Cignana Unit (LCU), crops out to the South of the Cignana artificial lake, SW of the dam. The Lago di Cignana Unit is a small slice of MORB–type oceanic crust covered by oceanic sediments tectonically sandwiched between the lower ZSZ and the overlying Combin and Dent Blanche Units. The peculiar feature of the Cignana crustal section is that it equilibrated under ultrahigh–pressure (UHP) conditions during the alpine event (600 °C – 3.2 GPa; **Figure 3**; Groppo et al., 2009;

Reinecke, 1998), witnessed by the presence of coesite inclusions in mafic rocks and metasediments and of microdiamonds in meta–sedimentary rocks (**Reinecke, 1991, 1998; Frezzotti et al., 2011**). Pressure estimates of up to 3.6 GPa derive from microdiamond occurrence (**Frezzotti et al., 2011**). U–Pb zircon ages of Cignana eclogite yield an average of 44.1 ± 0.7 Ma, interpreted to date the peak subduction event (**Rubatto et al., 1998**). Rb–Sr cooling ages on white mica in Cignana metasediments indicate rapid exhumation at ~38 Ma (**Amato et al., 1999**). Several authors (**Forster et al., 2004; Groppo et al., 2009; Reinecke, 1998**) consider these serpentinites to be part of the underlying, lower pressure, Zermatt–Saas Zone.

ANALYTICAL METHODS

Bulk rock major element concentrations were measured either by XRF at the Activation Laboratories in Toronto, Canada, or by the laser–ablation ICP–MS pressed powder pellet (LA–ICP–MS PPP) technique at the University of Bern, Switzerland (**Peters & Pettke, 2017**). Trace element measurements were done either by liquid–mode ICP–MS at the University of Montpellier, France, or by LA–ICP–PPP at the University of Bern, Switzerland. Data are reported in **Table 2**.

Liquid mode ICP–MS followed the procedures described in **Ionov et al. (1992)** and in **Godard et al. (2000)**. 100 mg powdered sample aliquots were dissolved in a $HF/HClO_4$ mixture in screw–top Teflon beakers and then diluted for measurement by a factor of 1000, 2000, and 4000 for ultramafic, mafic, and silicic rocks, respectively, using an Agilent 7700X quadrupole ICP–MS. External calibration solutions employed were multi–element standard solutions (Merck) except for Nb and Ta, and In and Bi were used as internal standards. To avoid memory effects due to the introduction of concentrations Nb–Ta solutions in the instrument, Nb and Ta concentrations were determined by using, respectively, Zr and Hf as internal standards. This surrogate calibration technique is adapted from the method described by **Jochum et al. (1990)** for the determination of Nb by spark–source mass spectrometry. Scandium, V, Mn, Co, Ni, Cu, Zn, and As were measured in helium cell gas mode, in order to reduce polyatomic interferences. Reproducibility and accuracy of analyses were monitored by measuring, as unknows, the standards BHVO-1, BE-N and OU6 (used for trace–element rich rocks, like gneiss, micaschist and black-wall), UB-N, BIR-1 and MRG1 (for intermediate mafic rocks), and JP-1 and DTS-1 (for depleted chlorite harzburgite).

Bulk rock measurements performed by LA–ICP–MS PPP follow the procedures documented in detail by **Peters & Pettke (2017)**. The sample processing procedure comprised the following steps: (1) dry milling of crushed rock powder and (2) subsequent wet milling of ~2.2 g of rock powder in 5.6 g of high purity water, all in agate milling equipment using a Retsch PM 100 planetary ball mill, to obtaining an average powder grain size a few µm. (3) The sample suspension is then dried down on a hot plate under a fume hood at 70 °C. (4) The production of the pressed powder pellets involves homogenisation of the dried powder and mixing by hand of 120 mg rock powder with 30 mg of microcrystalline cellulose as binder using a small agate mortar and pestle, and then pressing robust pellets in a manual hydraulic press at 500 MPa using an in–house built steel apparatus. The resulting pellets were measured at 6 spots each with a laser beam size of 120 µm, an energy density of 5 J/cm^2 at a repetition rate of 10 Hz, and calibrated by bracketing standardisation employing the United State Geological Survey (USGS) basalt glass GSD–1G. LA–ICP–MS measurements were done using a Geolas Pro 193 nm ArF excimer laser coupled with an Elan DRC–e ICP–MS at the University of Bern, Switzerland. Instrument optimisation procedures followed those detailed in **Pettke et al. (2012)**. Data reduction employed SILLS (**Guillong et al., 2008**), and 100 wt.% minus LOI (wt.%) was used as the internal standard for quantification. Due to lack of data on Fe^{3+}/Fe^{2+}, total iron was calculated as FeO. Analytical accuracy was monitored by measurement of BCR–2G standard as PPP, and data correspond to the long–term averages reported in **Peters & Pettke (2017)** except for Be and Cd, for which measurements near the respective limits of detection can produce strong overestimates (Peters and Pettke, 2017).

Isotope ratio measurements were performed using a Finnigan MAT 262 multiple collector thermal ionisation mass spectrometer (TIMS) at IGG–CNR of Pisa (Italy). For Pb, the instrument was operated in static mode. Lead fractions were purified with conventional ion chromatography using Dowex AG1–X8 anion resin, using standard HBr and HCl elution procedures. Lead was loaded on single Re (99.999% pure) filaments with TEOS solution and measured at a pyrometer–controlled temperature of 1310 °C. Replicate analyses of Pb standard SRM981 yielded isotope ratios are accurate to within 0.025% (2SD) per mass unit, after applying a mass bias correction of 0.15±0.01% per mass unit relative to the NIST SRM 981 reference composition of **Todt et al. (1996)**. Lead blanks were of the order of 0.2 − 0.4 ng during the period of chemistry processing; hence, no blank correction was made. Strontium isotope ratio measurements were performed in dynamic mode. Strontium fractions were purified using the Sr–spec ion exchange resin. Instrumental mass bias correction was done by internal normalisation to $^{86}Sr/^{88}Sr = 0.1194$. Replicate measurements of NIST SRM 987 ($SrCO_3$) standard gave an average value of 0.710207 ± 13 (2SD, n = 47). Our data were adjusted to $^{87}Sr/^{86}Sr = 0.710250$. Throughout the full chemical process, the Sr blanks were approximately 0.3 ng, which are negligible for the analysed samples (0.3–0.5 g of sample, depending on Sr content). Lead and Sr isotope ratios are reported with age correction (40 Ma; **Rubatto et al., 1998**) using U, Th, Pb, Rb, and Sr concentrations obtained from liquid mode ICP–MS measurements, respectively.

In–situ major element (SiO_2, TiO_2, Al_2O_3, Cr_2O_3, FeO, MgO, MnO, CaO, NiO, Na_2O, and K_2O) compositions of minerals (Table 2–6) were measured using a JEOL JXA 8200 Superprobe equipped with five wavelengths–dispersive (WDS) spectrometers, an energy dispersive (EDS) spectrometer, and a cathodoluminescence detector (accelerating potential 15 kV, beam current 15nA), operating at the Dipartimento di Scienze della Terra, University of Milano. The measurements of all elements were performed with a 30–second counting time. Results with total oxide percentage lower than 98% and higher than 102% were immediately discarded from the data set. A second measurement quality check was done based on atoms per formula unit, discarding measurements that showed more than 0.5% deviation from the stoichiometric composition.

RESULTS

Petrography and microstructures

Samples were collected along a profile from the internal part of the Zermatt–Saas Zone into the LCU UHP unit, localised in Figure 2 and reported in Table 1. Tectonic units sampled include (1) the serpentinites from the Zermatt Saas Zone, in the area described in **Rebay et al. (2012)**, (2) the Lago di Cignana Unit (basaltic eclogites and metasediments), and (3) the serpentinites directly in contact with the UHP Lago di Cignana Unit referred to here as Cignana serpentinites; serpentinites and Ti–chondrodite/clinohumite veins).

Zermatt–Saas Zone Serpentinite

Zermatt–Saas Zone serpentinites crop out in a structurally lower area with respect to the LCU (**Figure 2**). Three samples of Zermatt serpentinite (ZSG1405, ZSG1406, ZSG1410) from the area described in **Rebay et al. (2012)** were investigated in detail. The Zermatt serpentinite displays a well–developed antigorite (Atg) + olivine (Ol) + diopside (Di) ± magnetite (Mag) foliation (S2) parallel to boudinaged rodingite dykes and wrapping around less deformed serpentinite domains. This foliation and the less deformed serpentinite include pre–kinematic clasts of mantle clinopyroxene (Cpx), bastites after mantle pyroxene, and mesh structures (serpentine + magnetite) after mantle olivine (**Figure 4a–b**). Metamorphic diopside aggregates are stretched along the main foliation or grow around mantle clinopyroxene porphyroclasts. Sample ZSG1406 contains fragments of olivine + Ti–clinohumite (Ti–Chu) veins, locally showing tiny Ti–chondrodite (Ti–Chn) relict grains (**Figure 4c**).

Lago di Cignana eclogite and metasediments

The five metasediment samples comprise metaquartzite (LCG1414 and LCG1415), meta–calcschist (LCG1416A and LCG1416B), and marble (LCG1501), in addition to one basaltic eclogite (LCG1401; **Table 1**).

The basaltic eclogite (**Figure 5a**) consists of garnet (Grt), omphacite (Omp), phengite (Ph), and rutile (Rt). Garnet shows inclusion–rich cores, mostly coesite (Coe), quartz (Qz) phengite, zircon (Zrn), rutile, and apatite (Ap), and inclusion–poor rims. Omphacite occurs as large (mm–sized) crystals, generally zoned from core to rim. Eclogite shows various degrees of re–equilibration along weak foliations defined by blue– and/or green–schist facies minerals, mostly glaucophane (Gln) after omphacite, chlorite (Chl) and barroisite (Brs) after garnet. Amongst collected eclogites, sample LCG1401 (**Figure 5a**) show the weakest retrograde overprint (<5%).

The Cignana metasediments consist of (1) impure, locally Mn–rich, quartzite (LCG1415, **Figure 5b–c–d**), (2) garnet calcschists (LCG1416A and LCG1416B, **Figure 5e–f**), and (3) garnet–bearing impure marbles (LCG1501). Quartzite has poikiloblastic garnet and tourmaline (Tur) with inclusions of coesite (optically identified, now mostly quartz), phengite/piemontite, apatite, and rutile. Mn–quartzite contains garnet, phengite, piemontite (Pmt), pseudomorphs after lawsonite (Lws), and epidote (Ep) with an allanite (Aln) core (**Figure 5c–d**). Mn–garnet occurs within layers and close–packed nodules of 50–300 μm–sized crystals and often contains coesite inclusions (**Figure 5d**). Quartzite locally hosts large

(1–2 mm) garnet poikiloblasts and zoned tourmaline (LCG1415). Oriented phengite (3T polytype; **Groppo et al., 2009**) defines the foliation in quartzites. Exhumation–related quartz sub–grain growth along with undulous extinction suggests that all quartz recrystallized from original UHP coesite during exhumation. Quartzites are partially retrogressed to epidote–greenschist facies: albite (Ab) replaces phengite, albite and muscovite (Ms) replace lawsonite, and chlorite and barroisite replace garnet. Calcschist (LCG1416A and LCG1416B) and impure marble (LCG1501) contain calcite (Cal), quartz, poikiloblastic garnet, epidote, phengite, and rare paragonite (**Figure 5e–f**). Typical inclusions in garnet are calcite, apatite, rutile, coesite, and white mica. The UHP eclogitic assemblage is rarely preserved in calcschists. Garnet is partially chloritized at rims and late iron hydroxides replace HP mica and epidote.

Cignana Serpentinites

A serpentinite body, 1km long and 100m thick, crops out 200m to the West of the Southern section of the Lago di Cignana Unit (**Figure 2**). The Cignana serpentinite shows an antigorite + olivine–bearing HP foliation deforming rodingite dykes comparable to the S2 foliation described for the underlying Zermatt serpentinites (**Rebay et al., 2012**). In Cignana, widespread Ti–rich metamorphic veins cross–cut the olivine–bearing foliation and are, in turn, crenulated by later deformation events. We investigated four serpentinite samples (ZSG1403, ZSG1502S, ZSG1507S and ZSG1510), and three veins (ZSG1402, ZSG1502V, ZSG1507).

The serpentinite foliation is defined by elongated domains of HP metamorphic olivine, metamorphic diopside, and magnetite embedded in antigorite (**Figure 4d**). Chlorite aggregates with magnetite cores are stretched along the main foliation. Two types of veins cut the Cignana serpentinite: one dominated by Ti–clinohumite (type 1) and another contains Ti–chondrodite (type 2). Type 1 veins host 3–5 mm Ti–clinohumite crystals, olivine, chlorite, magnetite, and rare diopside (**Figure 4e**). Type 2 veins are 1–3 cm thick and up to 20 cm long, characterised by the occurrence of primary Ti–chondrodite. Type 2 veins consist of Ti–chondrodite, chlorite, olivine, apatite, and diopside (**Figure 4f–g**) and display a compositional banding consisting in 5–10mm thick chlorite–rich rims and Ti–chondrodite–rich cores. Ti–chondrodite occurs as 0.5–1 mm–sized, isolated crystals, filled with inclusions of ilmenite (Ilm), zircon and REE–bearing phases (**Figure 4f**). The Ti–chondrodite vein crystals display corroded rims which recrystallize into 50–500 µm–sized, inclusion–free, Ti–clinohumite neoblasts (**Figure 4f**). Olivine generally occurs as relics, partially replaced by Ti–clinohumite. In type 2 veins, chlorite occurs as idiomorphic, inclusion–free crystals (**Figure 4f**), and apatite occurs as mm–sized aggregates of solid and fluid inclusions–rich crystals (**Figure 4g**). Vein diopside occurs as sub–mm fibres bordering the Ti–clinohumite–rich bands (**Figure 4h**). Elongated fluid inclusions (Flincs) occur parallel to the diopside elongation axis. Such diopside fibres extensively recrystallized into finer–grained, inclusion–free diopside crystals (**Figure 4h**). The type 2 Ti–chondrodite–bearing veins contain no relics of potential igneous minerals, like aphyric clinopyroxene or ilmenite, which might hint to a Fe–Ti gabbroic protolith for these bodies (i.e. **Scambelluri & Rampone, 1999**).

Type 1 and type 2 veins are deformed by an olivine–bearing antigorite foliation and are crenulated during a later–stage deformation event. Crenulations display an olivine–free, antigorite axial plane foliation. In both type 1 and type 2 veins, the original mineralogy recrystallized into finer–grained (<1 mm), inclusion–free, Ti–clinohumite (2), chlorite (2), and diopside (2).

Bulk–rock compositions

The major and trace element and isotopic bulk compositions of metasediments, meta–oceanic crust and serpentinites from the Lago di Cignana Unit and from the Zermatt–Saas Zone are reported in **Tables 2 and 3** and illustrated in **Figures 6, 7, 8, 9 and 10**.

Major elements

The Zermatt–Saas Zone serpentinite displays a rather homogeneous harzburgitic composition (except for higher FeO content of sample ZSG1406), but with much lower Al_2O_3 (~1.5–1.7 wt.%) and CaO (~0.5%) content than Cignana serpentinites (**Figure 6a–b**).

The Cignana basaltic eclogite (LCG1501) is a typical oceanic Fe–Ti gabbro, has Al_2O_3 ~ 15.8%, TiO_2 ~ 2.5% and low L.O.I content (0.4%), compatible with an altered oceanic Fe–Ti gabbro protolith, as suggested by **Groppo et al. (2009)**. The Cignana metasediments include several lithological subtypes with varying silica and CO_2 contents. The most abundant varieties include Qz–micaschists with Mn–rich layers and calcschists. Qz–micaschists have a SiO_2 content >70% and Al_2O_3 of 7–12%; their compositional variability includes high MnO (~ 3.7%; sample LCG1414) and high B (360 µg/g; sample LCG1415) concentrations. Centimetre to m–sized layers of calcschist (CaO ~ 20–30%, L.O.I. ~ 20–30%; LCG1416A and LCG1416B) and silicate–bearings marbles (CaO ~ 30%, L.O.I. ~ 35%; LCG1501) reflect local variability in carbonate content.

The Cignana serpentinite displays a harzburgitic to lherzolitic composition with Al_2O_3 ~ 2.5–4.5% and CaO from ~ 2–4% up to 11.6% (this latter value reflects the exceptionally high diopside modal composition of sample ZSG1507S of about 40 vol.%; **Figure 6a–b**). Ti–clinohumite veins enclosed in Cignana serpentinites display variable major element compositions, especially for their FeO (~7–15%) and CaO (~3–9%) content. This difference reflects their relative abundance in magnetite, diopside, olivine, and Ti–clinohumite. The Ti–chondrodite vein has a major element (FeO, MgO, CaO, and Al_2O_3; **Figure 6a–b**) and Cr–Ni (**Figure 7**) composition comparable to mantle peridotites, Cignana serpentinite, and the Ti–clinohumite veins.

Trace elements

Zermatt Serpentinite. The Zermatt serpentinite displays rather depleted TE and REE patterns (**Figures 8 and 9**; C1 chondrite and PM from **McDonough & Sun, 1995**). Rare earth elements (REE) decrease from heavy to light and show a variably small negative Eu anomaly (**Figure 8**). All samples display comparable PM–normalized TE patterns, with notable enrichments in B, Bi, W, Mo, As, and Sb with respect to the mantle depletion trend (**Figure 9**).

LCU crustal rocks. The Cignana eclogite has a flat REE and TE pattern (**Figures 8 and 9**). Except for a slight depletion in Cs, Rb, Ba, and K, all other TE are equally enriched, between 10 and 30 times the primitive mantle. The Cignana metasediments have homogeneous REE patterns, showing steady decrease from light to heavy REE (**Figure 8**). All samples display a weak negative Eu anomaly, absent in the eclogite sample. The TE patterns show positive peaks in Cs, Rb, Pb, As, and Sb and negative peaks in Cd and Ti (**Figure 9**). Quartzites and calcschists show similar trends, except for Pb and Sr, up to one order of magnitude higher in calcschists, and for As and Sb, generally higher in quartzites. The remarkably high B content (365 µg/g) of sample LCG1415 reflects the presence of tourmaline.

Cignana Serpentinite. The Cignana serpentinite shows rather flat REE patterns, with values ranging between 1 and 10 C1 chondrite composition (**Figure 8**). The TE patterns scatter, showing positive anomalies for several fluid mobile elements (**Figure 9**). Noticeably, As and Sb values are very variable, ranging from PM values (ZSG1510; 0.07 and 0.01 µg/g) up to values two orders of magnitude higher (sample ZSG1502S, 1.82 and 0.3 µg/g). Moreover, the Cignana serpentinite displays (strong) enrichments in B, Bi, W, As, Sb, Sr and Th. The TE patterns of Ti–clinohumite veins hosted by the Cignana serpentinites closely resemble that of the host Cignana serpentinite, except for increased Nb, Ta, and Ti contents. The type 2 Ti–chondrodite vein (ZSG1402) is, instead, extremely enriched in all REE and most TE (especially Nb, Ta, Th, U), by up to 2 orders of magnitude relative to the host serpentinites. Type 2 vein displays a light–REE pattern comparable with metasediments and a slightly enriched heavy–REE pattern, most comparable with eclogite. Elements such as Cs, Rb, Ba, B, Cd, Pb, As, Sb, Sr, Ga, and Li display values comparable with those of Cignana serpentinites.

Isotopic Compositions

Selected samples from the Lago di Cignana Unit and from the Cignana and Zermatt serpentinites were analysed for their Pb and Sr isotopic compositions. All results, corrected for an age of 40 Ma, are shown in **Table 3** and displayed in **Figure 10**. The Zermatt serpentinite shows non–radiogenic Pb isotopic values (lower than DM values) for all three isotopic systems ($^{206}Pb/^{204}Pb$, $^{207}Pb/^{204}Pb$, and $^{208}Pb/^{204}Pb$ are 16.887–17.731, 14.841–15.548, and 35.776–37.555, respectively) and $^{87}Sr/^{86}Sr$ = 0.707051, typical for Jurassic seawater serpentinization (**Jones & Jenkyns, 2001**; **Vils et al., 2009**; **Cannaò et al., 2016**). The Cignana eclogite shows typical isotopic composition for MORB (Kelemen et al., 2014), with $^{206}Pb/^{204}Pb$, $^{207}Pb/^{204}Pb$, and $^{208}Pb/^{204}Pb$ being 18.547, 15.518, and 37.986, respectively and $^{87}Sr/^{86}Sr$ = 0.703764. The Cignana metasediments (quartzite and calcschist) show similar values as GLOSS–II (**Plank, 2014**); $^{206}Pb/^{204}Pb$, $^{207}Pb/^{204}Pb$, and $^{208}Pb/^{204}Pb$ are between 18.636–18.706, 15.642–15.652, and 38.719–38.881, respectively and $^{87}Sr/^{86}Sr$ is between 0.709368 and 0.711573. The Cignana serpentinite has Pb and Sr isotope values between DM and MORB values ($^{206}Pb/^{204}Pb$, $^{207}Pb/^{204}Pb$, and $^{208}Pb/^{204}Pb$ are 18.172–18.341, 15.402–15.596, and 37.692–38.129, respectively. $^{87}Sr/^{86}Sr$ are 0.703883–0.704160, lower values than Jurassic seawater (**Jones & Jenkyns, 2001**) and like MORB (**Kelemen et al., 2014**) and the Cignana eclogite. Ti–bearing veins in serpentinites retain similar $^{87}Sr/^{86}Sr$, and close to MORB values (0.704221 in Ti–chondrodite vein and 0.704059 in Ti–clinohumite vein). The Ti–clinohumite vein has Pb isotopic compositions comparable with the host serpentinite. To the contrary, the Ti–chondrodite vein is quite enriched in radiogenic lead, having values over the range reported for reservoirs around the Lago di Cignana Unit (eclogite and metasediments).

Mineral compositions

Major elements

We performed electron probe measurements on rock–forming minerals of the Cignana eclogite and metasediments, on the Cignana serpentinites and their Ti–clinohumite and Ti–chondrodite veins, and on the Zermatt serpentinites. Representative mineral data are reported in **Tables 4-9**; the full dataset is shown in the **repository data**. Cignana eclogite consists of garnet, omphacite and rutile. Garnet is of almandine–grossular composition and has Fe-rich cores (Alm ~ 56–57% and Prp ~ 7%) and Mg contents increase towards the rims (Alm ~ 50–51% and Prp ~ 8–9%). Jadeite content in omphacite increases from ~ 50% in the core to ~ 70% in the rim. Epidote occurs as small inclusions within garnet cores and has ~ 50% clinozoisite component. In the Cignana quartzite, garnet is almandine–grossular and has Ca–rich cores (Alm ~ 50–53%, Grs ~ 27–28%, Sps ~ 10–11% and Prp ~ 4%) and Fe(II) content increases towards the rims (Alm ~ 69–70%, Grs ~ 10–11%, Sps ~ 1–2% and Prp ~ 16–17%). Tourmalines are dravites, with schorl contents increasing from cores (~ 18–19%) to rims (~ 30–31%). Mn–rich layers in quartzites consists of quartz, Mn–rich (sps > 70%) garnet, phengite, and epidote (allanite cores and clinozoisite ~ 30% towards the rims). In the Zermatt serpentinites antigorite (**Figure 11a**) has low Al contents (~0.05–0.09 a.p.f.u.) and high Mg# (~0.97–0.98); Olivine (**Figure 11b**) has low NiO_2 contents (~0.05–0.1%) and Mg# (~0.96–0.98) comparable with associated antigorite, and Ti–chondrodite and Ti–clinohumite have different compositions with respect to Cignana serpentinites, presenting lower Ti contents and higher Fe(II) + Mg (**Figure 12a–b**). The Cignana serpentinites and the

Ti–clinohumite/chondrodite veins have similar mineralogy (despite changes in modal amounts of the single phases) and consist of antigorite, chlorite, olivine, diopside, magnetite, and Ti–clinohumite. Antigorite (**Figure 11a**) has Mg#~0.86–0.88 and variable Al contents (0.9–0.15 a.p.f.u.). Olivine (**Figure 11b**) shows similar compositions both in the serpentinites and in the Ti–clinohumite veins, having Mg#~0.84–0.88 and variable NiO_2 contents (~0.15–0.5%). Similarly, Ti–clinohumite (**Figure 12a**) has similar compositions both in Ti–clinohumite and in Ti–chondrodite veins (Ti~0.3–0.5 a.p.f.u.).

Trace elements

The full LA–ICP–MS mineral trace element dataset for the Cignana eclogite and metasediments and the Cignana and Zermatt serpentinites and Ti–clinohumite veins is reported in the **repository data**. Representative analyses are shown in **Tables 10-13** and plotted in **Figure 13**. Antigorite (**Figure 13**) displays rather similar TE and REE patterns, both in Cignana and Zermatt serpentinites. REE are depleted (0.01 to 0.1 C1 chondrite) and show a slight increase from light to heavy REE. Cignana serpentines are slightly more enriched in light REEs. Cignana serpentines show enrichment in Th, Be, Ta, La and Ce. Conversely, Zermatt serpentines have higher B, As, and Sb. In the Cignana serpentinite, olivine is depleted in light–REE and enriched in heavy REEs, B, Sb, and Li (**Figure 13**). While the major element composition of diopside from the Zermatt and Cignana serpentinite is similar, its REE and TE compositions differ (**Figure 13**). The Cignana diopside is enriched in REE (~5–10 times the C1 chondrite), while in the Zermatt serpentinite, diopside is depleted in REE, showing a slight negative Eu anomaly. Besides REE's, the Cignana diopside is enriched in Rb, U, Th, Be, Ce, Pb, and Sr. Conversely, Zermatt diopside contains considerable amounts of W, B, As, and Sb. Ti–clinohumite (**Figure 13**) has generally similar patterns in all Cignana lithologies. Ti–clinohumite is enriched in Nb, Ta, B, W, As, Sb, and

REE. To the contrary, Ti–clinohumite in Zermatt serpentinite has more depleted trends, with lower levels of REE, Nb, and Ta.

DISCUSSION

PT evolution of the Cignana serpentinite

The Lago di Cignana Unit consists of oceanic crustal rocks such as eclogites and metasediments which underwent a complex Alpine subduction history to UHP metamorphic conditions. Prograde zoning in garnet, omphacite and white mica, observed in both metasedimentary rocks and metagabbros, records subduction to UHP depth along a cold geothermal gradient (~7 °C/km; **Amato et al., 1999; Groppo et al., 2009; Reinecke, 1998; Rubatto et al., 1998; Skora et al., 2015**). Re–hydration and destabilization of HP phases in eclogite and metasediments indicates exhumation to greenschist–facies conditions following the UHP peak (26 km/m.y.; **Amato et al., 1999**). HP serpentinites sandwich the UHP Lago di Cignana Unit and display an antigorite + olivine foliation deforming olivine + Ti–clinohumite + magnetite ± diopside metamorphic veins. **Rebay et al. (2012)** recently studied the serpentinites and associated eclogites lying below the Lago di Cignana Unit (the Zermatt serpentinite). These serpentinites reached pressure conditions of 2.4–2.6 GPa during the Alpine HP event (**Rebay et al., 2012; Angiboust et al., 2009**), like several other ophiolite domains in the Western Alps (e.g. Erro–Tobbio, **Scambelluri et al., 1995**; Lanzo Ultramafic Massif, **Pelletier and Müntener, 2006**; **Debret et al., 2013a, 2013b**). The serpentinites lying above the Lago di Cignana Unit (the "Cignana serpentinites") were, instead, never investigated in detail and are commonly attributed to the Zermatt–Saas Zone. Our observations of the Zermatt and Cignana serpentinites add further detail and information to this scenario.

The HP Zermatt serpentinites are characterized by the formation of HP olivine via the dehydration of brucite, according to the reaction (1) antigorite + brucite = olivine ± chlorite + H_2O, which liberates a fluid phase drained in olivine + Ti–clinohumite + magnetite veins (**Figure 14**). This type of vein forms in serpentinites during prograde metamorphism in the presence of free water, after simultaneous breakdown of brucite (reaction 1 in Figure 14) and former Ti–bearing clinopyroxene, according to the generalized reaction: mantle clinopyroxene + olivine + antigorite = diopside + chlorite + Ti clinohumite + H_2O (**López Sánchez–Vizcaíno et al., 2009**). Genesis of such veins has been related to these dehydration reactions in the Zermatt–Saas Zone (**Rebay et al., 2012; Zanoni et al., 2012**), as well as in other HP serpentinites such as Erro–Tobbio (**Scambelluri et al., 1995**), the Lanzo Massif (**Debret et al., 2013a**), and Cerro de Almirez (**López Sánchez–Vizcaíno et al., 2009**).

The Cignana serpentinites display a well–developed antigorite + olivine foliation, locally deforming two distinct types of veins containing titanate phases: type 1 and type 2 veins. Type 1 veins contain Ti–clinohumite as the main Ti–bearing phase (large crystals, locally overgrown by finer–grained Ti–clinohumite), plus olivine, chlorite, magnetite, and rare diopside (**Figure 4e**). **Figure 14** shows a series of reaction lines (adapted from **Shen et al., 2015**) in the system TiO_2–MgO–SiO_2–H_2O (plus the reactions graphite–diamond and quartz–coesite for comparison with the LCU crustal lithologies), based on which the *P*-*T* formation conditions of type 1 veins can be constrained (in analogy to the veins reported for Almirez; **López Sánchez–Vizcaíno et al., 2009**). The *P*-*T* field is roughly divided into two domains by reaction (5): an orange shaded area delimiting the stability field of Ti–clinohumite, and a reddish area at higher pressure were Ti–chondrodite is stable. The black arrow is the PT path proposed by **Groppo et al. (2009)** for eclogites in the Lago di Cignana Unit. The origin of type 1 veins can be related to the formation of metamorphic diopside and to brucite dehydration, according to reaction (1) and (2) respectively. Brucite dehydrates at a temperature of around 500 °C, which corresponds to about 2.0–2.5 GPa (~ 75km depth) considering the *P–T* estimates of eclogites from the ZSZ (**Angiboust et al., 2009**) and a typical Alpine subduction geothermal gradient (6.5–7.5 °C/km; **Scambelluri et al., 1995; López Sánchez–Vizcaíno et al., 2009; Groppo et al., 2009**). The TE composition of these veins (**Figure 9**) closely compares to that of the host rock, suggesting dehydration in a closed system, with little to no influx of externally derived components and fluids. As such, the Cignana and Zermatt serpentinites released moderate amounts of aqueous fluid during subduction, which slightly remobilized many elements and locally recrystallized as Ti–clinohumite–bearing veins.

The second occurrence of Ti–bearing minerals concerns the type 2 veins, hosting coarse Ti–chondrodite, chlorite, olivine, diopside, and apatite (Sample ZSG1402). The presence of Ti–chondrodite as main vein–forming mineral readily indicates that type 2 veins formed at higher pressures than type 1, in the stability field of Ti–chondrodite (orange shaded area in **Figure 14**). Importantly, the *P-T* conditions necessary for the formation of TI–chondrodite–bearing veins are not recorded in the Zermatt–Saas Zone. To the contrary, they are compatible with the *P-T* path recorded in the Lago di Cignana Unit eclogites and metasediments (**Figure 14**; **Groppo et al., 2009**). Such estimates for the formation of type 2 veins lie at higher temperature than the dehydration reaction (1), which generated type 1 veins, and at lower temperature than the expected antigorite dehydration of reaction (2). As such, it is unlikely that the fluid responsible for the type 2 veining had an internal origin as for the type 1 veins. Instead, this fluid was probably externally derived (i.e. non–serpentinitic). Hypotheses on the possible origins of such fluid are discussed below.

Deformation and recrystallisation of type 1 and 3 veins occurred during a lower pressure deformation event (D3). Large crystals are replaced by smaller metamorphic phases: Ti–clinohumite(2) replaces Ti–chondrodite and Ti–Clinohumite (**Figure 4e–f–g–h**); when present, first generation olivine, chlorite, apatite, and diopside recrystallize. Regarding the origin of such Ti–chondrodite veins, we propose here that type 2 veins crystallized from a fluid derived from the nearby crustal Cignana rocks for the following petrologic and geochemical reasons. Compared to type 1 Ti–clinohumite veins, the type 2 Ti–chondrodite veins are strikingly enriched in REE, Th, U, Nb, Ta, As, Sb, and Y (**Figure 9**). This enrichment can be interpreted to be due either to (1) metasomatism of initial gabbroic dykelets (**Scambelluri & Rampone, 1999**) or to (2) channelized infiltration of metamorphic fluids enriched in crustal components into the Cignana serpentinite at UHP conditions. In the Voltri Massif, **Scambelluri & Rampone (1999**) described Ti–chondrodite + Ti–clinohumite + diopside + chlorite bearing veinlets associated with the occurrence of igneous clinopyroxene and ilmenite relics, which provided evidence for an origin from metasomatized Fe–Ti gabbroic dykelets. Differently from Voltri, magmatic clinopyroxene and ilmenite relics are absent in the Ti–chondrodite + olivine veinlets from Cignana. Nevertheless, favouring hypothesis (2) does not enable to rule out hypothesis (1). However, a magmatic origin of such veins should be recorded by the immobile elements in the bulk composition (e.g. Cr and Ni), which are very different in concentration in a former gabbroic dyke with respect to a peridotite. **Figure 7** shows that Cr–Ni bulk compositions of the Cignana Ti–chondrodite veins are comparable with serpentinites, peridotites and type 1 veins is and strongly different from reference eclogites and gabbroic dykes. This bears implications on the fluid origin of type 2 Ti–chondrodite veins.

The petrogenetic sequence presented in **Figure 15** summarizes and compares the metamorphic evolutions of the Zermatt serpentinites with the Cignana serpentinite and the Lago di Cignana Unit. The mineralogical and textural evolution of the Cignana serpentinites thus reveals prograde, peak, and retrograde events. The three metamorphic stages recorded in type 1 and 2 veins and in their LP recrystallization products are comparable to the metamorphic evolution defined for the coesite–bearing eclogites and metasediments (**Groppo et al., 2009**). The type 1 veins can correspond to the prograde metamorphic zoning observed in eclogitic garnet (**Reinecke, 1998; Groppo et al., 2009**), while type 2 Ti–chondrodite–bearing veins in serpentinites likely formed under peak metamorphic conditions in the coesite stability field. Consequently, peak conditions are consistent for both the Lago di Cignana Unit and the Cignana serpentinites. Retrograde re–equilibration of eclogite and metasediments (formation of chlorite after garnet and barroisite and glaucophane after omphacite) indicates near–isothermal decompression (**Groppo et al., 2009**). In serpentinites, this retrograde event causes the recrystallization of type 1 Ti–clinohumite and type 2 Ti–chondrodite veins. As such, the microstructural and mineralogical record of the Ti–bearing veins provides constraints to the evolution of the Lago di Cignana Unit and of the surrounding serpentinites throughout their prograde, peak and retrograde evolution. A main implication of this finding is the stability of the mineral association antigorite + olivine in natural samples at UHP metamorphic condition, as predicted from experimental work by **Ulmer & Trommsdorff (1995)**.

Zermatt–Saas serpentinites (ZSG1405, ZSG1406 and ZSG1410) are closely comparable to Cignana serpentinites in petrology, microstructure, and field occurrence. As such, it is difficult to clearly distinguish the Cignana serpentinites from the Zermatt–Saas serpentinites; hence, the definition of a boundary for the UHP event in serpentinites is not possible. Furthermore, the occurrence of Ti–chondrodite is not limited to the area surrounding the LCU. Ti–Chondrodite is found in sample ZSG1406 and it is reported in other sections of the Zermatt–Saas Zone (**Rebay et al. (2012)**; Tartarotti, Hermann, personal communications). This might imply (1) deeper subduction of the Zermatt area than so far known and only local preservation of the UHP mineralogy, or (2) that the Zermatt–Saas consists of slices of oceanic crust and metasediments which were equilibrated at different depths, and were then incorporated into the plate interface during exhumation. In this latter case, the model of tectonic coherence of the Zermatt–Saas unit should be reconsidered, an arduous task given the extensive greenschist–facies retrogression of metabasic rocks and/or lack of viable pressure indicators. Trace element and isotopic analyses in serpentinites (discussed below) proved to be a useful tool to discriminate between different serpentinite slices.

Geochemical evolution

Recent work (**Hattori & Guillot, 2003**; **Deschamps et al., 2011**, **2012**, **Lafay et al., 2013**; **Scambelluri et al., 2014, 2015**; **Cannaò et al., 2015, 2016**; **Debret et al., 2013b**) has investigated the role of serpentinites in acquiring and releasing FME during tectonic processes. Interaction with subduction fluids (**Cannaò et al., 2015, 2016**), as well as lizardite–antigorite and antigorite dehydration reactions (**Kodolányi and Pettke, 2011**; **Debret et al., 2013a, 2013b**), change the TE budget of a serpentinite and might affect its Sr–Pb isotopic signature (**Cannaò et al., 2015, 2016**). FME geochemistry, coupled with detailed field and microstructural investigations, helps unravelling (1) the timing and tectonic setting of fluid–rock interaction and (2) the evolution of the serpentinites during their subduction–exhumation cycle.

Using this geochemical petrology approach, we discuss (1) the tectonic setting of initial serpentinization and the evolution and FME exchange of the Zermatt and Cignana serpentinites and (2) the origin of fluids interacting with serpentinites. This will allow us to propose a possible evolution of the Zermatt–Saas Zone near the Lago di Cignana Unit.

Inherited features of Zermatt and Cignana serpentinites

The Western Alpine ophiolites are fragments of different sections of the Ligurian–Piemontese slow–spreading ocean opened during the Jurassic (**Dal Piaz et al., 2003**;

Piccardo, 2008; Rampone et al., 2014). Studies of pristine non–subducted sections of this ocean basin show that the mantle peridotites underwent melt depletion and refertilization by circulating melts in the stability fields of spinel and subsequently plagioclase. The final composition of a peridotite is thus the result of combined processes of melt extraction, melt percolation and melt–rock interactions, leading to dissolution of pyroxenes and recrystallization of olivine (**Godard et al., 2000**; **Rampone et al., 2004; Müntener et al., 2004**). This complex mantle history can be traced back in serpentinites by studying the composition of mantle clinopyroxene relics and bulk rock major and rare earth elements, which largely remain unaltered by serpentinization (**Niu, 2004**).

Zermatt and Cignana serpentinites only sporadically preserve relics of pristine mantle clinopyroxene (e.g. **Figure 4a**). This scarcity of mineralogical relics of mantle phases affects the whole Zermatt–Saas Zone (**Dal Piaz et al., 2003**; **Li et al., 2004; Angiboust et al., 2009; Rebay et al., 2012**). Therefore, as a careful characterization of the serpentinite protolith mineralogy is not feasible, geochemical data are used to constrain the mantle precursor rocks and to define mass transfer and fluid/rock interaction during serpentinization at the seafloor and during subduction.

To a first order, ocean floor serpentinization does not significantly affect the initial peridotite major element budget and ratios (**Bogolepov, 1970**; **Coleman & Keith, 1971; Niu, 2004; Deschamps et al., 2013**). Exceptions are local CaO depletion due to serpentinization and/or chloritization of Ca–bearing plagioclase and clinopyroxene, and/or fluid element addition, introduction of silica (talc metasomatism; **Paulick et al, 2006**), Mg loss by marine weathering (**Snow and Dick, 1995**), or CO_2 addition forming ophicarbonates near the ocean floor (carbonation; **Bideau et al., 1991**). **Figure 6a–b** shows major element relations in Zermatt and Cignana serpentinites. The Zermatt serpentinite displays a refractory composition, with MgO > 37 % and low Al_2O_3 and CaO levels. To the contrary, the Cignana serpentinite shows more enriched compositions, with lower MgO content and higher CaO and Al_2O_3 (**Figure 6a–b**). As a first approximation, the major element composition of the Zermatt and Cignana serpentinites may suggest a derivation from harzburgitic and lherzolitic protolith, respectively.

In **Figure 9**, the REE compositions and patterns of (1) pristine depleted harzburgites and (2) refertilized (plagioclase–impregnated) lherzolite from the Lanzo Massif (**Guarnieri et al., 2012**) overlap with the Zermatt and Cignana serpentinites, respectively. One Cignana serpentinite (sample ZSG1407S) is slightly more enriched, due to a larger mode of diopside. In summary, the Zermatt and Cignana serpentinites features likely represent local compositional variations within a coherent lithospheric mantle, which is a common feature of the Thetian ophiolitic oceanic lithosphere (Internal Ligurides, **Rampone & Piccardo, 2000**; Erro–Tobbio, **Rampone et al., 2014**; Lanzo, **Müntener et al., 2004**; **Guarnieri et al., 2012**). Alternatively, the Cignana serpentinite might be a tectonic sliver sampling a different section of lithospheric mantle, detached and juxtaposed over the Zermatt serpentinites only during exhumation.

Variation of the initial composition of the Zermatt and Cignana serpentinite

Mantle peridotites can be serpentinized in oceanic as well as in subduction zone settings. The serpentinization reactions occurring in the two different environments can be accompanied by enrichments and/or depletion in key FME tracers (**Deschamps et al., 2013**; **Peters et al., 2017**; **Kodolányi et al., 2012; Scambelluri & Tonarini, 2012; Lafay et al., 2013; Debret et al, 2013b**). During subduction recrystallization, serpentinite can acquire TE, depending on element mobility in aqueous solutions and on fluid–rock compatibility ratio (K_d). Hence, previous studies led to identify the tectonic setting where different TE are added, or removed, from serpentinites (e.g. **Scambelluri & Philippot, 2001; Kodolányi et**

al., 2012; Debret et al., 2013b; Scambelluri et al., 2014; Peters et al., 2017). This allowed to trace back distinct stages in tectonic history of the serpentinites, looking at differences in micro–texture and trace element composition (**Cannaò et al., 2015, 2016**).

Zermatt serpentinite. Major element and REE patterns of the Zermatt serpentinite indicate an origin from a depleted mantle peridotite protolith. The PM–normalized TE composition of such serpentinites (**Figure 10**) shows that most TE (Cs, Rb, Ba, Th, U, K, Sr, Zr, Hf, Ti, Ga, Li, Y, Sc) follow the mantle depletion trend, suggesting their concentrations are largely controlled by depletion via melt extraction in the mantle. Differently, Bi, B, W, Sn, Pb, As, Sb, and Mo show positive anomalies with respect to the mantle depletion trend; some of the above TE also show higher contents with respect to refertilized, plagioclase–impregnated peridotite from the Lanzo massif (**Guarnieri et al., 2012**). Recent work on serpentinites from present–day abyssal and forearcs settings, and from ophiolites pointed out such enrichments can equally be attributed to ocean floor or subduction zone serpentinization (**Niu, 2004**; **Boschi et al., 2008**; **Vils et al., 2009**; **Deschamps et al., 2011, 2012; Kodolányi et al., 2012; Peters et al., 2017**). As such, the positive TE anomalies of the Zermatt serpentinite cannot be attributed to a specific serpentinization environment. The lack of prominent Cs enrichments while B is strongly enriched implies absence of a sedimentary signature, however (**Peters et al., 2017**), and no significant U uptake (**Kodolányi et al., 2012; Deschamps et al. 2013; Peters et al., 2017**) indicates slightly less oxidised serpentinization fluids compared to, e.g., sea water (Langmuir, 1978). This is further supported by W/Mo > 1, since fluid-mediated Mo transport and enrichment is more redox-sensitive than for W for these otherwise geochemically very similar elements (e.g., **Koschinsky and Hein, 2003**; **Mohajerin et al., 2016)**. Molybdenum will thus be less strongly enriched than W by less oxidised fluids (W/Mo = 0.06-0.18 for mid-ocean ridge serpentinites with U = 0.211-1.02 μg g^{-1} in **Jöns et al., 2010**). Overall, such fluid characteristics and resulting fluid signatures are like FME enrichment patterns observed in some ocean floor serpentinites that have been sampled in somewhat deeper parts of the lithospheric mantle at the ocean floor (**Peters et al., 2017**).

During oceanic serpentinization, the original peridotite also exchanges isotopes with seawater. The very low Pb amount in seawater (Pb ~ 0.002 µg/g; **Li, 1982**) does not change significantly the Pb content of serpentinite with respect to the original peridotite (Pb ~ 0.05 µg/g in DM), and does not strongly change the isotopic composition of these rocks. In this respect, the 0.06–0.13 µg/g Pb and the Pb isotopic ratio of the Zermatt serpentinites are within the range of the reference mantle peridotite (DM and unaltered Lanzo levels; Figures 9 and 10). Regarding Sr, the bulk Sr contents of serpentinites are strongly influenced by (1) the presence of clinopyroxene porphyroclasts, which retain most of the bulk Sr content and have a mantle isotopic imprint ($^{87}Sr/^{86}Sr$ ~ 0.7030) and (2) by the amount of Sr introduced by the aqueous fluid hydrating the rock during serpentinization. As clinopyroxene is generally more resistant than olivine to serpentinization, partially serpentinized peridotites will retain most of their mantle isotopic signature and thus have a Sr isotopic composition lying on a mixing line between pristine peridotite and seawater. Since mantle clinopyroxene clasts in the Zermatt serpentinite are scarce (< 5 vol.%), the bulk isotopic composition of these rocks well approximates the composition of the serpentinization fluid. As such, the $^{87}Sr/^{86}Sr$ compositions of the Zermatt serpentinites ($^{87}Sr/^{86}Sr$ = 0.707051-0.708303) imply exchange with Jurassic seawater in accordance with TE data, without further indications for interaction with either sediment–equilibrated fluids in forearc regions or subduction–derived fluids along the subduction interface.

Like the bulk–rock TE composition, rock forming minerals in Zermatt serpentinite display enrichments in B, As, and Sb. These elements are equally stored in antigorite and metamorphic diopside. Antigorite displays a steady increase in HREEs relative to LREEs, and strong enrichments in B, As, and Sb, showing a pattern compatible with oceanic serpentinization of olivine (**Kodolányi et al., 2012**). Similarly, prograde diopside REE patterns likely reflect the composition of the original mantle clinopyroxene, with enrichments of B, W, As, and Sb due to oceanic hydration. Ti–clinohumite shows an enrichment in Nb and Ta up to PM levels, consistent with the high compatibility of high field strength elements in humite–group minerals (**Garrido et al., 2005**). The strong B enrichment in Ti–clinohumite from HP veins suggests its preferential partitioning into the fluid–phase compared to other elements during serpentinite dehydration.

In summary, TE and the Sr–Pb isotopes suggest that the Zermatt serpentinite represents a section of the oceanic slab, which was serpentinized during the Jurassic spreading of the Tethys and still largely retains the original oceanic geochemical signature despite its deep subduction and exhumation during the Alpine orogeny.

Cignana serpentinite. Compared with reference refertilized plagioclase peridotite from Lanzo (**Figure 9**), the Cignana serpentinites show enrichments in Th, U, B, W, Nb, Ta, Be, Sn, As, Sb, and Sr. Like in the Zermatt serpentinite, FME patterns might be related to interaction with seawater–derived and slightly reduced fluids in oceanic environments. However, the elevated Th, Be, Nb, Ta, and Sr contents combined with high As and Sb when compared to the Zermatt serpentinite, suggest inputs from reservoirs other than seawater.

Arsenic and Sb, for instance, are generally acquired in moderate amounts during oceanic serpentinization except for proximity to major hydrothermal sites where significant sulphide precipitation occurs (**Andreani et al., 2014**). Moreover, several recent works suggest that elevated contents of As and Sb can be acquired during subduction and serpentinite emplacement in the accretionary wedge and plate interface (**Hattori & Guillot, 2003**, **2007**; **Hattori et al., 2005**; **Deschamps et al., 2011, 2012; Lafay et al., 2013;**

Scambelluri et al., 2014; **Cannaò et al., 2015, 2016**). **Figure 16a** shows the potential relationships between As and Sb of the Zermatt and Cignana serpentinites compared with eclogite and metasediments from the Lago di Cignana Unit and with some major global reservoirs (GLOSS–II, **Plank, 2014**; depleted mantle, **Rehka & Hofmann, 1997**; Jurassic seawater, **Jones & Jenkyns, 2001**; average continental crust, **Rudnick and Gao, 2003**). While the Zermatt–Saas serpentinite plots near DM and PM (suggesting just oceanic alteration) the Cignana serpentinites display variable increase in their As and Sb budgets with respect to Zermatt–Saas. This enrichment can be either due to (1) an intensive oceanic hydrothermal alteration (**Andreani et al., 2014**) or to (2) exchange with crustal rock reservoirs during subduction (**Lafay et al., 2013; Scambelluri et al., 2014**; **Cannaò et al., 2015, 2016**). The Cignana serpentinite also plots close to the Lago di Cignana eclogite and metasediments, suggesting an exchange of these elements with such rocks during subduction. Furthermore, this enrichment is comparable with that recorded by other HP serpentinites (Voltri) and metaperidotites (Cima di Gagnone) for which the uptake of As and Sb via interaction of crust–derived subduction fluids has shown on textural and geochemical grounds (**Cannaò et al., 2015; 2016; Scambelluri et al., 2014**).

A further discrimination between oceanic and subduction input of FME to serpentinites can be defined by the B vs. Sr diagram (**Figure 16b)**. The diagram shows that oceanic abyssal serpentinites are more enriched in B relative to Sr, whereas the subduction zone serpentinites display an opposite trend. In **Figure 16b**, the Zermatt–Saas serpentinite overlaps the abyssal serpentinite trend whereas the Cignana serpentinite is strongly enriched in Sr with respect to B. This suggests a dual origin for the observed enrichments: prevalently oceanic in the Zermatt serpentinite vs. prevalently subduction–related in the Cignana serpentinite.

Finally, **Figure 16c** shows the concentrations in Th and U within the same suite of Zermatt and Cignana rocks. The strong enrichment in U of abyssal serpentinites has been widely documented as due to interactions with ocean waters (up to 3.2 µg/g; **Bailey and Ragnarsdottir, 1994**; **Kodolányi et al., 2012**; **Deschamps et al., 2013**; **Peters et al., 2017**). The Zermatt serpentinite plots close to the DM and overlies the field of unaltered oceanic Lanzo peridotite and suggests scarce U uptake from seawater, i.e., in slightly reduced environments such as deeper parts of the oceanic mantle (Peters et al., 2017) or at the sea floor. Conversely, the Cignana serpentinite fall along a trend of coupled U and Th enrichment towards crustal reservoirs: a same trend followed by some subduction zone serpentinites (**Deschamps et al., 2013,** and reference therein).

Rock forming minerals in Cignana serpentinite show enrichments like those reported for the bulk rock. Like antigorite from the Zermatt serpentinite, antigorite from the Cignana serpentinite shows an enrichment in heavy– respect to light–REE and enrichments in B, As and Sb, compatible with the oceanic serpentinization of olivine (**Kodolányi et al., 2012**). However, elevated levels of Th and Be in antigorite (present also in diopside) cannot be solely attributed to oceanic serpentinization and, as suggested for bulk rock, might indicate Th and Be enrichment during subduction (**Figure 13**). Ti–clinohumite shows an enrichment of up to 100 PM in Nb and Ta, again consistent with the high compatibility of high field strength elements in humite–group minerals (**Garrido et al., 2005**).

Since dehydration of crustal lithologies during subduction may produce fluids carrying substantial amounts of Sr, Be and possibly Th, the TE data shown in **Figure 16** suggest that the Cignana serpentinites underwent exchange with subduction fluids that increased their budget in Sr, Be and Th with respect to the Zermatt serpentinite, which essentially records an oceanic imprint. The serpentinization environment and process of Cignana can be traced also by Sr and Pb isotopic compositions. **Figure 17** reports the Sr and

Pb isotopic values of Zermatt serpentinites along with the Cignana serpentinite, eclogite and metasediments. Also shown are the DM, MORB, Continental Crust, and GLOSS–II compositions (GLOSS–II; **Plank, 2014**; depleted mantle, **Rehka & Hofmann, 1997**; Jurassic seawater, **Jones & Jenkyns, 2001**; average continental crust, **Rudnick and Gao, 2003**). As previously explained, the Zermatt and Cignana serpentinites underwent intensive (~95 vol.%) serpentinization, which implies that their isotopic composition records that of the serpentinizing fluid. The Sr isotope values of the Zermatt serpentinite overlap with Jurassic seawater ($^{87}Sr/^{86}Sr = 0.7070$), which confirms that serpentinization prevalently occurred in oceanic environment. Similarly, the Cignana serpentinite experienced an oceanic serpentinization, as suggested by B and Cs signatures and by the presence of boudinaged rodingite dykes. However, the more primitive Sr isotopic composition of this serpentinite points to an exchange with a different fluid that may have exchanged with metabasaltic material such as the Cignana eclogite.

To conclude, the Zermatt–Saas serpentinites largely inherit an oceanic signature acquired by interactions with seawater. The Cignana serpentinites were originally exposed near the sea–floor and acquired an oceanic signature still recorded by trace elements such as B, Cs and W. During subduction, fluids equilibrated with altered oceanic crust interacted with the Cignana serpentinites, largely modifying its trace element (prevalently Th, Sr, and Be, and to a lesser extent As and Sb) and Sr and Pb isotopic compositions.

Veins. Based on petrologic evidence the type 1 olivine + Ti–clinohumite veins in Cignana serpentinite formed during subduction, likely resulting from brucite + antigorite dehydration occurring at about 450 °C (reaction 1 in **Figure 14**). The chemical and isotopic compositions of such veins is comparable to that of the host serpentinite (**Figure 9, Figure 13, Figure 16**), which suggests that dehydration of the Cignana serpentinites occurred in a closed system, and infiltration of externally–derived subduction fluids is not indicated.

Consequently, FME enrichment and fluid–rock interaction between the Cignana serpentinite and fluids of crustal origin occurred during the first stages of subduction, i.e., before this dehydration event. It implies that the Cignana serpentinites were associated with subducting oceanic crust of the type cropping out in the nearby Lago di Cignana Unit, already since the first stages of subduction.

According to petrographic observations and to recently published experimental work by **Shen et al. (2015)**, the type 2 Ti–chondrodite veins in the Cignana serpentinites could have crystallized during the UHP metamorphic peak at 3.2 GPa and 600 °C (peak estimates for Cignana eclogites after **Groppo et al., 2009**). Hence, in the Cignana serpentinite, this Ti–chondrodite likely formed after the HP type 1 veins.

The presence of Ti–chondrodite–bearing type 2 veins suggests their formation occurred at PT conditions in–between the brucite–out and antigorite–out dehydration reactions (reactions 1 and 2 in **Figure 14**). The origin of the fluid responsible for type 2 Ti–chondrodite veins cannot thus be related to a specific serpentinite dehydration event, as suggested for type 1 veins. Instead, the fluid might be derived from an external source rich in U, Th, As, and Sb. Furthermore, the bulk REE patterns are strongly controlled by 2–3 % vol. of overly enriched apatite crystals (**Figures 4e and 13**). Although rare in type 2 veins, apatite crystals can account for the bulk LREE enrichment and thus explain its high LREE concentrations.

The Sr–Pb isotopic signature of the Ti–chondrodite vein might help understanding fluid–rock interaction and fluid paths in UHP subduction systems. The comparatively radiogenic Pb–isotope composition (close to GLOSS–II values) in the Ti–chondrodite vein is not yet fully understood. One possibility is that it might indicate a sedimentary/crustal hybridized origin of the UHP fluid generating the vein. However, this should strongly influence the Sr isotopes, making them more radiogenic (as for the cases of Voltri serpentinite and Cima di Gagnone metaperidotite described by Cannaò et al., 2015; 2016), which is not the case.

CONCLUSIONS

We have shown that the eclogite facies serpentinites from Valtournenche (Zermatt–Saas Zone and the serpentinite enveloping the UHP Lago di Cignana Unit) display different metamorphic histories and different metamorphic and trace element signatures.

1. The Zermatt and Cignana serpentinites record different Alpine pressure–temperature paths. The top of the coherent Zermatt–Saas Zone consists of a thin sliver of UHP serpentinites (the Cignana serpentinite). The Zermatt–Saas serpentinite shows formation of metamorphic olivine and Ti–clinohumite–bearing assemblages in rock and vein systems. Overall, development of this paragenesis requires a stage of antigorite + brucite dehydration in the Ti–clinohumite stability field at P–T conditions of about 2–2.5 GPa and 450–500 °C. The serpentinite enveloping the UHP Lago di Cignana Unit shows a first crystallization of olivine + Ti–clinohumite in rocks and veins (type 1 veins) at about 2.0 GPa and 450–500 °C. The Cignana serpentinite also includes Ti–chondrodite veins (type 2) formed at higher pressure and temperature of about 3.0 GPa and 600–650 °C, comparable to the UHP conditions recorded by the nearby UHP Cignana eclogite and metasediments. Type 1 and type 2 veins are both overgrown by later stage Ti–clinohumite.

2. Antigorite + olivine + Ti–clinohumite/chondrodite serpentinites are thus a stable UHP mineral association, being representative of UHP, coesite–facies conditions.

3. Bulk–rock major and trace element data indicate that the Zermatt and the Cignana serpentinites derive from different mantle photoliths, and either represent

two separate units of different oceanic origin, or two sections of heterogeneous oceanic mantle.

4. The fluid–mobile element and isotopic composition of the Cignana serpentinite suggests it experienced geochemical exchange with the nearby Cignana crustal rocks. This geochemical imprint is different from that of the Zermatt serpentinite, which mostly preserves oceanic geochemical characteristics because subduction took place under closed system conditions. This evidence reinforces the hypothesis that the Cignana UHP rocks were tectonically coupled with the surrounding serpentinite during subduction, and shows that the tectonic horizon including the Lago di Cignana Unit and other tectonic slices (Etirol–Levaz, **Beltrando et al., 2010**; Teodulo, **Skora et al., 2015**; Allalin Gabbro, **Bucher & Grapes, 2009**; dismembered sections of Austroalpine domain like Mt. Emilius, Figure 1) behaved as a major discontinuity (plate interface) during exhumation.

ACKNOWLEDGEMENTS

We greatly benefitted from discussions with P. Agard, E. Cannaò, H. Marschall, J. Hermann, D. Rubatto, and all scientists and fellows from the ZIP project (http://www.zip-itn.eu/): discussions within ZIP stimulated this work. We thank A. Risplendente and L. Negretti for technical assistance during the SEM and wavelength-dispersive spectrometry microprobe work. We acknowledge funding by the People Programme (Marie Curie Actions, European Union's Seventh Framework Programme FP7/2007—2013) to the Initial Training Network ZIP (Zooming In-between Plates, REA grant agreement no. 604713). M.S. also acknowledges support from the Italian MIUR and the University of Genova.

REFERENCES

908 Agard, P., Yamato, P., Jolivet, L. & Burov, E. (2009). Exhumation of oceanic blueschists and eclogites in subduction zones: timing and mechanisms. Earth-Science Reviews 92(1), 53–79.

911 Amato, J.M., Johnson, C.M., Baumgartner, L.P. & Beard, B.L. (1999). Rapid exhumation of the Zermatt-Saas ophiolite deduced from high-precision Sm-Nd and Rb-Sr geochronology. Earth and Planetary Science Letters 171(3), 425–438.

914 Andreani, M., Escartin, J., Delacour, A., Ildefonse, B., Godard, M., Dyment, J., Fallick, A.E. & Fouquet, Y. (2014). Tectonic structure, lithology, and hydrothermal signature of the Rainbow massif (Mid□Atlantic Ridge 36° 14′ N). Geochemistry, Geophysics, Geosystems 15(9), 3543-3571.

918 Angiboust, S., Agard, P., Jolivet, L. & Beyssac, O. (2009). The Zermatt-Saas ophiolite: the largest (60-km wide) and deepest (c. 70–80 km) continuous slice of oceanic lithosphere detached from a subduction zone? Terra Nova 21(3), 171–180.

921 Angiboust, S., Agard, P., Raimbourg, H., Yamato, P. & Huet, B. (2011). Subduction interface processes recorded by eclogite-facies shear zones (Monviso, W. Alps). Lithos 127(1), 222–238.

924 Angiboust, S., Agard, P., Yamato, P. & Raimbourg, H. (2012b). Eclogite breccias in a subducted ophiolite: A record of intermediate-depth earthquakes? Geology 40(8), 707–710.

927 Angiboust, S., Pettke, T., De Hoog, J.C., Caron, B. & Oncken, O. (2014). Channelized fluid flow and eclogite-facies metasomatism along the subduction shear zone. Journal of Petrology 55(5), 883–916.

930 Bailey, E.H. & Ragnarsdottir, K.V. (1994). Uranium and thorium solubilities in subduction zone fluids. Earth and Planetary Science Letters 124(1-4), 119-129.

Bearth, P. & Schwander, H. (1981). The post-Triassic sediments of the ophiolite zone Zermatt-Saas Fee and the associated manganese mineralizations. Eclogae Geologicae Helvetiae 74(1), 189–205.

Bearth, P.P. (1967). Die Ophiolithe der Zone von Zermatt-Saas Fee. Kummerly & Frey.

Bebout, G.E. (2007). Metamorphic chemical geodynamics of subduction zones. Earth and Planetary Science Letters 260(3), 373–393.

Beltrando, M., Rubatto, D. & Manatschal, G. (2010). From passive margins to orogens: The link between ocean-continent transition zones and (ultra) high-pressure metamorphism. Geology 38(6), 559–562.

Bideau, D., Hebert, R., Hekinian, R. & Cannat, M. (1991). Metamorphism of deep□seated rocks from the Garrett Ultrafast Transform (East Pacific Rise near 13° 25′ S). Journal of Geophysical Research: Solid Earth 96(B6), 10079-10099.

Bogolepov, V.G. (1970). Problem of serpentinization of ultrabasic rocks. International Geology Review 12(4), 421-432.

Boschi, C., Dini, A., Früh-Green, G.L. & Kelley, D.S. (2008). Isotopic and element exchange during serpentinization and metasomatism at the Atlantis Massif (MAR 30 N): insights from B and Sr isotope data. Geochimica et Cosmochimica Acta 72(7), 1801-1823.

Bostock, M., Hyndman, R., Rondenay, S. & Peacock, S. (2002). An inverted continental moho and serpentinization of the forearc mantle. Nature 417(6888), 536–538.

Bostock, M. (2013). The moho in subduction zones. Tectonophysics 609, 547–557.

Brovarone, A. V., Beyssac, O., Malavieille, J., Molli, G., Beltrando, M. & Compagnoni, R. (2013). Stacking and metamorphism of continuous segments of subducted lithosphere in a high-pressure wedge: The example of Alpine Corsica (France). Earth-Science Reviews 116, 35–56.

Bucher, K. & Grapes, R. (2009). The eclogite-facies Allalin gabbro of the Zermatt–Saas ophiolite, Western Alps: a record of subduction zone hydration. Journal of Petrology, egp035.

Bucher, K., Fazis, Y., Capitani, C.D. & Grapes, R. (2005). Blueschists, eclogites, and decompression assemblages of the Zermatt-Saas ophiolite: High-pressure metamorphism of subducted Tethys lithosphere. American Mineralogist 90(5-6), 821–835.

Cannaò, E., Agostini, S., Scambelluri, M., Tonarini, S. & Godard, M. (2015). B, Sr and Pb isotope geochemistry of high-pressure Alpine metaperidotites monitors fluid-mediated element recycling during serpentinite dehydration in subduction mélange (Cima di Gagnone, Swiss Central Alps). Geochimica et Cosmochimica Acta 163, 80–100.

Cannaò, E., Scambelluri, M., Agostini, S., Tonarini, S. & Godard, M. (2016). Linking serpentinite geochemistry with tectonic evolution at the subduction plate-interface: The Voltri massif case study (Ligurian Western Alps, Italy). Geochimica et Cosmochimica Acta 190, 115–133.

Cannat, M., Mevel, C., Maia, M., Deplus, C., Durand, C., Gente, P., Agrinier, P., Belarouchi, A., Dubuisson, G., Humler, E., et al. (1995). Thin crust, ultramafic exposures, and rugged faulting patterns at the Mid-Atlantic Ridge (22–24 n). Geology 23(1), 49–52.

Coleman, R.G. & Keith, T.E. (1971). A chemical study of serpentinization—Burro Mountain, California. Journal of Petrology 12(2), 311-328.

Dal Piaz, G.V., Bistacchi, A. & Massironi, M. (2003). Geological outline of the Alps. Episodes 26(3), 175-180.

Dal Piaz, G.V. (1992). Alpi dal monte bianco al lago maggiore. guide geologiche regionali. Vol. 3. Societa Geologica Italiana. BE-MA Editrice.

Debret, B., Nicollet, C., Andreani, M., Schwartz, S. & Godard, M. (2013a). Three steps of serpentinization in an eclogitized oceanic serpentinization front (Lanzo Massif–Western Alps). Journal of Metamorphic Geology 31(2), 165–186.

Debret, B., Andreani, M., Godard, M., Nicollet, C., Schwartz, S. & Lafay, R. (2013b). Trace element behaviour during serpentinization/de-serpentinization of an eclogitized oceanic lithosphere: A LA-ICPMS study of the Lanzo Ultramafic Massif (Western Alps). Chemical Geology 357, 117–133.

Deschamps, F., Guillot, S., Godard, M., Andreani, M. & Hattori, K. (2011). Serpentinites act as sponges for fluid-mobile elements in abyssal and subduction zone environments. Terra Nova 23(3), 171–178.

Deschamps, F., Godard, M., Guillot, S., Chauvel, C., Andreani, M., Hattori, K., Wunder, B. & France, L. (2012). Behavior of fluid-mobile elements in serpentines from abyssal to subduction environments: Examples from Cuba and Dominican Republic. Chemical Geology 312, 93-117.

Deschamps, F., Godard, M., Guillot, S. & Hattori, K. (2013). Geochemistry of subduction zone serpentinites: A review. Lithos 178, 96–127.

Ernst, W.G. & Dal Piaz, G.V. (1978). Mineral parageneses of eclogitic rocks and related mafic schists of the Piemonte ophiolite nappe, Breuil-St. Jacques area, Italian Western Alps. American Mineralogist 63(7-8), 621-640.

Forster, M., Lister, G., Compagnoni, R., Giles, D., Hills, Q., Betts, P., Beltrando, M., Tamagno, E. (2004). Mapping of oceanic crust with "HP" to "UHP" metamorphism: The Lago di Cignana Unit (Western Alps). Mapping geology in Italy.

Frezzotti, M., Selverstone, J., Sharp, Z. & Compagnoni, R. (2011). Carbonate dissolution during subduction revealed by diamond-bearing rocks from the Alps. Nature Geoscience 4(10), 703–706.

Garrido, C.J., López Sánchez□Vizcaíno, V., Gómez□Pugnaire, M.T., Trommsdorff, V., Alard, O., Bodinier, J.L. & Godard, M. (2005). Enrichment of HFSE in Chlorite□ Harzburgite produced by high□pressure dehydration of Antigorite□Serpentinite: implications for subduction magmatism. Geochemistry, Geophysics, Geosystems 6(1).

Godard, M., Jousselin, D. & Bodinier, J.L. (2000). Relationships between geochemistry and structure beneath a paleo-spreading centre: a study of the mantle section in the Oman ophiolite. Earth and Planetary Science Letters 180(1), 133-148.

Groppo, C., Beltrando, M. & Compagnoni, R. (2009). The P–T path of the ultra-high-pressure Lago di Cignana and adjoining high-pressure meta-ophiolitic units: insights into the evolution of the subducting Tethyan slab. Journal of Metamorphic Geology 27(3), 207–231.

Guarnieri, L., Nakamura, E., Piccardo, G.B., Sakaguchi, C., Shimizu, N., Vannucci, R. & Zanetti, A. (2012). Petrology, trace element and SR, Nd, Hf isotope geochemistry of the North Lanzo peridotite massif (Western Alps, Italy). Journal of Petrology 53(11), 2259-2306.

Guillong, M., Meier, D.L., Allan, M.M., Heinrich, C.A. & Yardley, B.W. (2008). Appendix A6: SILLS: A MATLAB-based program for the reduction of laser ablation ICP-MS data of homogeneous materials and inclusions. Mineralogical Association of Canada Short Course 40, 328-333.

Guillot, S., Hattori, K.H., de Sigoyer, J., Nägler, T. & Auzende, A.L. (2001). Evidence of hydration of the mantle wedge and its role in the exhumation of eclogites. Earth and Planetary Science Letters 193(1), 115-127.

Guillot, S., Schwartz, S., Reynard, B., Agard, P. & Prigent, C. (2015). Tectonic significance of serpentinites. Tectonophysics 646, 1–19.

Hattori, K.H. & Guillot, S. (2003). Volcanic fronts form as a consequence of serpentinite dehydration in the forearc mantle wedge. Geology 31(6), 525-528.

Hattori, K.H. & Guillot, S. (2007). Geochemical character of serpentinites associated with high- to ultrahigh-pressure metamorphic rocks in the Alps, Cuba, and the Himalayas: Recycling of elements in subduction zones. Geochemistry, Geophysics, Geosystems 8(9).

Hattori, K., Takahashi, Y., Guillot, S. & Johanson, B. (2005). Occurrence of arsenic (V) in forearc mantle serpentinites based on X-ray absorption spectroscopy study. Geochimica et Cosmochimica Acta 69(23), 5585–5596.

Hermann, J., Müntener, O. & Scambelluri, M. (2000). The importance of serpentinite mylonites for subduction and exhumation of oceanic crust. Tectonophysics 327(3), 225–238.

Ionov, D. A., Savoyant, L. & Dupuy, C. (1992). Application of the ICP□MS technique to trace element analysis of peridotites and their minerals. Geostandards and Geoanalytical Research 16(2), 311-315.

Iwamori, H. (1998). Transportation of H2O and melting in subduction zones. Earth and Planetary Science Letters, 160(1), 65-80.

Jochum, K.P., Seufert, H.M. & Thirlwall, M.F. (1990). High-sensitivity Nb analysis by spark-source mass spectrometry (SSMS) and calibration of XRF Nb and Zr. Chemical Geology 81(1-2), 1-16.

John, T., Scambelluri, M., Frische, M., Barnes, J.D. & Bach, W. (2011). Dehydration of subducting serpentinite: implications for halogen mobility in subduction zones and the deep halogen cycle. Earth and Planetary Science Letters 308(1), 65–76.

Jones, C.E. & Jenkyns, H.C. (2001). Seawater strontium isotopes, oceanic anoxic events, and seafloor hydrothermal activity in the Jurassic and Cretaceous. American Journal of Science 301(2), 112–149.

Jöns, N., Bach, W., & Klein, F. (2010). Magmatic influence on reaction paths and element transport during serpentinization. Chemical Geology, 274(3–4), 196–211.

Kelemen, P. B., Hanghøj, K., & Greene, A. R. (2003). One view of the geochemistry of subduction-related magmatic arcs, with an emphasis on primitive andesite and lower crust. Treatise on geochemistry, 3, 659.

Kendrick, M.A., Scambelluri, M., Honda, M. & Phillips, D. (2011). High abundances of noble gas and chlorine delivered to the mantle by serpentinite subduction. Nature Geoscience 4(11), 807–812.

Kendrick, M.A., Hémond, C., Kamenetsky, V.S., Danyushevsky, L., Devey, C.W., Rodemann, T. & Perfit, M.R. (2017). Seawater cycled throughout Earth's mantle in partially serpentinized lithosphere. Nature Geoscience 10(3), 222-228.

Kodolányi, J. & Pettke, T. (2011). Loss of trace elements from serpentinites during fluid-assisted transformation of chrysotile to antigorite—An example from Guatemala. Chemical Geology 284(3), 351-362.

Kodolányi, J., Pettke, T., Spandler, C., Kamber, B.S. & Gméling, K. (2012). Geochemistry of ocean floor and fore-arc serpentinites: constraints on the ultramafic input to subduction zones. Journal of Petrology 53(2), 235-270.

Koschinsky, A., & Hein, J. R. (2003). Uptake of elements from seawater by ferromanganese crusts: Solid-phase associations and seawater speciation. Marine Geology, 198(3–4), 331–351.

Lafay, R., Deschamps, F., Schwartz, S., Guillot, S., Godard, M., Debret, B. and Nicollet, C. (2013). High-pressure serpentinites, a trap-and-release system controlled by metamorphic conditions: Example from the piedmont zone of the western alps. Chemical Geology 343, 38–54.

Langmuir, D. (1978). Uranium solution-mineral equilibria at low temperatures with applications to sedimentary ore deposits. Geochimica et Cosmochimica Acta, 42(6), 547–569.

Li, X.-P., Rahn, M. & Bucher, K. (2004). Serpentinites of the Zermatt Saas ophiolite complex and their texture evolution. Journal of Metamorphic Geology 22(3), 159–177.

Li, Y.H. (1982). A brief discussion on the mean oceanic residence time of elements. Geochimica et Cosmochimica Acta 46(12), 2671-2675.

Sánchez-Vizcaíno, V.L., Gómez-Pugnaire, M.T., Garrido, C.J., Padrón-Navarta, J.A. & Mellini, M. (2009). Breakdown mechanisms of titanclinohumite in antigorite serpentinite (Cerro del Almirez massif, S. Spain): A petrological and TEM study. Lithos 107(3), 216-226.

Marschall, H.R., Wanless, V.D., Shimizu, N., von Strandmann, P.A.P., Elliott, T. & Monteleone, B.D. (2017). The boron and lithium isotopic composition of mid-ocean ridge basalts and the mantle. Geochimica et Cosmochimica Acta 207, 102-138.

McDonough, W.F. & Sun, S.S. (1995). The composition of the Earth. Chemical geology 120(3-4), 223-253.

Mohajerin, T. J., Helz, G. R., & Johannesson, K. H. (2016). Tungsten-molybdenum fractionation in estuarine environments. Geochimica et Cosmochimica Acta, 177, 105–119.

Müntener, O., Pettke, T., Desmurs, L., Meier, M. & Schaltegger, U. (2004). Refertilization of mantle peridotite in embryonic ocean basins: trace element and Nd isotopic evidence and implications for crust–mantle relationships. Earth and Planetary Science Letters 221(1), 293-308.

Niu, Y. (2004). Bulk-rock major and trace element compositions of abyssal peridotites: implications for mantle melting, melt extraction and post-melting processes beneath mid-ocean ridges. Journal of Petrology 45(12), 2423-2458.

Paulick, H., Bach, W., Godard, M., De Hoog, J.C.M., Suhr, G. & Harvey, J. (2006). Geochemistry of abyssal peridotites (Mid-Atlantic Ridge, 15 20′ N, ODP Leg 209): implications for fluid/rock interaction in slow spreading environments. Chemical Geology 234(3), 179-210.

Pelletier, L. & Müntener, O. (2006). High-pressure metamorphism of the Lanzo peridotite and its oceanic cover, and some consequences for the Sesia–Lanzo zone (north-western Italian Alps). Lithos, 90(1), 111-130.

Peters, D. & Pettke, T. (2017). Evaluation of Major to Ultra Trace Element Bulk Rock Chemical Analysis of Nanoparticulate Pressed Powder Pellets by LA□ICP□MS. Geostandards and Geoanalytical Research 41(1), 5-28.

Peters, D., Bretscher, A., John, T., Scambelluri, M. & Pettke, T. (2017). Fluid-mobile elements in serpentinites: Constraints on serpentinization environments and element cycling in subduction zones. Chemical Geology 466, 654-666.

Pettke, T., Oberli, F., Audétat, A., Guillong, M., Simon, A.C., Hanley, J. J. & Klemm, L.M. (2012). Recent developments in element concentration and isotope ratio analysis of individual fluid inclusions by laser ablation single and multiple collector ICP-MS. Ore Geology Reviews 44, 10-38.

Piccardo, G.B. (2008). The Jurassic Ligurian Tethys, a fossil ultraslow□spreading ocean: the mantle perspective. Geological Society, London, Special Publications 293(1), 11-34.

Plank, T. (2014). The chemical composition of subducting sediments. Treatise on geochemistry 4, 607-629.

Rampone, E. & Piccardo, G.B. (2000). The ophiolite-oceanic lithosphere analogue: new insights from the Northern Apennines (Italy). SPECIAL PAPERS-GEOLOGICAL SOCIETY OF AMERICA, 21-34.

Rampone, E., Romairone, A. & Hofmann, A.W. (2004). Contrasting bulk and mineral chemistry in depleted mantle peridotites: evidence for reactive porous flow. Earth and Planetary Science Letters 218(3), 491-506.

Rampone, E., Borghini, G., Romairone, A., Abouchami, W., Class, C. & Goldstein, S.L. (2014). Sm–Nd geochronology of the Erro-Tobbio gabbros (Ligurian Alps, Italy): insights into the evolution of the Alpine Tethys. Lithos 205, 236-246.

Ranero, C. & Sallares, V. (2004). Geophysical evidence for hydration of the crust and mantle of the Nazca plate during bending at the North Chile trench. Geology 32(7), 549–552.

Rebay, G., Spalla, M. & Zanoni, D. (2012). Interaction of deformation and metamorphism during subduction and exhumation of hydrated oceanic mantle: Insights from the Western Alps. Journal of Metamorphic Geology 30(7), 687–702.

Rebay, G., Zanoni, D., Langone, A., Luoni, P., Tiepolo, M. & Spalla, M.I. (2017). Dating of ultramafic rocks from the Western Alps ophiolites discloses Late Cretaceous subduction ages in the Zermatt-Saas Zone. Geological Magazine, 1-18.

Reddy, S., Wheeler, J. & Cliff, R. (1999). The geometry and timing of orogenic extension: an example from the Western Italian Alps. Journal of Metamorphic Geology 17, 573–590.

Rehka, M. & Hofmann, A.W. (1997). Recycled ocean crust and sediment in Indian Ocean MORB. Earth and Planetary Science Letters 147(1), 93-106.

Reinecke, T. (1991). Very-high-pressure metamorphism and uplift of coesite-bearing metasediments from the Zermatt-Saas Zone, Western Alps. European Journal of Mineralogy, 7–18.

Reinecke, T. (1998). Prograde high-to ultrahigh-pressure metamorphism and exhumation of oceanic sediments at Lago di Cignana, Zermatt-Saas Zone, Western Alps. Lithos 42(3), 147–189.

Reynard, B. (2013). Serpentine in active subduction zones. Lithos 178, 171–185.

Rubatto, D., Gebauer, D. & Fanning, M. (1998). Jurassic formation and Eocene subduction of the Zermatt–Saas-Fee ophiolites: implications for the geodynamic evolution of the Central and Western Alps. Contributions to Mineralogy and Petrology 132(3), 269–287.

Rudnick, R.L. & Gao, S. (2003). Composition of the continental crust. Treatise on geochemistry 3, 659.

Rüpke, L. H., Morgan, J. P., Hort, M., & Connolly, J. A. (2004). Serpentine and the subduction zone water cycle. Earth and Planetary Science Letters, 223(1), 17-34.

Ryan, J. & Chauvel, C. (2014). 3.13 - the subduction-zone filter and the impact of recycled materials on the evolution of the mantle. In: Holland, H. D., Turekian, K. K. (Eds.), Treatise on Geochemistry (Second Edition), second edition. Elsevier, Oxford, pp. 479 – 508.

Sánchez-Vizcaíno, V.L., Trommsdorff, V., Gómez-Pugnaire, M., Garrido, C., Müntener, O. & Connolly, J. (2005). Petrology of titanian clinohumite and olivine at the high-pressure breakdown of antigorite serpentinite to chlorite harzburgite (Almirez Massif, S. Spain). Contributions to Mineralogy and Petrology 149(6), 627–646.

Savov, I.P., Ryan, J.G., D'Antonio, M., Kelley, K. & Mattie, P. (2005). Geochemistry of serpentinized peridotites from the Mariana forearc conical seamount, ODP leg 125: Implications for the elemental recycling at subduction zones. Geochemistry, Geophysics, Geosystems 6(4).

Scambelluri, M. & Philippot, P. (2001). Deep fluids in subduction zones. Lithos 55(1), 213-227.

Scambelluri, M. & Rampone, E. (1999). Mg-metasomatism of oceanic gabbros and its control on Ti-clinohumite formation during eclogitization. Contributions to Mineralogy and Petrology, 135(1), 1-17.

Scambelluri, M. & Tonarini, S. (2012). Boron isotope evidence for shallow fluid transfer across subduction zones by serpentinized mantle. Geology 40(10), 907–910.

Scambelluri, M., Müntener, O., Hermann, J., Piccardo, G.B. & Trommsdorff, V. (1995). Subduction of water into the mantle: history of an alpine peridotite. Geology 23(5), 459–462.

Scambelluri, M., Müntener, O., Ottolini, L., Pettke, T.T. & Vannucci, R. (2004). The fate of B, Cl and Li in the subducted oceanic mantle and in the antigorite breakdown fluids. Earth and Planetary Science Letters 222(1), 217–234.

Scambelluri, M., Pettke, T., Rampone, E., Godard, M. & Reusser, E. (2014). Petrology and trace element budgets of high-pressure peridotites indicate subduction dehydration of serpentinized mantle (Cima di Gagnone, Central Alps, Switzerland). Journal of Petrology 55(3), 459–498.

Scambelluri, M., Pettke, T. & Cannaò, E. (2015). Fluid-related inclusions in Alpine high-pressure peridotite reveal trace element recycling during subduction-zone dehydration of serpentinized mantle (Cima di Gagnone, Swiss Alps). Earth and Planetary Science Letters 429, 45–59.

Schmidt, M.W. & Poli, S. (1998). Experimentally based water budgets for dehydrating slabs and consequences for arc magma generation. Earth and Planetary Science Letters 163(1), 361–379.

Schwartz, S., Allemand, P., & Guillot, S. (2001). Numerical model of the effect of serpentinites on the exhumation of eclogitic rocks: insights from the Monviso ophiolitic massif (Western Alps). Tectonophysics, 342(1), 193-206.

Shen, T., Hermann, J., Zhang, L., Lü, Z., Padrón-Navarta, J.A., Xia, B. & Bader, T. (2015). UHP metamorphism documented in Ti-chondrodite-and Ti-clinohumite-bearing serpentinized ultramafic rocks from Chinese Southwestern Tianshan. Journal of Petrology 56(7), 1425–1458.

Skora, S., Mahlen, N., Johnson, C., Baumgartner, L., Lapen, T., Beard, B. & Szilvagyi, E. (2015). Evidence for protracted prograde metamorphism followed by rapid exhumation of the Zermatt-Saas Fee ophiolite. Journal of Metamorphic Geology 33(7), 711–734.

Snow, J. E., & Dick, H. J. B. (1995). Pervasive magnesium loss by marine weathering of peridotite. Geochimica et Cosmochimica Acta, 59(20), 4219–4235.

Spandler, C. & Pirard, C. (2013). Element recycling from subducting slabs to arc crust: A review. Lithos 170, 208-223.

Tartarotti, P., Festa, A., Benciolini, L. & Balestro, G. (2017). Record of Jurassic mass transport processes through the orogenic cycle: Understanding chaotic rock units in the high-pressure Zermatt-Saas ophiolite (Western Alps). Lithosphere 9(3), 399-407.

Todt, W., Cliff, R. A., Hanser, A. & Hofmann, A.W. (1996). Evaluation of a 202Pb–205Pb Double Spike for High□Precision Lead Isotope Analysis. Earth processes: reading the isotopic code, 429-437.

Ulmer, P. & Trommsdorff, V. (1995). Serpentine stability to mantle depths and subduction-related magmatism. Science 268 (5212), 858–861.

Vils, F., Tonarini, S., Kalt, A. & Seitz, H.M. (2009). Boron, lithium and strontium isotopes as tracers of seawater–serpentinite interaction at Mid-Atlantic ridge, ODP Leg 209. Earth and Planetary Science Letters 286(3), 414-425.

Weber, S. & Bucher, K. (2015). An eclogite-bearing continental tectonic slice in the Zermatt–Saas high-pressure ophiolites at Trockener Steg (Zermatt, Swiss Western Alps). Lithos 232, 336–359.

Zanoni, D., Rebay, G., Bernardoni, J. & Spalla, M.I. (2012). Using multiscale structural analysis to infer high-/ultrahigh-pressure assemblages in subducted rodingites of the Zermatt-Saas Zone at Valtournanche, Italy. Journal of the Virtual Explorer 41, 2-30.

Zanoni, D., Rebay, G. & Spalla, M.I. (2016). Ocean floor and subduction record in the Zermatt□Saas rodingites, Valtournanche, Western Alps. Journal of Metamorphic Geology 34(9), 941-961.

Figures:

1) Simplified geological sketch and block diagram of the Western Alps around the Zermatt–Saas Zone (redrawn after **Dal Piaz, 1992**). **Upper Austroalpine outliers**: DB = Dent Blanche, VP = Valpelline Unit, MM = Mt. Mary, P = Pillonet; **Sesia-Lanzo Inliers (SL)**: II–DK = Dioritic–kinzigitic, Gm = Gneiss Minuti, Emc = Eclogitic Micascist; **Inner Penninic**: MR = Monte Rosa, AB = Arcesa–Brusson, GP = Gran Paradiso; **Mid Penninic**: SB = Grand St. Bernard; **Outer Penninic**: VA = Valais Zone, PF = Penninic Front; **Helvetic (HE)**: MB = Mt. Blanc; **Piemonte Zone**: CO = Combin, ZS = Zermatt–Saas, A = Atrona; **Lower Austroalpine Outliers**: EM = Mt. Emilius, GR = Glacier–Rafray, S = Santanel, TP = Tour Ponton, AR = Acque Rosse, E = Etirol–Levaz, C = Lago di Cignana Unit, Ch = Chatillon, SV = St. Vincent; **major Alpine faults**: SF = Simplon Fault, CL = Canavese Line, ARF = Aosta–Ranzola Fault.
2) Simplified geologic sketch and profile (A–A'–A'') of the Lago di Cignana Unit, modified after **Forster et al. (2004)** and **Groppo et al. (2009)**. (1) Austroalpine domain (Arolla Unit), (2) Combine Zone, (3) Pancherot Unit. Zermatt–Saas Zone: (4) Prasitites with eclogites, (5) Mg–Al metagabbros, (6) UHP Fe–Ti gabbros and metasediments of the Lago di Cignana Unit and (7) serpentinites.
3) PT path for the Lago di Cignana Unit (**Groppo et al., 2009**) and geothermobarometric estimates for the Zermatt–Saas Zone eclogites (**Angiboust et al., 2009; Groppo et al., 2009**) and serpentinites (**Rebay et al., 2012**).
4) Representative microstructures of Zermatt (a, b. c) and Cignana (d, e, f, g, h.) serpentinites and Ti–rich veins. **Zermatt serpentinite**: (a.) HP foliation in the Zermatt serpentinite wrapping a relic of mantle clinopyroxene; (b.) serpentinite with bastite after mantle pyroxene; (c.) fragment of Ti–clinohumite + olivine + magnetite

vein embedded in serpentinite. **Cignana serpentinite**: (d.) Cignana serpentinite displaying a main foliation defined by elongated domains of HP metamorphic rock–forming olivine and metamorphic diopside; (e.) type 1 Ti–clinohumite vein hosting large (3–5 mm) crystals of olivine, Ti–clinohumite, chlorite, diopside and magnetite; (f.) type 2 Ti–chondrodite vein. Ti–chondrodite occurs with chlorite as 0.5–1 mm–sized, isolated crystals, filled with solid inclusions of ilmenite, zircon and REE–bearing phases. Finer Ti–clinohumite crystals grow at the expense of former Ti–chondrodite; (g.) mm–sized aggregates of apatite rich in solid and fluid inclusions; (h.) Metamorphic diopside crystals containing elongated fluid inclusions.

5) Representative microstructures from the Lago di Cignana Unit. (a.) Coesite–bearing eclogite. An omphacite + rutile foliation wraps around large, inclusion-bearing garnet porphyroclasts. Coesite occurs as inclusion in garnet; (b.) Coesite–bearing garnet and tourmaline quartzite. Note the large poikiloblasts of garnet and tourmaline with quartz inclusions; (c.) Coesite– and microdiamond–bearing garnet Mn–quartzite; (d.) Coesite inclusion in garnet from Mn–quartzite; (e.) Phengite, epidote and calcite from a garnet calcschist; (f.) Poikilitic garnet porphyroclast with quartz inclusions in garnet calcschist.

6) Major element plots (FeO vs MgO and Al_2O_3 vs CaO) for the Zermatt serpentinites and for the Cignana serpentinites and veins. FeO vs MgO: contours are Mg# = molar Mg/(Mg+Fe). Al_2O_3 vs CaO: the shaded areas refer to the mantle depletion trend.

7) Cr vs Ni plot for the Zermatt serpentinites and for the Cignana serpentinites and veins. Shaded areas are for Alpine eclogites (Cignana, this work; Monviso, **Angiboust et al., 2012**), gabbroic dykelets (Voltri, **Scambelluri & Rampone, 1999**), and peridotites (Lanzo, **Müntener et al., 2004; Guarnieri et al., 2012**). Note that the Ti–chondrodite

(orange diamond) and the Ti–clinohumite veins (yellow diamonds) fall within the peridotite area.

8) C1 Chondrite–normalized (**McDonough and Sun, 1995**) REE patterns of bulk–rock from eclogite and metasediments from the UHP Lago di Cignana Unit, Cignana and Zermatt serpentinites and Cignana Ti–bearing veins. Shaded areas are for fresh plagioclase peridotite (orange) and spinel harzburgites (blue) from the Lanzo Massif (**Guarneri et al, 2012**)).

9) PM–normalized (**McDonough and Sun, 1995**; B and Li after **Marschall et al., 2017**) TE patterns of bulk–rock (PPP data used from Table 1) from eclogite and metasediments from the UHP Lago di Cignana Unit, Cignana and Zermatt serpentinites, and Cignana Ti–bearing veins. Shaded areas are for fresh plagioclase peridotite from the Lanzo Massif (orange; **Guarneri et al, 2012**) and the mantle depletion trend (blue).

10) $^{206}Pb/^{204}Pb$ and $^{87}Sr/^{86}Sr$ values of analysed samples from the Lago di Cignana Unit, Cignana serpentinites and veins and Zermatt serpentinites. Values from GLOSS–II (**Plank, 2014**), depleted mantle (**Rehka & Hofmann, 1997**), Jurassic seawater (**Jones & Jenkyns, 2001**) and average continental crust (**Rudnick and Gao, 2003**) are reported for comparison.

11) Mineral analyses of serpentine and olivine from the Zermatt serpentinite, the Cignana serpentinite, and the Ti–bearing veins. Serpentine from Zermatt has higher Mg# and lower Al content that serpentine from Cignana. Mg# in Zermatt olivine is comparable with serpentine from the same locality. Olivine from the Cignana serpentinite and Ti–clinohumite vein have similar Mg#, lower than in the Zermatt serpentinite.

12) Mineral analyses of Ti–chondrodite and Ti–clinohumite from the Cignana serpentinite veins and from the Zermatt serpentinite. Note the lower Ti content of both Ti–

chondrodite and Ti–clinohumite from the Zermatt–serpentinite with respect to Cignana serpentinite veins. Mineral analyses from **Scambelluri & Rampone (1999)** and **Shen et al., (2014)** reported for comparison.

13) REE and TE composition of antigorite, diopside, Ti–clinohumite and apatite from the Cignana and Zermatt serpentinites.

14) Pressure–Temperature diagram with the stability field of Ti–clinohumite (light orange) and Ti–chondrodite (dark orange) in serpentinite systems. The main reaction lines involving Ti–clinohumite and Ti–chondrodite and the quartz to coesite transition lines are from **Shen et al. (2015).** The black arrow corresponds to the PT path of the Lago di Cignana Unit (**Groppo et al., 2009**). The dashed grey lines are the geothermal gradients for cold (5–7 °C/km) and hot (20 °C/km) subduction. Cignana type 1 veins formed during the prograde path, after the partial dehydration of the Cignana serpentinite. Type 2 veins formed at peak UHP conditions, in the stability field of Ti–chondrodite. Type 1 and 2 veins recrystallized during retrograde decompression in the stability field of Ti–clinohumite.

15) Petrogenetic sequence summarizing and comparing the overall evolution of the Zermatt and Cignana serpentinite and the Lago di Cignana Unit.

16) As vs Sb, Sr vs B, and U vs Th plots of analysed samples from the Lago di Cignana Unit, Cignana serpentinites and veins and Zermatt serpentinites. Shaded area from Voltri (**Cannaò et al., 2016**), Cima di Gagnone (CdG; **Scambelluri et al., 2014**; **Cannaò et al., 2015**), Subduction zone (SZ serp) and abyssal serpentinites (**Deschamps et al., 2013** and references therein) and Lanzo peridotite (**Guarnieri et al., 2012**).

17) Initial $^{206}Pb/^{204}Pb$ vs $^{87}Sr/^{86}Sr$, shows a mixing line between Zermatt serpentinite and a fluid of composition comparable with Cignana eclogite (Sample LCG1401), Continental

Crust (**Rudnick and Gao, 2003**) and GLOSS–II (Plank, 2014). Shaded area from Voltri (**Cannaò et al., 2016**), Cima di Gagnone (CdG; **Cannaò et al., 2015**). Values from GLOSS–II (**Plank, 2014**), depleted mantle (**Rehka & Hofmann, 1997**), Jurassic seawater (**Jones & Jenkyns, 2001<**), and average continental crust (**Rudnick and Gao, 2003**) are reported for comparison.

Tables

1) Lists of collected samples and mineral assemblages of the Lago di Cignana Unit and of the Cignana and Zermatt serpentinite.
2) Major (wt.%) and Trace element (μg/g) composition of eclogite and metasediments from the Lago di Cignana Unit, Cignana serpentinites and Ti–bearing veins and of Zermatt serpentinite. Samples were analysed for major elements (d.l. = 0.01 wt.%) and V (d.l. 5 μg/g), Be, Sr, Zr (d.l. 2 μg/g), Sc, Y, and Ba (d.l. 1 μg/g) by means of Fusion-ICP-MS at Act-Lab, Canada. Trace elements were analysed by liquid ICP-MS at Geosciences Montpellier (France). Detection limits can be found in **Godard et al. (2000)**. Furthermore, all samples were analysed for major and trace element by PPP-LA-ICP-MS at the University of Bern.
3) Pb and Sr isotopic composition of selected samples from the Lago di Cignana Unit, the Cignana serpentinite and the Zermatt–Saas Zone serpentinite. All values are reported as observed (obs.) and as corrected (corr.) for an age of 40 Ma.
4) Representative electron microprobe analyses of mineral phases from the UHP eclogite of the Lago di Cignana Unit.
5) Representative electron microprobe analyses of mineral phases from the UHP quartzite of the Lago di Cignana Unit.
6) Representative electron microprobe analyses of mineral phases from the UHP calcschist of the Lago di Cignana Unit.

7) Representative electron microprobe analyses of mineral phases from the Cignana serpentinite.

8) Representative electron microprobe analyses of mineral phases from Ti–chondrodite and Ti–clinohumite veins hosted within Cignana serpentinite.

9) Representative electron microprobe analyses of mineral phases from the Zermatt serpentinite.

10) Representative laser ablation in–situ trace element analyses of mineral phases from the UHP eclogite and metasediments of the Lago di Cignana Unit. All data are reported in µg/g.

11) Representative laser ablation in–situ trace element analyses of mineral phases from the Cignana serpentinite. All data are reported in µg/g.

12) Representative laser ablation in–situ trace element analyses of mineral phases from Ti–chondrodite and Ti–clinohumite veins hosted in the Cignana serpentinite. All data are reported in µg/g.

13) Representative laser ablation in–situ trace element analyses of mineral phases from the Zermatt serpentinite. All data are reported in µg/g.

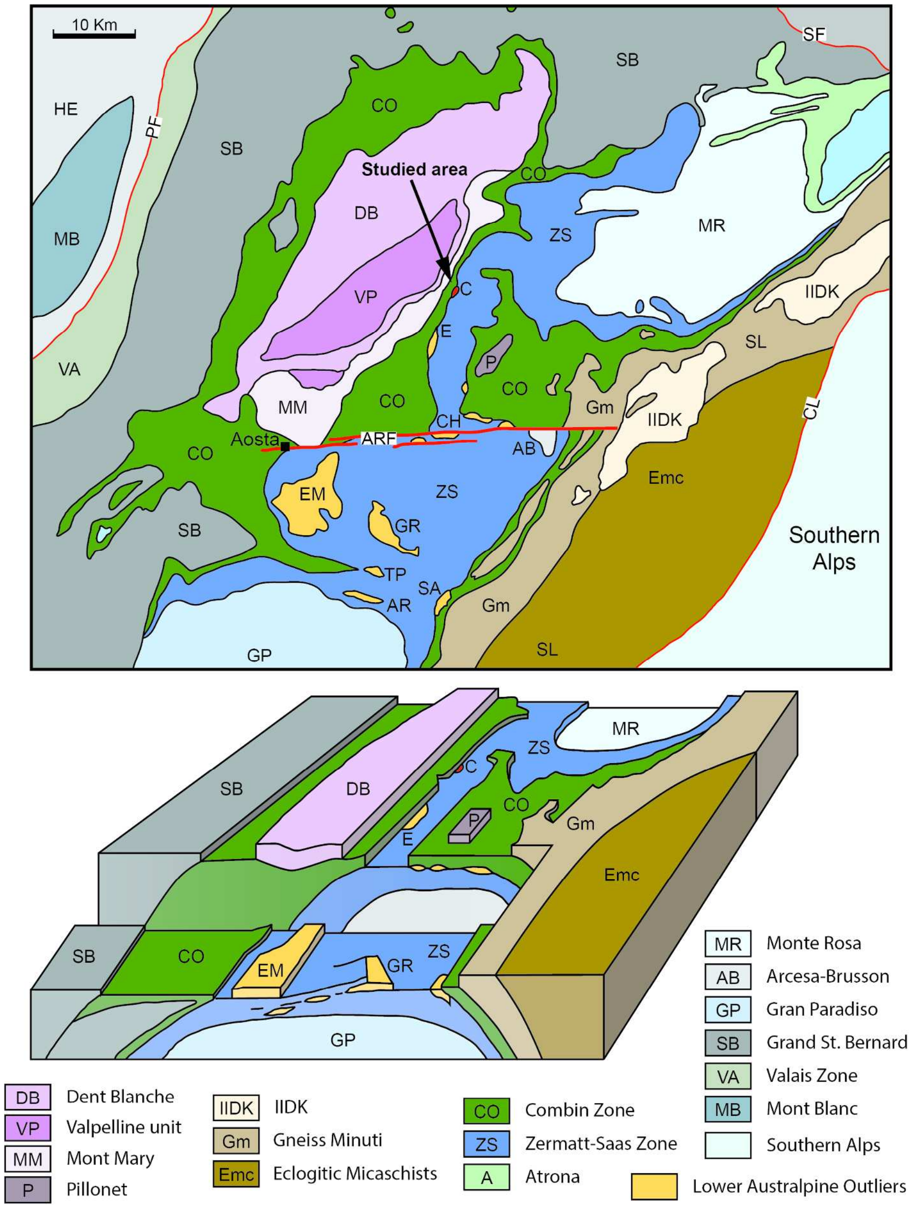

Figure 1 - Simplified geological sketch and block diagram of the Western Alps around the Zermatt–Saas Zone (redrawn after Dal Piaz, 1992). Upper Austroalpine outliers: DB = Dent Blanche, VP = Valpelline Unit, MM = Mt. Mary, P = Pillonet; Sesia-Lanzo Inliers (SL): II–DK = Dioritic–kinzigitic, Gm = Gneiss Minuti, Emc = Eclogitic Micascist; Inner Pennidic: MR = Monte Rosa, AB = Arcesa–Brusson, GP = Gran Paradiso; Mid Penninic: SB = Grand St. Bernard; Outer Penninic: VA = Valais Zone, PF = Penninic Front; Helvetic (HE): MB = Mt. Blanc; Piemonte Zone: CO = Combin, ZS = Zermatt–Saas, A = Atrona; Lower Austroalpine Outliers: EM = Mt. Emilius, GR = Glacier–Rafray, S = Santanel, TP = Tour Ponton, AR = Acque Rosse, E = Etirol–Levaz, C = Lago di Cignana Unit, Ch = Chatillon, SV = St. Vincent; major Alpine faults: SF = Simplon Fault, CL = Canavese Line, ARF = Aosta–Ranzola Fault.

197x261mm (300 x 300 DPI)

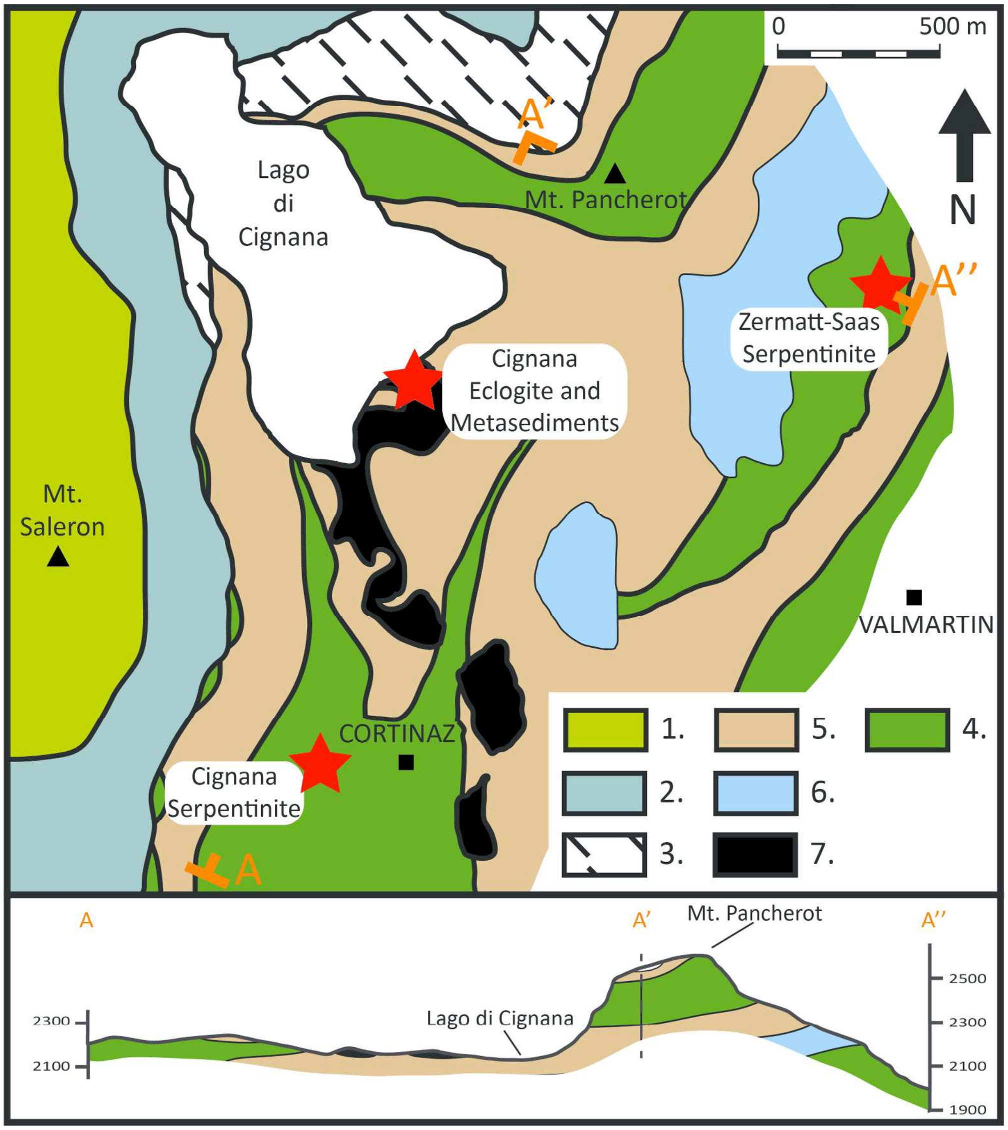

Figure 2 - Simplified geologic sketch and profile (A–A'–A'') of the Lago di Cignana Unit, modified after Forster et al. (2004) and Groppo et al. (2009). (1) Austroalpine domain (Arolla Unit), (2) Combine Zone, (3) Pancherot Unit. Zermatt–Saas Zone: (4) Prasitites with eclogites, (5) Mg–Al metagabbros, (6) UHP Fe–Ti gabbros and metasediments of the Lago di Cignana Unit and (7) serpentinites.

211x237mm (300 x 300 DPI)

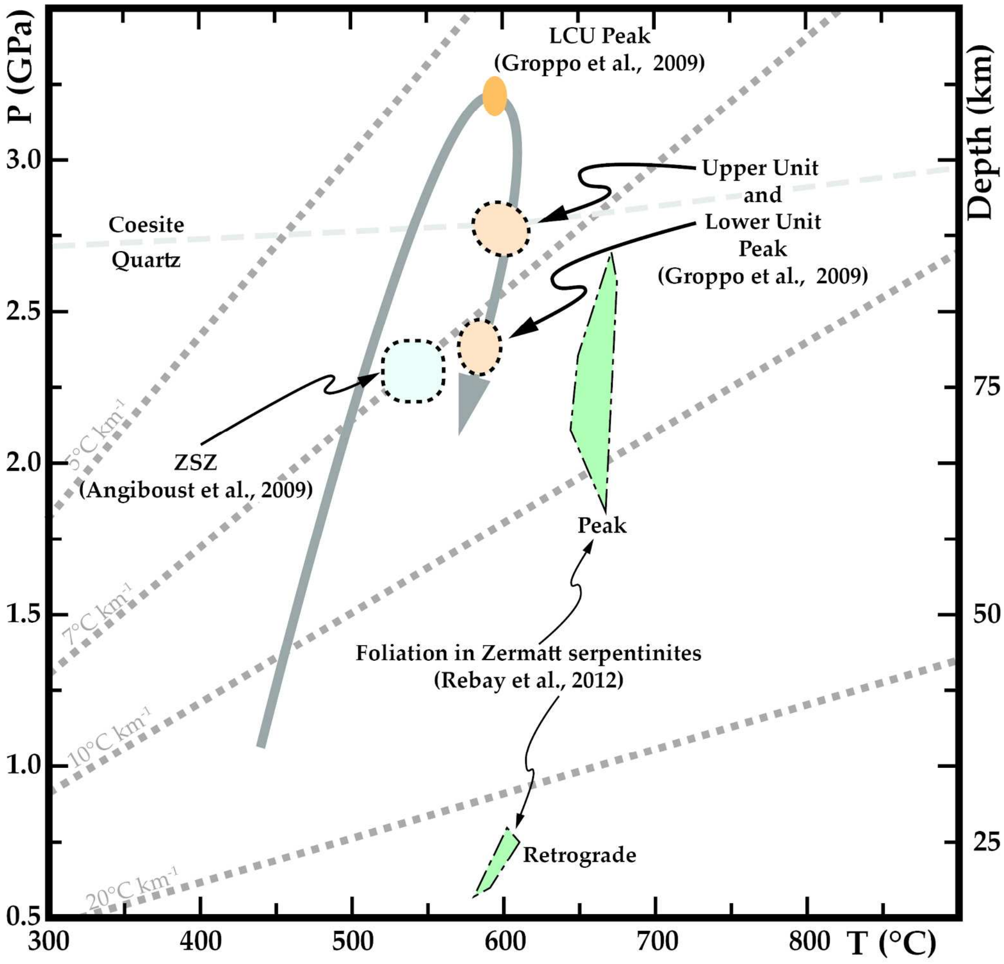

Figure 3 - PT path for the Lago di Cignana Unit (Groppo et al., 2009) and geothermobarometric estimates for the Zermatt–Saas Zone eclogites (Angiboust et al., 2009; Groppo et al., 2009) and serpentinites (Rebay et al., 2012).

187x180mm (300 x 300 DPI)

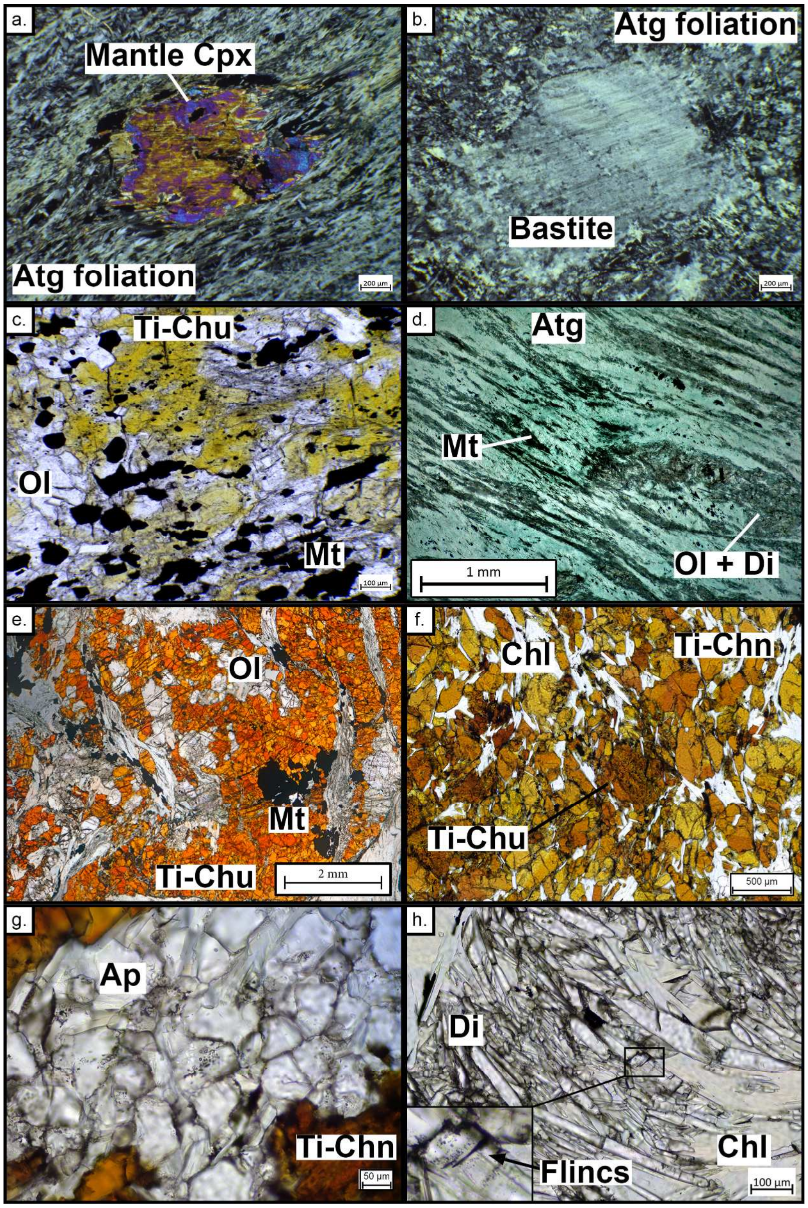

Figure 4 - Representative microstructures of Zermatt (a., b. and c.) and Cignana (d., e., f., g. and h.) serpentinites and Ti–rich veins. Zermatt serpentinite: (a.) HP foliation in the Zermatt serpentinite wrapping a relic of mantle clinopyroxene; (b.) serpentinite with bastite after mantle pyroxene and serpentine + magnetite mesh structure after mantle olivine; (c.) fragment of Ti–clinohumite + olivine + magnetite vein embedded in serpentinite. Cignana serpentinite: (d.) Cignana serpentinite displaying a main foliation defined by elongated domains of HP metamorphic rock–forming olivine and diopside; (e.) type 1 Ti–clinohumite vein hosting large (3–5 mm) crystals of olivine, Ti–clinohumite, chlorite, diopside and magnetite; (f.) type 2 Ti–chondrodite vein. Ti–chondrodite occurs with chlorite as 0.5–1 mm–sized, isolated crystals, filled with solid inclusions of ilmenite, zircon and REE–bearing phases. Finer Ti–clinohumite crystals grow at the expenses of former Ti–chondrodite; (g.) mm–sized aggregates of apatite rich in solid and fluid inclusions; (h.) Diopside crystals containing elongated fluid inclusions.

180x270mm (300 x 300 DPI)

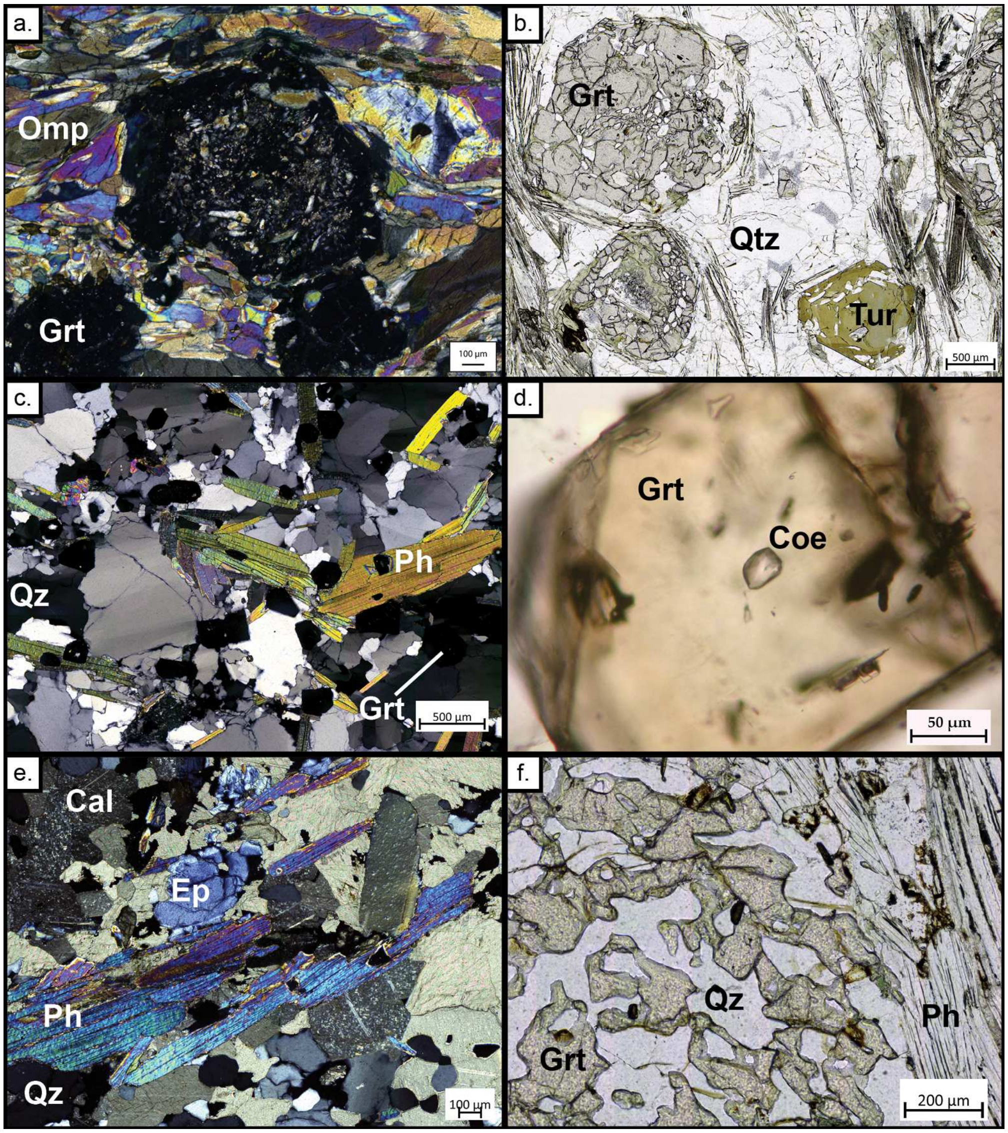

Figure 5 - Representative microstructures from the Lago di Cignana Unit. (a.) Coesite–bearing eclogite. Large, inclusion-bearing garnet porphyroclasts are wrapped around an omphacite + rutile foliation. Coesite occurs as inclusion in garnet; (b.) Coesite–bearing garnet and tourmaline quartzite. Note the large poikiloblasts of garnet and tourmaline with quartz inclusions; (c.) Coesite– and microdiamond–bearing garnet Mn–quartzite; (d.) Coesite inclusion in garnet from Mn–quartzite; (e.) Phengite, epidote and calcite from a garnet calcschist; (f.) Poikilitic garnet porphyroclast with quartz inclusions in garnet calcschist.

180x202mm (300 x 300 DPI)

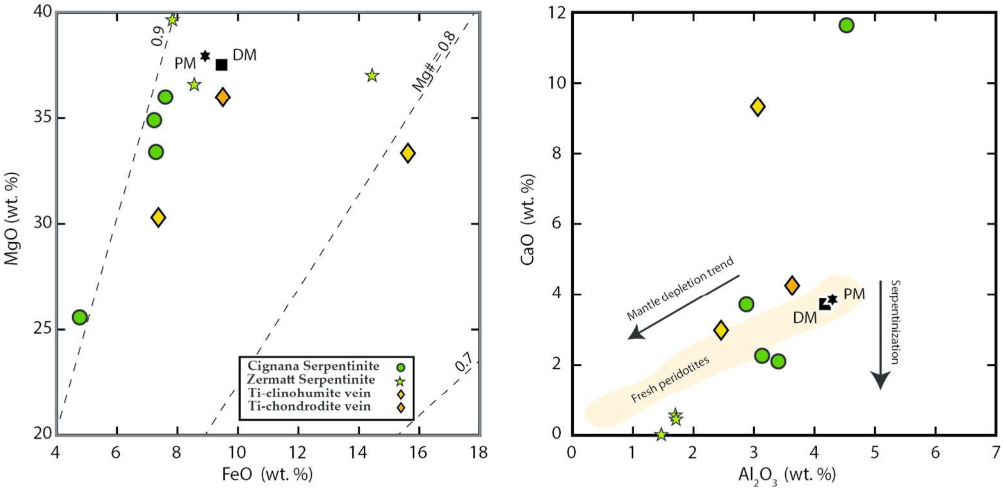

Figure 6 - Major element plots (FeO vs MgO and Al_2O_3 vs CaO) for the Zermatt serpentinites and for the Cignana serpentinites and veins. FeO vs MgO: contours are Mg# = Mg/(Mg+Fe). Al_2O_3 vs CaO: the shaded areas refer to the mantle depletion trend in peridotite.

170x83mm (300 x 300 DPI)

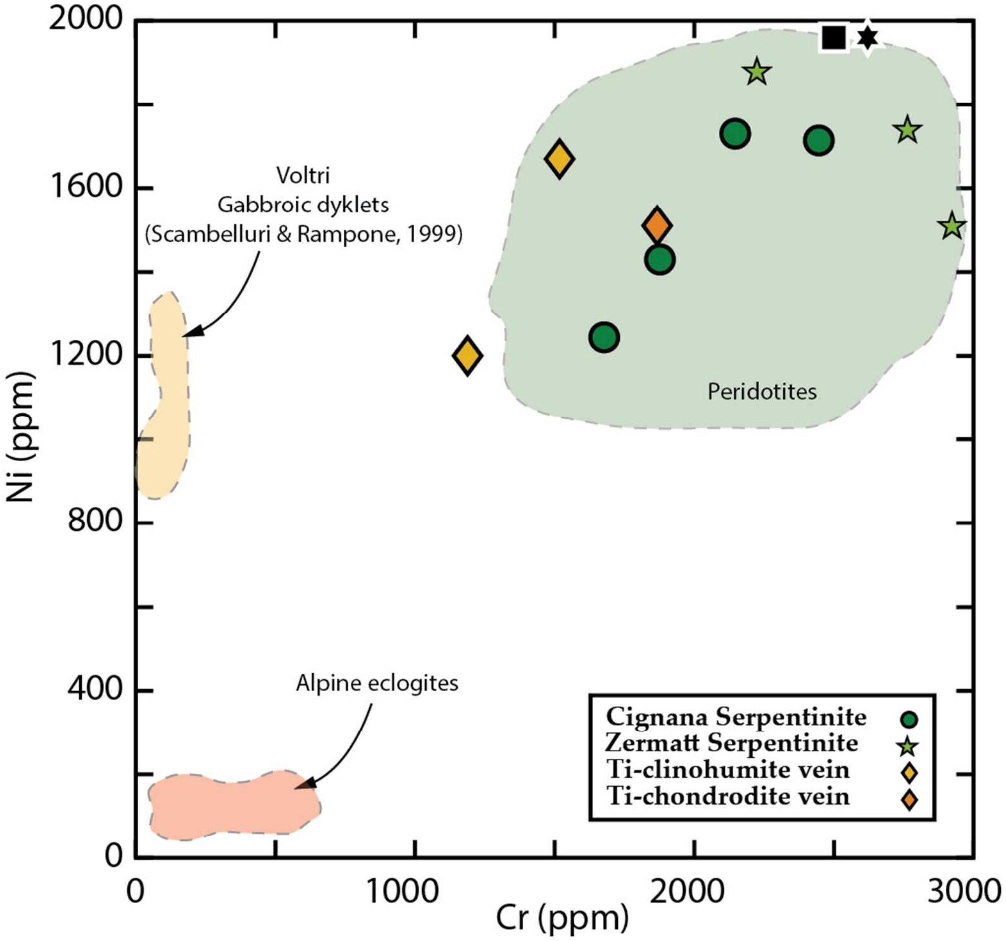

Figure 7 - Cr vs Ni plot for the Zermatt serpentinites and for the Cignana serpentinites and veins. Shaded areas are for Alpine eclogites (Cignana, this work; Monviso, Angiboust et al., 2012), gabbroic dykelets (Voltri, Scambelluri & Rampone, 1999) and peridotites (Lanzo, Müntener et al., 2004; Guarnieri et al., 2012). Note that the Ti–chondrodite (orange diamond) and the Ti–clinohumite veins (yellow diamonds) fall within the peridotite area.

86x81mm (300 x 300 DPI)

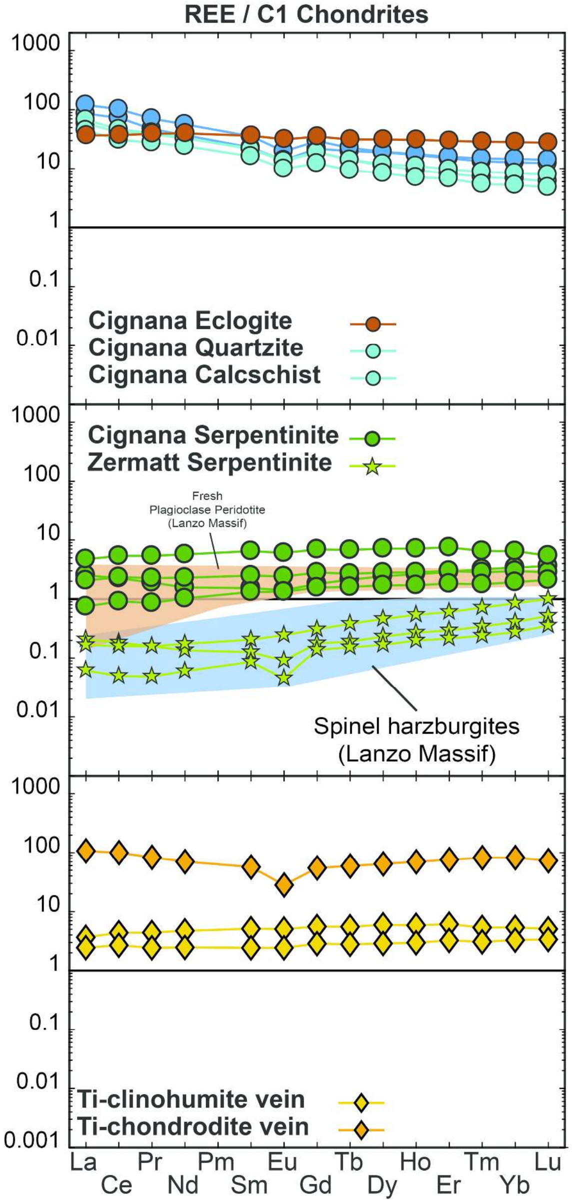

Figure 8 - C1 Chondrite–normalized (McDonough and Sun, 1995) REE patterns of bulk–rock from: eclogite and metasediments from the UHP Lago di Cignana Unit, Cignana and Zermatt serpentinites and Cignana Ti–bearing veins. Shaded areas are for fresh plagioclase peridotite (orange) and spinel harzburgites (blue) from the Lanzo Massif (Guarneri et al, 2012).

184x392mm (300 x 300 DPI)

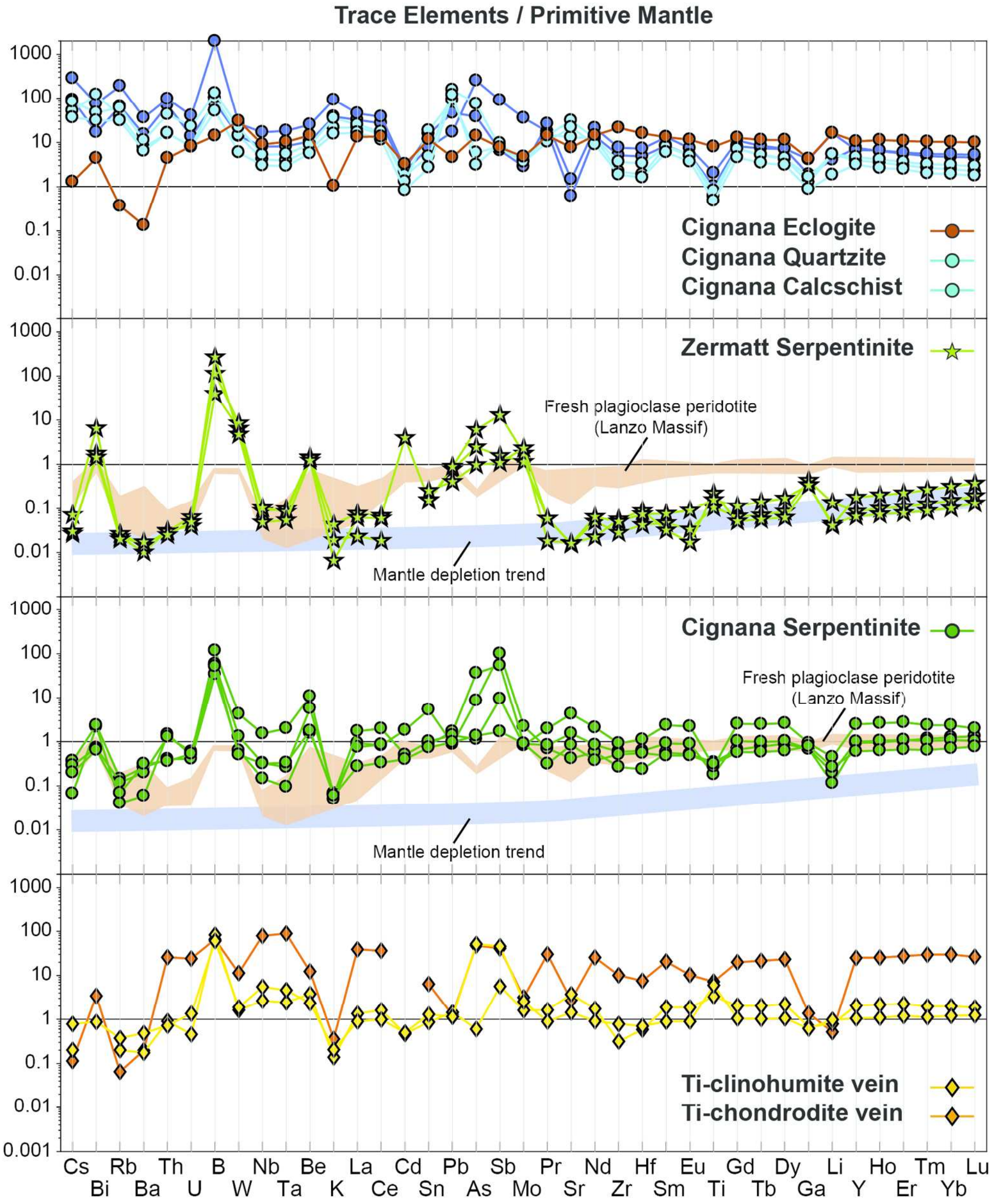

Figure 9 - PM–normalized (McDonough and Sun, 1995; B and Li after Marschall et al., 2017) TE patterns of bulk–rock from: eclogite and metasediments from the UHP Lago di Cignana Unit, Cignana and Zermatt serpentinites and Cignana Ti–bearing veins. Shaded areas are for fresh plagioclase peridotite from the Lanzo Massif (orange; Guarneri et al, 2012) and the mantle depletion trend (blue).

159x194mm (300 x 300 DPI)

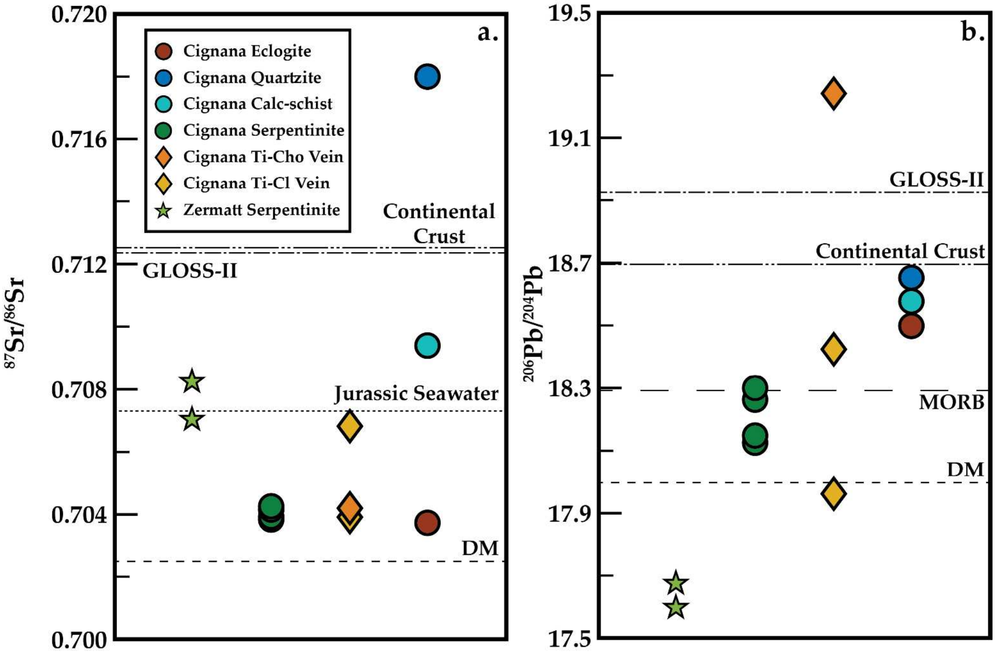

Figure 10 - ^{206}Pb/^{204}Pb and ^{87}Sr/^{86}Sr values of analysed samples from the Lago di Cignana Unit, Cignana serpentinites and veins and Zermatt serpentinites. Values from GLOSS–II (Plank, 2014), depleted mantle (Rehka & Hofmann, 1997), Jurassic seawater (Jones & Jenkyns, 2001) and average continental crust (Rudnick and Gao, 2003) are reported for comparison.

255x167mm (300 x 300 DPI)

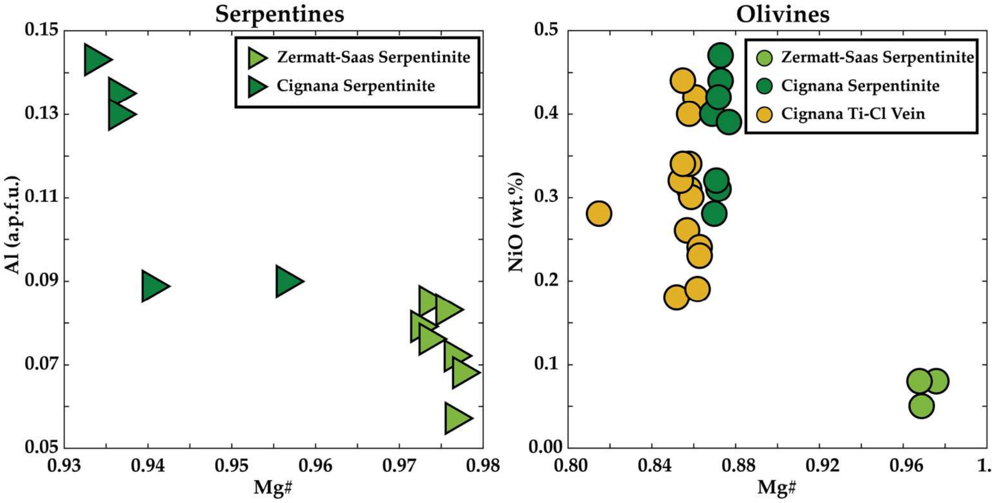

Figure 11 - Mineral analyses of serpentine and olivine from the Zermatt serpentinite, the Cignana serpentinite and the Ti–bearing veins. Serpentine from Zermatt has higher Mg# and lower Al content that serpentine from Cignana. Mg# in Zermatt olivine is comparable with serpentine from the same locality. Olivine from the Cignana serpentinite and Ti–clinohumite vein have similar Mg#, lower than in the Zermatt serpentinite.

162x81mm (300 x 300 DPI)

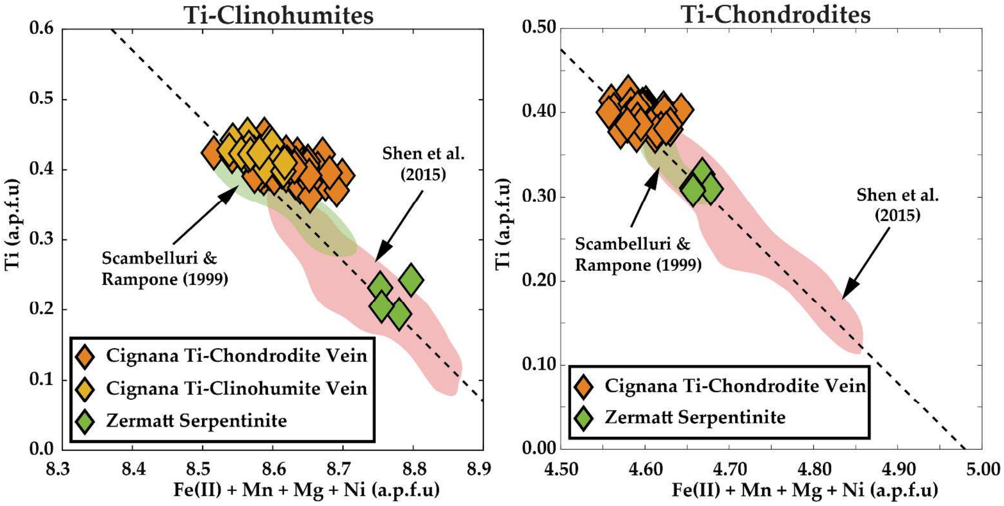

Figure 12 - Mineral analyses of Ti–chondrodite and Ti–clinohumite from the Cignana serpentinite veins and from the Zermatt serpentinite. Note the lower Ti content of both Ti–chondrodite and Ti–clinohumite from the Zermatt–serpentinite respect to Cignana serpentinite veins. Mineral analyses from Scambelluri & Rampone (1999) and Shen et al., (2014) reported for comparison.

323x161mm (300 x 300 DPI)

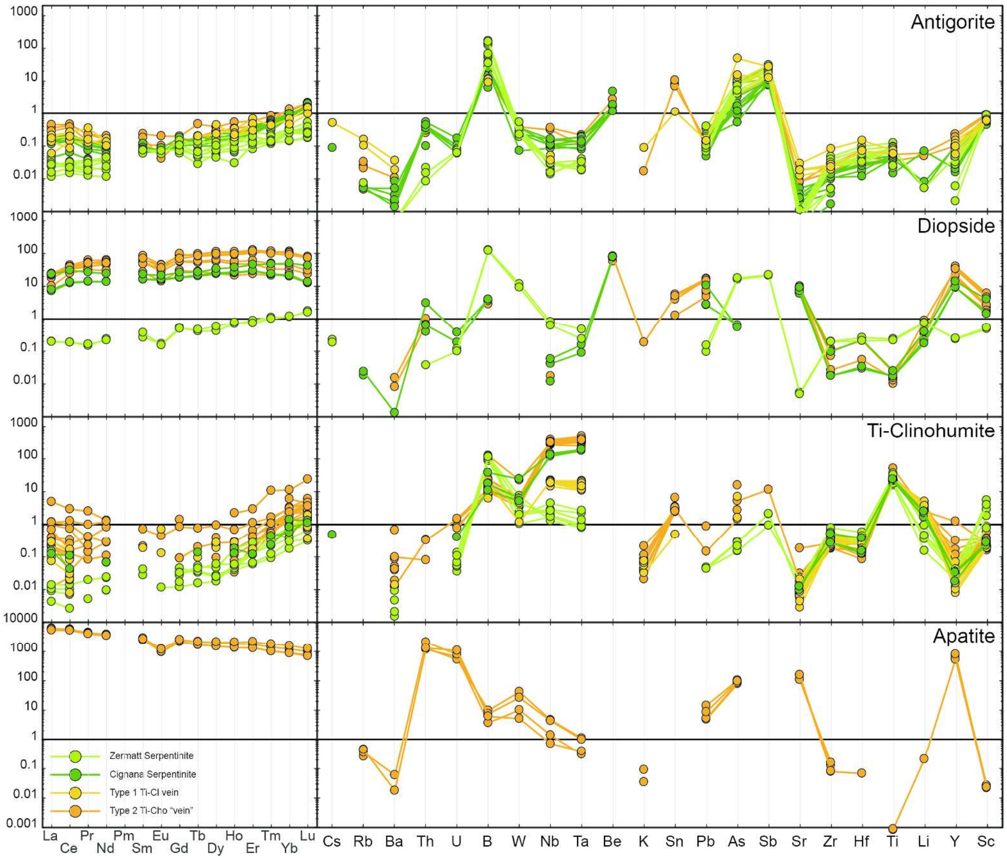

Figure 13 - REE and TE composition of antigorite, diopside, Ti–clinohumite and Apatite from the Cignana and Zermatt serpentinites.

211x180mm (300 x 300 DPI)

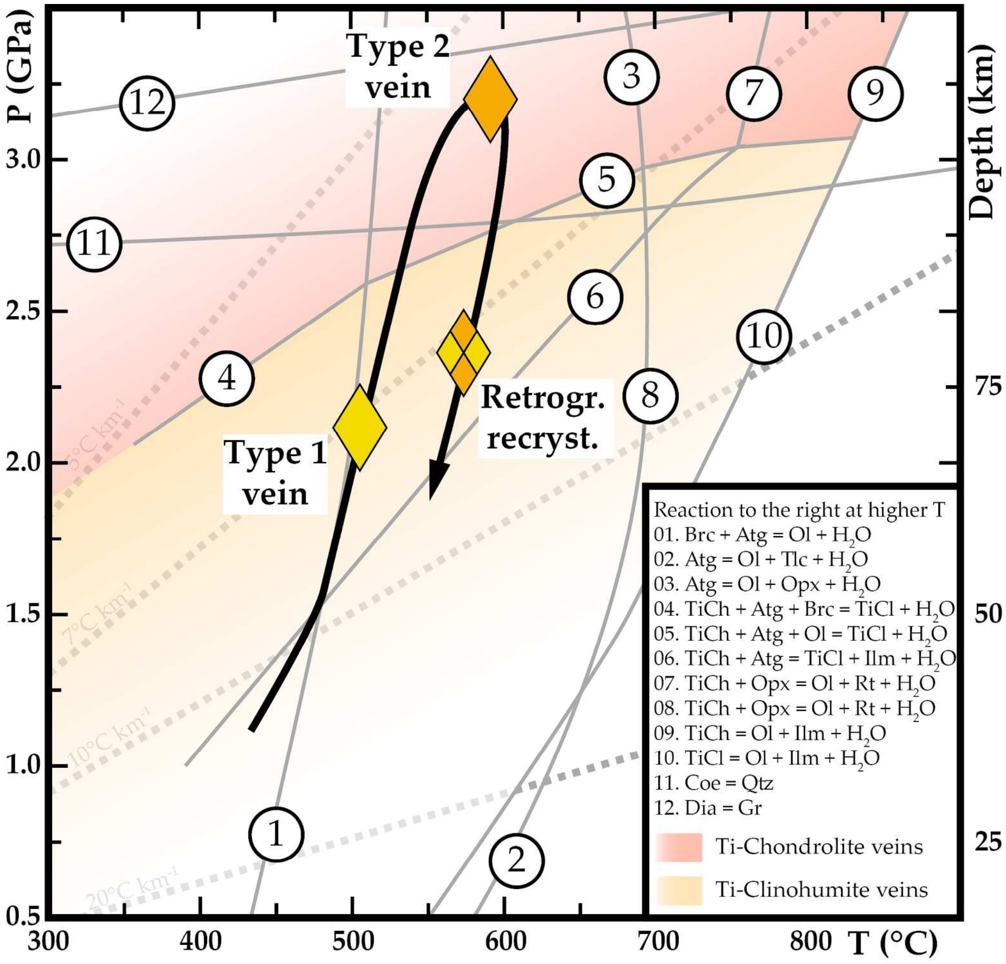

Figure 14 - Pressure–Temperature diagram with the stability field of Ti–clinohumite (light orange) and Ti–chondrodite (dark orange) in serpentinite systems. The main reaction lines involving Ti–clinohumite and Ti–chondrodite and the quartz to coesite transition lines are from Shen et al. (2015). The black arrow corresponds to the PT path of the Lago di Cignana Unit (Groppo et al., 2009). The dashed grey lines are the geothermal gradients for cold (5–7 °C/km) and hot (20 °C/km) subduction. Cignana type 1 veins formed during the prograde path, after the partial dehydration of the Cignana serpentinite. Type 2 veins formed at peak UHP conditions, in the stability field of Ti–chondrodite. Type 1 and 2 veins recrystallized during the retrograde decompression in the stability field of Ti–clinohumite.

187x179mm (300 x 300 DPI)

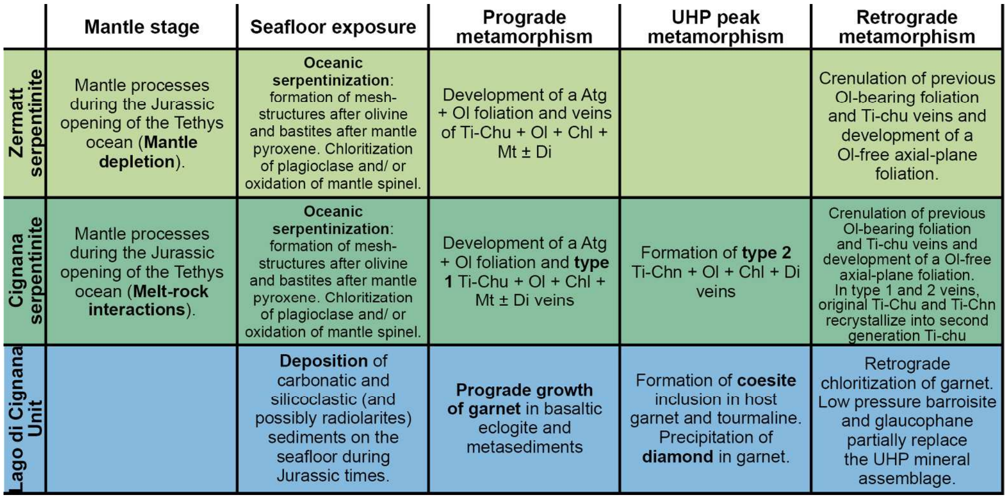

	Mantle stage	Seafloor exposure	Prograde metamorphism	UHP peak metamorphism	Retrograde metamorphism
Zermatt serpentinite	Mantle processes during the Jurassic opening of the Tethys ocean (**Mantle depletion**).	**Oceanic serpentinization**: formation of mesh-structures after olivine and bastites after mantle pyroxene. Chloritization of plagioclase and/ or oxidation of mantle spinel.	Development of a Atg + Ol foliation and veins of Ti-Chu + Ol + Chl + Mt ± Di		Crenulation of previous Ol-bearing foliation and Ti-chu veins and development of a Ol-free axial-plane foliation.
Cignana serpentinite	Mantle processes during the Jurassic opening of the Tethys ocean (**Melt-rock interactions**).	**Oceanic serpentinization**: formation of mesh-structures after olivine and bastites after mantle pyroxene. Chloritization of plagioclase and/ or oxidation of mantle spinel.	Development of a Atg + Ol foliation and **type 1** Ti-Chu + Ol + Chl + Mt ± Di veins	Formation of **type 2** Ti-Chn + Ol + Chl + Di veins	Crenulation of previous Ol-bearing foliation and Ti-chu veins and development of a Ol-free axial-plane foliation. In type 1 and 2 veins, original Ti-Chu and Ti-Chn recrystallize into second generation Ti-chu
Lago di Cignana Unit		**Deposition** of carbonatic and silicoclastic (and possibly radiolarites) sediments on the seafloor during Jurassic times.	**Prograde growth of garnet** in basaltic eclogite and metasediments	Formation of **coesite** inclusion in host garnet and tourmaline. Precipitation of **diamond** in garnet.	Retrograde chloritization of garnet. Low pressure barroisite and glaucophane partially replace the UHP mineral assemblage.

Figure 15 - Petrogenetic sequence summarizing and comparing the overall evolution of the Zermatt and Cignana serpentinite and the Lago di Cignana Unit.

184x90mm (300 x 300 DPI)

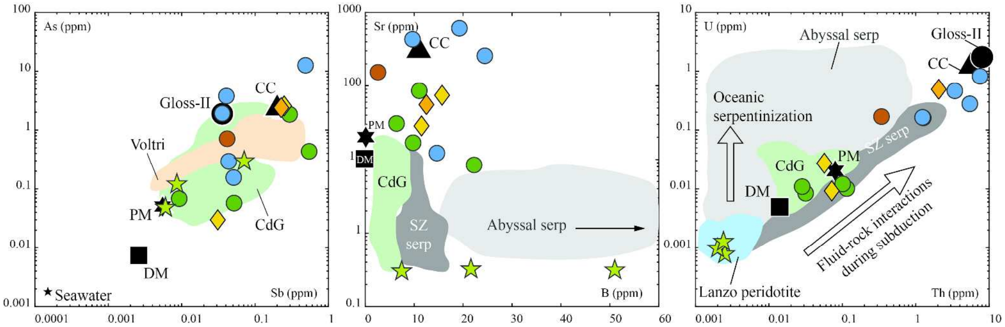

Figure 16 - As vs Sb, Sr vs B and U vs Th plots of analysed samples from the Lago di Cignana Unit, Cignana serpentinites and veins and Zermatt serpentinites. Shaded area from Voltri (Cannaò et al., 2016), Cima di Gagnone (CdG; Scambelluri et al., 2014; Cannaò et al., 2015), Subduction zone (SZ serp) and abyssal serpentinites (Deschamps et al., 2013 and references therein) and Lanzo peridotite (Guarnieri et al., 2012).

340x110mm (300 x 300 DPI)

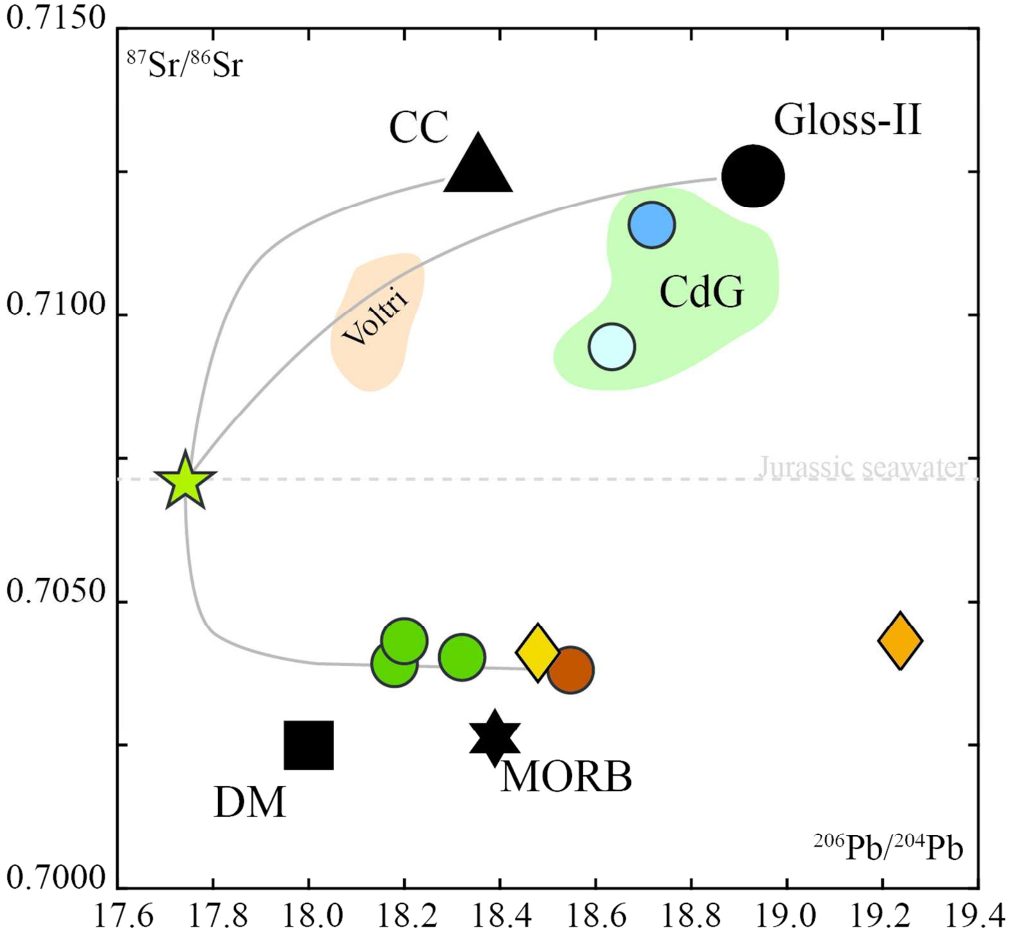

Figure 17 - ^{206}Pb/^{204}Pb vs ^{87}Sr/^{86}Sr, shows a mixing line between Zermatt serpentinite and a fluid of composition comparable with Cignana eclogite (Sample LCG1401), Continental Crust (Rudnick and Gao, 2003) and GLOSS–II (Plank, 2014). Shaded area from Voltri (Cannaò et al., 2016), Cima di Gagnone (CdG; Scambelluri et al., 2014; Cannaò et al., 2015). Values from GLOSS–II (Plank, 2014), depleted mantle (Rehka & Hofmann, 1997), Jurassic seawater (Jones & Jenkyns, 2001) and average continental crust (Rudnick and Gao, 2003) are reported for comparison.

116x109mm (300 x 300 DPI)

Table 1 - Lists of collected samples and mineral assemblages of the Lago di Cignana Unit and of the Cignana and Zermatt serpentinite.

	Sample Name	**Rock Type**	**Mineral assemblage**	**GPS coordinates**	
				N	**E**
LCU	LCG1401	Eclogite	Omp, Grt, Rt	5081691	390860
	LCG1414	Quartzite	Qz, Grt, Ph, Ep	5081468	390669
	LCG1415A	Quartzite	Qz, Tur, Grt, Ph, Ep	5081468	390669
	LCG1416A	Calcshists	Cal, Qz, Grt, Ph, Ep	5081405	390653
	LCG1416B	Calcshists	Cal, Qz, Grt, Ph, Ep	5081405	390653
	LCG1501	Impure marble	Cal, Qz, Grt, Ph, Ep	5081405	390653
Cignana serp.	ZSG1402	Ti-chondrodite vein	Ti-Chn, Ti-Chu, Ap, Ol, Chl, Di, Ilm, REE-phases	5080411	390635
	ZSG1502 V	Ti-clinohumite vein	Ti-Chu, Ol, Chl, Di, Ilm, Mag, Atg	5079863	390554
	ZSG1507 V	Ti-clinohumite vein	Ti-Chu, Ol, Chl, Di, Ilm, Mag, Atg	5079808	390474
	ZSG1403	Serpentinite	Atg, Ol, Di, Chl, Mag	5080411	390635
	ZSG1502 S	Serpentinite	Atg, Ol, Di, Chl, Mag	5079863	390554
	ZSG1507 S	Serpentinite	Atg, Ol, Di, Chl, Mag	5079808	390474
	ZSG1510	Serpentinite	Atg, Ol, Di, Chl, Mag	5079908	390620
ZSZ	ZSG1405	Serpentinite	Atg, Ol, Di, Chl, Mag	5070553	395494
	ZSG1406	Serpentinite	Atg, Ol, Di, Chl, Mag	5070553	395494
	ZSG1410	Serpentinite	Atg, Ol, Di, Chl, Mag	5081326	392588

Table 2 - Major (wt.%) and Trace element (µg/g) composition of eclogite and metasediments from the Lago di Cignana Unit, Cignana serpentinites and Ti–bearing veins and of Zermatt serpentinite. Samples were analysed for major elements (d.l. = 0.01 wt.%) and V (d.l. 5 µg/g), Be, Sr, Zr (d.l. 2 µg/g), Sc, Y, and Ba (d.l. 1 µg/g) by means of Fusion-ICP-MS at Act-Lab, Canada. Trace elements were analysed by liquid ICP-MS at Geosciences Montpellier (France). Detection limits can be found in Godard et al. (2000). Furthermore, all samples were analysed for major and trace element by PPP-LA-ICP-MS at the University of Bern.

	Lago di Cignana Unit															
	Eclogite			**Quartzite**						**Calcschist**						
	LCG1401			**LCG 1414B**			**LCG 1415A**			**LCG 1416A**			**LCG 1416B**			**LCG 1501**
	FUS	**ICP**	**PPP**	**FUS**	**ICP**	**PPP**	**FUS**	**ICP**	**PPP**	**FUS**	**ICP**	**PPP**	**FUS**	**ICP**	**PPP**	**PPP**
SiO_2	46.89		49.18	78.28		79.36	71.24		72.43	33.96		37.46	49.45		51.11	29.69
TiO_2	2.49		2.37	0.219		0.23	0.454		0.44	0.131		0.14	0.182		0.19	0.1
Al_2O_3	15.77		14.55	7.44		6.96	11.73		10.96	3.38		3.12	4.77		4.36	2.59
Fe_2O_3(T)	10.65		10.55	4.15		3.99	5.18		4.96	1.79		1.85	2.12		2.14	1.6
MnO	0.173		0.17	3.679		3.37	0.234		0.24	0.371		0.38	0.424		0.44	0.39
MgO	6.07		5.83	1.17		1.14	1.8		1.72	0.81		0.95	0.8		0.82	0.94
CaO	12.38		12.09	1.78		1.68	2.45		2.45	33.87		30.5	22.32		21.17	30.46
Na_2O	4.75		4.53	0.23		0.27	0.65		0.65	0.19		0.18	0.23		0.21	0.09
K_2O	0.03		0.0356	1.09		1.03	2.63		2.53	0.61		0.54	1.01		0.91	0.46
P_2O_5	0.73		0.69	0.06		0.0526	0.11		0.1	0.06		0.0541	0.11		0.0887	0.0324
LOI	0.4		0.4	0.4		0.4	3.09		3.09	25.54		25.54	19.08		19.08	33.65
Total	100.3		100.4	99.23		98.48	99.57		99.57	100.7		100.71	100.5		100.52	100
Li		22.5	24.3		5.61	5.49		22.1	20.2		7.42	6.65		7.35	6.61	2.56
Be	1		0.983	< 1		0.709	2		1.7	< 1		0.462	< 1		0.598	0.382
B			2.68			14.7			365			19.3			24.5	9.69
Sc	33	30.2	28.5	10	8.85	9.99	14	12.6	12.6	5	4.79	5.02	6	5.92	6.5	4.29
Ti		9570	14200		1220	1380		2440	2640		734	839		969	1140	583
V	263	246	269	38	34.7	37.3	89	86.2	86	29	26.7	26.5	35	31.4	32.1	23
Cr			121			41.2			68.7			36.7			32.7	32.4
Mn		1190	1320		26800	26100		1710	1860		2840	2940		3200	3410	3000
Co		27.1	30.5		40.3	38.3		32.7	32.5		15.7	16.6		19.7	20.7	13.2
Ni		85.4	114		48	49.1		84.7	82.1		36.5	47.4		46.1	51.1	37
Cu		14.3			4.67			52.3			369			17.4		87.3
Zn		65.3	49.8		51.5	34.6		101	57.2		27.1	20.7		40.7	24.6	21.1
Ga		17			7.53			16.4			5			6.6		3.53
Ge																1.1
As		0.704	0.229		12.5	12.8		1.89	1.38		3.73	4.13		-	0.291	0.154
Se																0.295
Rb		0.218	0.375		39.1	40.5		113	112		23.4	25.1		36.2	37.9	18.5
Sr	162	152	178	14	12.1	13.7	32	29	30.8	634	605	668	265	255	292	428
Y	42	45	38	32	31.8	28	31	28.7	25.1	20	16.7	16.6	22	19.9	19.6	13.5
Zr	256	10.9	224	61	5.24	53.1	101	3.23	79.3	27	0.671	23.1	39	0.78	37.9	19.5
Nb		5.93	8.26		5.2	5.11		11	10.3		2.71	3.14		3.44	3.94	1.96
Mo			0.237			1.76			0.142			0.182			0.201	0.18
Cd			0.129			0.088			0.103			0.0717			0.052	0.0325
In																0.0116
Sn		1.52			0.987			2			0.623			2.39		0.345
Sb		0.0415	0.0475		0.491	0.441		0.0364	0.037		0.0408	0.0646		0.0436	0.0719	0.0515
Cs		0.0265	0.032		1.91	1.93		5.92	5.86		1.07	1.14		1.73	1.79	0.761
Ba	< 2	0.874	1.41	110	98.7	109	261	237	254	57	50.7	62.4	81	72.5	88.8	42.3
La		8.58	8.28		20.5	18.4		28.8	27.5		13.9	13.4		16.1	16.4	10.7
La		8.58	8.28		20.5	18.4		28.8	27.5		13.9	13.4		16.1	16.4	10.7
Pr		3.6	3.99		4.42	4.4		6.63	7.06		3.58	3.86		3.77	4.27	2.59
Nd		18	19.3		17.1	17.1		26	27.5		15	16.3		15.3	17.4	11.1
Sm		5.26	5.32		3.37	3.46		5.28	5.6		3.31	3.62		3.23	3.69	2.41
Eu		1.76	1.98		0.794	0.812		1.12	1.21		0.79	0.866		0.76	0.888	0.558
Gd		6.89	5.67		4.35	3.45		5.88	4.7		3.86	3.4		3.81	3.38	2.46
Tb		1.12	0.968		0.724	0.644		0.821	0.761		0.513	0.501		0.512	0.503	0.339
Dy		7.55	6.49		4.74	4.35		4.8	4.44		2.79	2.83		2.96	3.01	2.07
Ho		1.67	1.32		0.935	0.837		0.966	0.868		0.52	0.5		0.606	0.573	0.394
Er		4.71	4.14		2.42	2.32		2.57	2.43		1.32	1.41		1.57	1.71	1.09
Tm		0.697	0.58		0.331	0.3		0.366	0.338		0.18	0.184		0.218	0.217	0.135
Yb		4.51	3.95		2.07	1.96		2.37	2.24		1.09	1.17		1.36	1.4	0.853
Lu		0.669	0.574		0.306	0.286		0.345	0.321		0.15	0.158		0.195	0.203	0.119
Hf		0.315	4.45		0.269	1.36		0.108	2.02		0.0279	0.533		0.0295	0.936	0.445
Ta		0.378	0.452		0.301	0.319		0.669	0.689		0.141	0.186		0.201	0.242	0.108
W		0.883	0.332		-	0.398		-	0.763		-	0.412		-	0.632	0.171
Tl																0.111
Pb		0.69	0.785		2.56	2.35		6.89	6.7		23.1	23.6		13.6	12.8	17.6
Bi			0.0106			0.042			0.187			0.298			0.117	0.0774
Th		0.345	0.32		5.51	5.22		7.6	7.73		1.25	1.36		3.44	3.69	1.28
U		0.167	0.284		0.275	0.326		0.812	1.16		0.162	0.233		0.458	0.545	0.159

Table 2 – (continued 1)

	Cignana Serpentinite										
	Serpentinite						**Ti-chondrodite vein**			**Ti-Clinohumite Vein**	
	ZSG 1403			**ZSG 1502S**	**ZSG 1507S**	**ZSG 1510**	**ZSG 1402**			**ZSG 1502V**	**ZSG 1507V**
	FUS	**ICP**	**PPP**	**PPP**	**PPP**	**PPP**	**FUS**	**ICP**	**PPP**	**PPP**	**PPP**
SiO_2	38.94		40.48	40.34	40.98	39.97	35.77		37.91	37.12	42.05
TiO_2	0.064		0.065	0.04	0.06	0.06	1.537		1.54	1.2	0.66
Al_2O_3	3.13		2.79	2.89	4.55	3.43	3.65		3.33	2.45	3.06
Fe_2O_3(T)	7.6		7.59	7.34	4.8	7.29	9.5		9.06	15.63	7.41
MnO	0.098		0.0999	0.08	0.07	0.09	0.176		0.17	0.23	0.17
MgO	36		34.84	33.65	25.7	35.19	35.98		34.37	33.38	30.33
CaO	2.26		2.23	3.74	11.71	2.14	4.26		4.54	3	9.34
Na_2O	0.01		0.0186	0.05	0.1	0.06	0.02		0.0263	0.05	0.09
K_2O	< 0.01		0.0015	0.002	0.0019	0.0017	< 0.01		0.0104	0.0058	0.0039
P_2O_5	< 0.01		0.0023	0.0006	0.0006	0.0017	1		0.94	0.0041	0.0009
LOI	10.42		10.42	11.87	12.03	11.77	8.03		8.03	6.93	6.89
Total	98.53		98.54	100	100	100	99.92		99.93	100	100
Li		0.16	0.255	0.28	0.619	0.369		0.721	0.787	1.35	1.09
Be	< 1		0.727	0.107	0.391	0.12	1		0.842	0.159	0.256
B			22.3	6.45	11.1	9.83			12.5	11.5	15.7
Sc	12	12.9	11.3	16.9	19.7	14.7	13	13.7	12.3	13.2	17.4
Ti		414	390	220	331	380		8690	9230	7190	3960
V	57	64.5	59	66.2	47	70.8	73	77.7	69.4	104	42.1
Cr			2450	1880	1680	2150			1870	1520	1190
Mn		771	774	644	568	683		1360	1320	1780	1320
Co		79.7	89.4	77.4	65	88.3		91.6	103	119	86.5
Ni		1710	2060	1430	1240	1730		1510	1710	1670	1200
Cu		19.8		14.7	9.77	27.1		8.7		59.8	9.77
Zn		40.9	18.1	20.1	13.8	23.9		55.8	45.1	50.7	31.8
Ga		2.73		2.74	3.68	3.15		5.5		2.46	2.7
Ge				0.765	1.02	0.717				0.743	1.05
As		0.43	0.882	1.82	0.0568	0.0676		2.39	3.12	2.56	0.0299
Se				0.138							
Rb		0.0236	0.0333	0.0863	0.0717	0.0406		0.0385	0.107	0.223	0.12
Sr	10	8.33	8.9	30.5	84.9	16.7	62	55.4	60	28.5	74.4
Y	5	4	3.74	4.3	10.6	2.6	103	108	98	4.5	8.8
Zr	4	2.81	2.33	6.24	9.58	5.4	118	106	111	8.15	3.32
Nb		0.999	0.913	0.0961	0.216	0.21		52.2	55.2	3.6	1.74
Mo			0.111	0.0448	0.0412	0.0448			0.159	0.127	0.0796
Cd			0.0729		0.0201	0.016			<0.0582	0.0198	0.0186
In				0.0113	0.008	0.0126				0.0085	0.0068
Sn		0.69		0.11	0.131	0.0959		0.833		0.168	0.112
Sb		0.55	0.448	0.298	0.0521	0.0093		0.227	0.261	0.25	0.031
Cs		0.0014	0.0028	0.0077	0.0061	0.0042		0.0024	0.0058	0.0164	0.0042
Ba	< 2	0.388	1.01	1.73	1.31	2.07	2	1.3	1.65	3.17	1.15
La		0.598	0.561	0.494	1.12	0.178		25.3	25.4	0.577	0.868
La		0.598	0.561	0.494	1.12	0.178		25.3	25.4	0.577	0.868
Pr		0.177	0.186	0.211	0.5	0.08		7.74	8.22	0.226	0.414
Nd		0.717	0.722	1.05	2.61	0.472		31.8	34.3	1.13	2.16
Sm		0.227	0.217	0.369	0.957	0.196		8.42	8.84	0.361	0.762
Eu		0.08	0.0808	0.136	0.338	0.0751		1.58	1.65	0.137	0.285
Gd		0.356	0.33	0.557	1.38	0.312		10.9	10.1	0.574	1.11
Tb		0.0771	0.0694	0.0966	0.245	0.0579		2.13	1.97	0.101	0.2
Dy		0.604	0.53	0.69	1.76	0.416		15.8	14.1	0.706	1.47
Ho		0.144	0.125	0.155	0.386	0.0935		3.76	3.23	0.162	0.321
Er		0.464	0.445	0.484	1.2	0.292		12.1	11.2	0.517	0.98
Tm		0.0787	0.0731	0.0695	0.161	0.0438		2.02	1.77	0.0759	0.133
Yb		0.554	0.532	0.479	1.04	0.312		13.2	12	0.527	0.868
Lu		0.0888	0.0835	0.0695	0.134	0.0517		1.79	1.57	0.083	0.125
Hf		0.0667	0.0543	0.176	0.315	0.156		2.14	2.13	0.198	0.165
Ta		0.0737	0.0716	0.0035	0.0098	0.0123		3.33	3.5	0.17	0.0902
W		0.123	0.117	0.0182	0.038	0.0147		0.325	0.276	0.0537	0.047
Tl				0.0013	0.0015	0.0013				0.0036	0.0015
Pb		0.132	0.229	0.253	0.209	0.146		0.189	0.282	0.171	0.215
Bi			0.0054	0.0059	0.0018	0.0016			0.0086	0.0022	
Th		0.116	0.105	0.0319	0.102	0.0286		2.06	1.91	0.0569	0.0718
U		0.0101	0.0115	0.0083	0.012	0.0108		0.491	0.442	0.0273	0.0092

Table 2 – (continued 2)

	Zermatt Serpentinite								
	Serpentinite								
	ZSG 1405			**ZSG 1406**			**ZSG 1410**		
	FUS	**ICP**	**PPP**	**FUS**	**ICP**	**PPP**	**FUS**	**ICP**	**PPP**
SiO_2	39.07		40.05	36.44		38.11	39.24		40.98
TiO_2	0.02		0.0189	0.043		0.0447	0.032		0.0317
Al_2O_3	1.71		1.44	1.46		1.26	1.7		1.5
Fe_2O_3(T)	8.57		8.67	14.45		14.44	7.83		7.73
MnO	0.107		0.11	0.142		0.15	0.13		0.13
MgO	36.61		35.87	37.08		35.68	39.66		38.11
CaO	0.48		0.42	0.02		<0.00980	0.57		0.49
Na_2O	< 0.01		0.0064	< 0.01		0.006	< 0.01		0.0062
K_2O	< 0.01		0.0013	< 0.01		0.0006	< 0.01		<0.00019
P_2O_5	0.01		0.0015	< 0.01		0.0008	< 0.01		0.0018
LOI	11.98		11.98	10.62		10.62	10.56		10.56
Total	98.57		98.57	100.3		100.31	99.72		99.54
Li		0.188	0.201		0.0626	0.0776		0.0566	0.115
Be	< 1		<0.0986	< 1		<0.0960	< 1		<0.0831
B			7.45			21.6			51
Sc	11	12.6	10.7	10	10.9	9.9	12	12.2	11.3
Ti		126	113		268	268		190	190
V	58	63.8	59.3	45	46.8	45.5	51	54.7	53.9
Cr			2930			2770			2230
Mn		844	852		1080	1160		968	1010
Co		74.6	83.8		95.3	111		95.6	114
Ni		1510	1770		1740	2020		1880	2470
Cu		30.9			9.01			17.8	
Zn		44.3	26.7		51.3	46.5		39.3	17.9
Ga		1.73			1.35			1.37	
Ge									
As		-	0.123		0.303	0.446		-	0.0493
Se									
Rb		0.0135	0.0279		0.0157	0.0168		0.0121	0.0164
Sr	< 2	0.308	0.304	< 2	0.328	0.317	< 2	0.318	0.344
Y	3	0.372	0.313	< 1	0.286	0.298	2	0.765	0.71
Zr	2	0.296	0.241	3	0.601	0.641	3	0.525	0.495
Nb		0.0578	0.0544		0.0678	0.0711		0.0315	0.0301
Mo			0.0566			0.0882			0.116
Cd			0.158			<0.0522			<0.0599
In									
Sn		0.0205			0.0196			0.033	
Sb		0.0086	0.0207		0.0706	0.0726		0.006	<0.0151
Cs		0.0015	0.0037		0.0006	0.0025		0.0006	<0.00312
Ba	< 2	0.0672	2.11	< 2	0.0964	0.46	< 2	0.114	1.78
La		0.0502	0.0428		0.0154	0.0182		0.0397	0.0355
La		0.0502	0.0428		0.0154	0.0182		0.0397	0.0355
Pr		0.0148	0.0135		0.0046	0.006		0.0154	0.0153
Nd		0.0627	0.0605		0.0281	0.0339		0.0813	0.0809
Sm		0.0192	0.0175		0.0131	0.0205		0.0313	0.0293
Eu		0.0052	0.005		0.0026	<0.00349		0.014	0.0142
Gd		0.0357	0.0294		0.028	0.0264		0.0624	0.0581
Tb		0.007	0.0062		0.0056	0.0059		0.0139	0.0132
Dy		0.0579	0.0448		0.0423	0.0414		0.115	0.0969
Ho		0.0149	0.0123		0.0106	0.0107		0.0295	0.0242
Er		0.048	0.0467		0.0348	0.0374		0.0978	0.0957
Tm		0.0086	0.0074		0.006	0.0056		0.0176	0.0155
Yb		0.0672	0.055		0.0451	0.0377		0.139	0.117
Lu		0.0128	0.0109		0.0088	0.0095		0.0245	0.0217
Hf		0.0123	0.0079		0.0245	0.0225		0.021	0.0198
Ta		0.0036	0.0021		0.0031	0.0031		0.002	0.0012
W		0.186	0.126		0.246	0.248		0.137	0.14
Tl									
Pb		0.117	0.182		0.134	0.208		0.0614	0.0989
Bi			0.0163			0.0044			0.0036
Th		0.0025	0.0025		0.0024	0.0022		0.002	<0.0027
U		0.0008	0.0014		0.0013	0.002		0.001	0.0019

Table 3 - Pb and Sr isotopic composition of selected samples from the Lago di Cignana Unit, the Cignana serpentinite and the Zermatt–Saas Zone serpentinite. All values are reported as observed (obs.) and as corrected (corr.) for an age of 40 Ma.

		Pb						**Sr**	
		206/204	**2σ mean**	**207/204**	**2σ mean**	**208/204**	**2σ mean**	**87/86**	**2σ mean**
Eclogite	**LCG1401**	18.547	0.003	15.518	0.002	37.986	0.006	0.703764	0.000006
Tur-Quartzite	**LCG1415A**	18.706	0.001	15.652	0.001	38.881	0.001	0.711573	0.000006
Calc-schist	**LCG1416A**	18.636	0.001	15.648	0.001	38.719	0.002	0.709368	0.000005
Cignana Serpentinite	**ZSG1403**	18.341	0.036	15.596	0.03	38.129	0.074	0.704671	0.000007
	ZSG1502S	18.191	0.025	15.453	0.021	37.737	0.05	0.704160	0.000008
	ZSG1507S	18.172	0.044	15.402	0.036	37.692	0.086	0.703883	0.000004
	ZSG1510	18.32	0.014	15.542	0.013	37.958	0.031	0.703937	0.000011
Ti-Cho vein	**ZSG1402**	19.239	0.024	15.566	0.02	39.287	0.051	0.704221	0.000004
Ti-Cl vein	**ZSG1502V**	18.477	0.063	15.576	0.054	38.117	0.131	0.704059	0.000015
Ti-Cl vein	**ZSG1507V**	18.016	0.071	15.304	0.065	37.404	0.129	0.706789	0.000060
Zermatt Serpentinite	**ZSG1406**	16.887	0.250	14.841	0.226	35.776	0.558	0.708303	0.000042
	ZSG1410	17.731	0.023	15.548	0.019	37.555	0.046	0.707051	0.000036

Table 4 - Representative electron microprobe analyses of mineral phases from the UHP eclogite of the Lago di Cignana Unit.

	Sample LCG1401													
	Garnet				**Omphacite**				**Epidote**		**Paragonite**		**Rutile**	**Titanite**
	Core		**Rim**											
SiO_2	38.54	38.75	38.44	38.82	56.86	56.93	56.37	56.46	39.06	38.76	48.30	47.38	0.01	31.20
TiO_2	-	0.07	0.16	0.02	0.07	0.13	0.05	0.08	0.49	0.28	0.09	0.05	97.63	37.25
Al_2O_3	21.66	21.40	21.67	21.49	11.24	16.07	11.40	11.14	27.00	27.70	38.61	38.91	0.04	1.31
Cr_2O_3	0.01	-	0.01	0.10	0.04	0.05	0.00	0.02	0.09	-	-	0.02	0.04	0.01
FeO	27.45	28.12	27.50	27.57	5.30	6.22	4.65	5.05	7.81	7.29	0.82	0.39	1.11	0.26
MnO	0.77	1.05	1.24	0.67	0.02	-	-	0.00	0.04	0.25	0.03	-	0.05	0.04
MgO	1.95	2.27	2.46	2.03	7.40	3.63	7.64	7.94	0.09	0.14	0.15	0.04	-	-
NiO	-	-	-	-	-	-	-	0.05	0.04	-	0.03	0.02	0.02	-
CaO	11.63	10.92	11.21	11.75	11.78	6.26	11.93	12.12	23.05	23.11	0.22	0.29	0.15	28.75
Na_2O	0.03	0.02	0.03	0.03	8.04	11.61	7.95	7.70	0.02	-	7.07	7.50	-	0.02
K_2O	-	-	0.01	0.00	0.01	0.00	0.01	0.01	0.00	0.01	0.27	0.32	0.01	-
Totals	102.04	102.61	102.72	102.48	100.76	100.90	100.01	100.58	97.69	97.54	95.59	94.92	99.06	98.84
Si	2.990	2.993	2.960	2.999	1.997	1.966	1.989	1.986	3.025	3.005	3.067	3.033	0.000	4.007
Ti	-	0.004	0.009	0.001	0.002	0.003	0.001	0.002	0.028	0.016	0.004	0.002	0.983	3.598
Al	1.981	1.948	1.967	1.957	0.465	0.654	0.474	0.462	2.464	2.531	2.890	2.936	0.001	0.198
Cr	0.000	-	0.001	0.006	0.001	0.001	0.000	0.001	0.006	-	-	0.001	0.000	0.001
Fe(III)*	0.077	0.055	0.176	0.073	0.013	0.033	0.012	0.013	0.506	0.473	-	-	0.000	-
Fe(II)	1.704	1.762	1.595	1.708	0.143	0.147	0.125	0.136	-	-	0.044	0.021	0.012	0.028
Mn	0.051	0.069	0.081	0.044	0.001	-	-	0.000	0.003	0.016	0.001	-	0.001	0.004
Mg	0.226	0.261	0.282	0.234	0.387	0.187	0.402	0.416	0.010	0.016	0.015	0.003	-	-
Ni	-	-	-	-	-	-	-	0.002	0.002	-	0.002	0.001	0.000	-
Ca	0.967	0.904	0.925	0.973	0.443	0.232	0.451	0.457	1.913	1.920	0.015	0.020	0.002	3.956
Na	0.005	0.004	0.004	0.004	0.547	0.777	0.544	0.525	0.003	-	0.871	0.931	-	0.005
K	-	-	0.001	0.000	0.001	0.000	0.001	0.000	0.000	0.001	0.022	0.026	0.000	-
H*	-	-	-	-	-	-	-	-	1.000	1.000	2.000	2.000	-	1.000
Totals	8.000	8.000	8.000	8.000	4.000	4.000	4.000	4.000	8.960	8.977	8.930	8.974	1.000	12.798

*Fe(III) and H_2O contents calculated stoichiometrically

Table 5 - Representative electron microprobe analyses of mineral phases from the UHP quartzite of the Lago di Cignana Unit.

	Sample LCG1414								**Sample LCG1415**						
	Epidote		**Phengite**		**Garnet**		**Barroisite**		**Garnet**		**Chlorite**	**Phengite**		**Tourmaline**	
					Core	**Rim**								**Core**	**Rim**
SiO_2	38.08	37.33	51.98	51.96	37.61	37.36	49.51	50.15	37.62	37.12	26.87	53.18	52.87	37.67	37.53
TiO_2	0.11	0.13	0.35	0.33	0.04	0.05	0.15	0.08	0.02	0.03	-	0.14	0.22	-	-
Al_2O_3	25.25	23.24	27.86	27.36	21.48	21.74	7.66	6.45	21.58	21.31	20.17	27.97	28.08	31.06	29.74
Cr_2O_3	0.06	-	0.07	0.02	-	0.06	0.05	0.04	0.00	0.05	-	0.01	0.00	-	-
FeO	11.03	13.24	3.48	3.78	5.66	29.55	17.48	16.53	30.36	26.40	22.91	2.32	2.22	3.60	6.41
MnO	0.31	0.69	0.05	0.09	30.45	4.47	0.61	0.89	1.71	4.46	0.46	-	0.04	-	-
MgO	0.03	0.03	3.02	2.96	2.02	1.86	11.34	12.42	3.46	1.43	16.53	3.06	3.11	9.06	8.04
NiO	0.01	-	0.04	0.09	0.05	-	0.04	0.08	-	-	-	0.04	0.02	-	-
CaO	23.07	22.59	-	0.03	4.68	7.21	7.04	8.11	5.66	9.06	0.06	0.02	0.01	0.28	0.33
Na_2O	-	0.02	0.49	0.44	0.02	0.05	3.49	2.78	0.04	-	0.03	0.42	0.47	2.72	2.81
K_2O	-	0.04	9.83	9.82	-	0.03	0.22	0.25	0.00	0.01	-	9.29	9.47	0.04	-
Totals	97.95	97.31	97.17	96.88	102.01	102.38	97.59	97.78	100.44	99.87	87.03	96.45	96.51	84.43	84.86
Si	2.977	2.964	6.806	6.837	2.962	2.924	7.049	7.138	2.974	2.969	5.615	6.928	6.893	6.162	6.210
Ti	0.007	0.008	0.035	0.033	0.002	0.003	0.016	0.009	0.001	0.002	-	-	-	-	-
Al	2.326	2.175	4.300	4.243	1.994	2.006	1.285	1.082	2.010	2.009	4.979	0.014	0.021	5.988	5.799
Cr	0.004	-	0.007	0.002	-1.650	0.004	0.005	0.004	0.000	0.003	-	4.295	4.315	-	-
Fe(III)*	0.721	0.879	-	-	0.030	0.285	1.583	1.432	0.092	0.083	0.111	-	-	-	-
Fe(II)	-	-	0.381	0.416	0.343	1.650	0.498	0.536	1.915	1.683	3.893	-	-	0.492	0.887
Mn	0.021	0.046	0.005	0.011	2.031	0.296	0.073	0.107	0.114	0.303	0.081	0.253	0.242	-	-
Mg	0.004	0.003	0.589	0.581	0.237	0.217	2.407	2.635	0.407	0.171	5.150	-	0.005	2.209	1.983
Ni	0.001	-	-	-	0.003	-	0.005	0.009	-	-	-	0.594	0.604	-	-
Ca	1.932	1.922	-	0.004	0.395	0.605	1.074	1.237	0.480	0.776	0.014	-	-	0.049	0.058
Na	-	0.003	0.124	0.113	0.003	0.008	0.963	0.767	0.006	-	0.024	0.002	0.002	0.863	0.901
K	-	0.004	1.642	1.648	-	0.003	0.041	0.046	0.000	0.001	-	0.107	0.118	0.008	-
H*	1.000	1.000	4.000	4.000	-	-	2.000	2.000	-	-	16.000	-	-	4.004	4.001
B*	-	-	-	-	-	-	-	-	-	-	-	4.000	4.000	3.001	3.002
Totals	8.993	9.004	17.889	17.888	8.000	8.001	16.999	17.002	8.000	8.000	35.868	16.193	16.200	22.776	22.841

*Fe(III), B and H_2O contents calculated stoichiometrically

Table 6 - Representative electron microprobe analyses of mineral phases from the UHP calcschist of the Lago di Cignana Unit.

	Sample LCG1416A											**Sample LCG1416B**					
	Garnet		**Paragonite**			**Phengite**		**Chlorite**		**Calcite**		**Epidote**		**Phengite**		**Calcite**	
												Core	**Rim**				
SiO_2	37.66	38.14	47.31	47.39	47.70	50.82	50.90	25.99	27.42	0.08	0.01	36.51	38.96	51.39	50.38	0.04	-
Al_2O_3	19.55	20.73	38.59	38.36	38.24	27.51	26.73	20.62	19.91	0.02	0.02	21.62	24.70	26.67	27.25	0.01	0.02
FeO	22.12	18.80	0.31	0.34	0.30	2.34	2.74	29.19	20.86	1.71	1.83	12.00	9.44	2.77	3.13	1.47	1.56
MnO	7.50	13.83	-	0.04	0.01	0.02	0.02	0.43	0.43	0.32	0.39	0.53	0.41	0.02	0.04	0.58	0.53
MgO	1.74	1.38	0.20	0.24	0.21	2.94	2.83	11.89	18.46	1.10	1.15	0.16	0.04	2.88	2.75	0.99	0.91
CaO	9.35	8.30	0.20	0.09	0.16	0.01	0.08	0.00	-	55.84	52.66	19.25	22.33	0.03	-	50.91	56.32
Na_2O	0.07	0.00	7.51	7.56	7.46	0.58	0.25	-	0.02	-	-	0.05	0.02	0.52	0.63	-	-
K_2O	-	0.00	0.71	0.36	0.67	9.71	10.13	0.02	-	-	0.02	0.00	-	10.02	9.95	0.01	-
Totals	97.99	101.19	94.82	94.37	94.74	93.92	93.67	88.14	87.10	59.07	56.07	90.11	95.91	94.31	94.14	54.01	59.34
Si	3.066	3.024	6.074	6.100	6.121	6.840	6.897	5.541	5.660	0.001	0.000	3.091	3.086	6.915	6.813	0.001	-
Al	1.876	1.937	5.840	5.820	5.784	4.365	4.269	5.197	4.853	0.000	0.000	2.157	2.306	4.230	4.343	0.000	0.000
Fe(III)*	-	-	-	-	-	-	-	0.153	0.093	-	-	0.850	0.625	-	-	-	-
Fe(II)	1.506	1.247	0.033	0.037	0.032	0.263	0.310	5.052	3.508	0.024	0.026	-	-	0.312	0.354	0.021	0.022
Mn	0.517	0.929	-	0.004	0.001	0.002	0.002	0.078	0.076	0.005	0.006	0.038	0.028	0.003	0.005	0.009	0.007
Mg	0.211	0.164	0.038	0.046	0.041	0.590	0.572	3.779	5.681	0.028	0.029	0.020	0.005	0.578	0.554	0.026	0.023
Ca	0.816	0.705	0.027	0.013	0.021	0.001	0.011	0.001	-	1.008	0.969	1.746	1.895	0.005	-	0.948	1.016
Na	0.011	0.001	1.869	1.887	1.856	0.151	0.066	-	0.015	-	-	0.008	0.004	0.136	0.166	-	-
K	-	0.000	0.116	0.058	0.110	1.667	1.751	0.009	-	-	0.000	0.000	-	1.720	1.716	0.000	-
H*	-	-	4.000	4.000	4.000	4.000	4.000	16.000	16.000	-	-	1.000	1.000	4.000	4.000	-	-
C*	-	-	-	-	-	-	-	-	-	0.966	0.984	-	-	-	-	0.997	0.965
Totals	8.002	8.007	17.997	17.963	17.966	17.880	17.877	35.810	35.887	2.031	2.015	8.910	8.950	17.897	17.951	2.002	2.034

*Fe(III), CO_2 and H_2O contents calculated stoichiometrically

Table 7 - Representative electron microprobe analyses of mineral phases from the Cignana serpentinite.

	Sample 1503									
	Chlorite		**Diopside**		**Olivine**		**Antigorite**		**Ti-Clinohumite**	
SiO2	33.60	33.59	56.01	55.29	39.99	40.10	42.17	42.22	36.15	36.36
TiO2	0.04	0.00	0.15	0.00	0.00	0.00	0.06	0.00	4.64	4.40
Al2O3	12.90	12.66	0.03	0.00	0.01	0.01	2.44	2.60	0.00	0.00
Cr2O3	0.66	0.74	0.05	0.03	0.01	0.06	0.34	0.31	0.00	0.00
FeO	4.61	4.55	1.87	1.26	13.13	13.04	4.51	4.75	12.65	12.46
MnO	0.03	0.07	0.12	0.05	0.37	0.40	0.07	0.07	0.40	0.49
MgO	34.30	33.76	18.14	17.93	47.96	47.22	37.44	37.69	45.50	45.73
NiO	0.12	0.17	0.11	0.00	0.47	0.40	0.14	0.19	0.32	0.22
CaO	0.02	0.00	25.45	25.67	0.01	0.04	0.01	0.03	0.02	0.04
Na2O	0.00	0.00	0.18	0.09	0.00	0.02	0.00	0.05	0.02	0.03
K2O	0.00	0.00	0.00	0.00	0.00	0.00	0.00	0.02	0.00	0.02
Y2O3	0.00	0.00	0.00	0.00	0.00	0.00	0.00	0.00	0.00	0.00
P2O5	0.03	0.00	0.00	0.00	0.04	0.04	0.00	0.01	0.01	0.00
Totals	86.32	85.55	102.11	100.31	102.00	101.33	87.17	87.93	99.70	99.74
Si	6.435	6.495	1.989	1.996	0.974	0.984	1.982	1.972	3.959	3.973
Ti	0.006	0.000	0.004	0.000	0.000	0.000	0.002	0.000	0.382	0.362
Al	2.916	2.886	0.001	0.000	0.000	0.000	0.135	0.143	0.000	0.000
Cr	0.100	0.114	0.001	0.001	0.000	0.001	0.013	0.011	0.000	0.000
Fe(III)	0.000	0.000	0.001	0.001	0.014	0.008	0.000	0.000	0.000	0.000
Fe(II)	0.780	0.740	0.054	0.038	0.254	0.259	0.177	0.186	1.159	1.139
Mn	0.006	0.012	0.004	0.001	0.008	0.008	0.003	0.003	0.037	0.045
Mg	9.792	9.732	0.961	0.965	1.741	1.728	2.624	2.625	7.429	7.450
Ni	0.019	0.026	0.003	0.000	0.009	0.008	0.005	0.007	0.028	0.019
Ca	0.004	0.000	0.969	0.993	0.000	0.001	0.000	0.001	0.002	0.004
Na	0.000	0.000	0.012	0.006	0.000	0.001	0.000	0.004	0.004	0.006
K	0.000	0.001	0.000	0.000	0.000	0.000	0.000	0.001	0.000	0.002
H	16.000	16.000	0.000	0.000	0.000	0.000	4.000	4.000	0.000	0.000
Totals	36.057	36.006	4.000	4.000	3.000	3.000	8.942	8.953	13.000	13.000

*Fe(III) and H_2O contents calculated stoichiometrically

Table 8 - Representative electron microprobe analyses of mineral phases from Ti–chondrodite and Ti–clinohumite veins hosted within Cignana serpentinite.

	Sample 1402						**Sample 1502**								**Sample 1507**							
	Chlorite		**Ti-Chondrodite**		**Ti-Clinohumite**		**Chlorite**		**Diopside**		**Olivine**		**Ti-Clinohumite**		**Chlorite**		**Diopside**		**Olivine**		**Ti-Clinohumite**	
SiO2	33.83	33.74	32.42	32.60	35.70	35.86	33.68	34.25	55.20	55.55	40.03	39.88	35.65	35.88	33.73	35.05	55.43	55.50	40.01	40.00	35.47	35.31
TiO2	0.00	0.02	8.85	8.55	5.13	5.11	0.04	0.00	0.04	0.00	0.00	0.00	5.03	4.62	0.10	0.20	0.02	0.00	0.13	0.09	4.91	4.92
Al2O3	13.12	13.44	0.01	0.03	0.00	0.00	13.04	13.42	0.03	0.01	0.00	0.01	0.00	0.02	13.61	10.90	0.05	0.17	0.00	0.02	0.00	0.02
Cr2O3	0.35	0.27	0.00	0.00	0.03	0.03	0.05	0.38	0.00	0.00	0.04	0.01	0.00	0.00	0.12	0.04	0.02	0.09	0.05	0.00	0.02	0.00
FeO	4.92	4.85	12.88	12.73	12.63	12.34	5.17	5.16	1.34	1.32	13.77	13.75	13.81	13.73			1.96	2.87				
MnO	0.05	0.04	0.51	0.43	0.32	0.33	0.02	0.00	0.13	0.15	0.54	0.49	0.58	0.63	5.63	5.15	0.09	0.15	14.03	13.11	16.54	16.93
MgO	34.25	33.49	42.79	42.52	45.83	45.53	32.96	32.91	17.65	17.56	46.08	45.81	43.01	43.49	0.11	0.09	17.28	16.47	0.66	0.50	0.66	0.66
NiO	0.16	0.10	0.14	0.10	0.19	0.16	0.28	0.23	0.00	0.01	0.31	0.26	0.16	0.32	32.53	33.79	0.05	0.06	45.17	46.15	40.95	40.66
CaO	0.00	0.00	0.05	0.01	0.00	0.01	0.01	0.00	25.45	25.47	0.00	0.00	0.00	0.01	0.18	0.16	24.92	24.05	0.18	0.24	0.22	0.12
Na2O	0.01	0.00	0.03	0.01	0.00	0.03	0.03	0.03	0.06	0.06	0.01	0.01	0.02	0.01	0.02	0.00	0.27	0.70	0.00	0.02	0.02	0.00
K2O	0.04	0.02	0.02	0.00	0.01	0.01	0.01	0.00			0.00	0.00	0.02	0.00	0.03	0.00	0.00	0.01	0.00	0.00	0.02	0.00
Totals	86.73	86.03	97.70	97.00	99.84	99.44	85.28	86.39	99.90	100.15	100.78	100.22	98.28	98.71	86.07	85.39	100.08	100.07	100.23	100.14	98.82	98.64
Si	6.452	6.481	1.986	2.010	3.904	3.939	6.531	6.544	2.003	2.009	0.992	0.994	4.003	4.003	6.491	6.779	2.010	2.017	1.000	0.996	4.014	4.009
Ti	0.000	0.002	0.408	0.396	0.422	0.422	0.006	0.000	0.001	0.000	0.000	0.000	0.425	0.388	0.014	0.029	0.000	0.000	0.002	0.002	0.418	0.420
Al	2.953	3.045	0.000	0.002	0.001	0.000	2.983	3.028	0.001	0.000	0.000	0.000	0.000	0.003	3.087	2.485	0.002	0.007	0.000	0.001	0.000	0.003
Cr	0.053	0.041	0.000	0.000	0.003	0.003	0.008	0.058	0.000	0.000	0.001	0.000	0.000	0.000	0.018	0.007	0.001	0.003	0.001	0.000	0.002	0.000
Fe(III)	0.000	0.030	0.000	0.000	0.000	0.000	0.031	0.093	0.000	0.000	0.004	0.003	0.000	0.000	0.060	0.062	0.000	0.000	0.000	0.001	0.000	0.000
Fe(II)	0.821	0.749	0.660	0.656	1.155	1.134	0.807	0.732	0.041	0.040	0.281	0.283	1.297	1.281	0.846	0.771	0.059	0.087	0.293	0.272	1.565	1.608
Mn	0.008	0.007	0.027	0.022	0.029	0.031	0.003	0.000	0.004	0.005	0.011	0.010	0.055	0.060	0.019	0.014	0.003	0.005	0.014	0.010	0.063	0.064
Mg	9.738	9.590	3.908	3.908	7.470	7.456	9.528	9.373	0.955	0.947	1.703	1.703	7.199	7.233	9.331	9.742	0.934	0.892	1.683	1.713	6.909	6.883
Ni			0.007	0.005	0.016	0.014	0.044	0.035	0.000	0.000	0.006	0.005	0.014	0.028	0.028	0.025	0.001	0.002	0.004	0.005	0.020	0.011
Ca	0.025	0.015	0.003	0.001	0.000	0.001			0.989	0.987	0.000	0.000	0.000	0.001	0.003	0.001	0.968	0.937	0.000	0.001	0.002	0.000
Na			0.000	0.000	0.000	0.000	0.002	0.001	0.004	0.004	0.000	0.000	0.004	0.003	0.024	0.003	0.019	0.050	0.000	0.000	0.005	0.000
K			0.000	0.000	0.000	0.000	0.020	0.025	0.000	0.001	0.000	0.000	0.003	0.000	0.009	0.000	0.000	0.000	0.000	0.000	0.000	0.002
H	16.000	16.000	0.000	0.000	0.000	0.000	16.000	16.000	0.000	0.000	0.000	0.000	0.000	0.000	16.000	16.000	0.000	0.000	0.000	0.000		
Totals	36.050	35.961	7.000	7.000	13.000	13.000	35.968	35.888	3.998	3.993	3.000	3.000	13.000	13.000	35.929	35.917	3.998	4.000	2.997	3.000	13.000	13.000

*Fe(III) and H_2O contents calculated stoichiometrically

Table 9 - Representative electron microprobe analyses of mineral phases from the Zermatt serpentinite.

	Sample ZSG1406															
	Olivine				**Antigorite**				**Ti-Clinohumite**				**Ti-Chondrodite**			
SiO2	42.21	42.12	42.11	42.42	43.57	44.53	42.57	43.35	37.90	37.88	38.13	38.75	33.85	34.22	34.66	34.81
TiO2	0.04	0.03	0.08	0.00	0.05	0.00	0.00	0.05	2.43	3.09	2.93	2.62	7.35	7.02	7.06	7.01
Al2O3	0.02	0.00	0.00	0.00	1.55	1.52	1.22	1.44	0.01	0.00	0.03	0.02	0.01	0.00	0.00	0.03
Cr2O3	0.00	0.00	0.00	0.04	0.04	0.01	0.07	0.09	0.00	0.00	0.00	0.00	0.04	0.00	0.07	0.00
FeO	3.25	2.43	3.20	3.25	1.88	1.75	1.62	1.94	3.15	2.96	2.89	2.81	3.48	3.64	3.44	3.48
MnO	0.40	0.45	0.48	0.57	0.02	0.04	0.00	0.07	0.44	0.53	0.42	0.52	0.72	0.56	0.65	0.65
MgO	54.88	55.06	55.03	54.87	39.98	39.61	39.94	39.90	53.37	54.51	53.94	54.47	50.54	51.02	50.99	51.15
NiO	0.08	0.08	0.05	0.08	0.07	0.06	0.04	0.13	0.16	0.04	0.01	0.07	0.05	0.04	0.11	0.05
CaO	0.00	0.00	0.02	0.00	0.00	0.00	0.00	0.01	0.00	0.02	0.01	0.01	0.00	0.01	0.02	0.02
Totals	100.88	100.18	100.97	101.24	87.17	87.52	85.46	86.98	97.46	99.03	98.36	99.27	96.04	96.52	96.99	97.20
Si	0.996	0.997	0.992	0.998	2.016	2.046	2.009	2.013	4.024	3.957	4.011	4.036	2.002	2.011	2.029	2.032
Ti	0.001	0.001	0.001	0.000	0.002	0.000	0.000	0.002	0.194	0.243	0.232	0.205	0.327	0.310	0.311	0.308
Al	0.000	0.000	0.000	0.000	0.085	0.083	0.068	0.079	0.001	0.000	0.003	0.002	0.000	0.000	0.000	0.002
Cr	0.000	0.000	0.000	0.001	0.001	0.000	0.003	0.003	0.000	0.000	0.000	0.000	0.002	0.000	0.003	0.000
Fe(III)	0.000	0.000	0.001	0.000	0.000	0.000	0.000	0.000	0.000	0.000	0.000	0.000	0.000	0.000	0.000	0.000
Fe(II)	0.064	0.048	0.062	0.064	0.073	0.067	0.064	0.075	0.280	0.259	0.254	0.245	0.172	0.179	0.168	0.170
Mn	0.008	0.009	0.010	0.011	0.001	0.001	0.000	0.003	0.040	0.047	0.038	0.046	0.036	0.028	0.032	0.032
Mg	1.930	1.943	1.933	1.924	2.758	2.713	2.810	2.763	8.448	8.489	8.459	8.458	4.457	4.469	4.450	4.452
Ni	0.002	0.002	0.001	0.002	0.003	0.002	0.002	0.005	0.014	0.003	0.001	0.006	0.002	0.002	0.005	0.002
Ca	0.000	0.000	0.000	0.000	0.000	0.000	0.000	0.001	0.000	0.002	0.001	0.002	0.000	0.001	0.001	0.001
H	0.000	0.000	0.000	0.000	4.000	4.000	4.000	4.000	13.000	13.000	13.000	13.000	7.000	7.000	7.000	7.000
Totals	3.000	3.000	3.000	3.000	8.939	8.913	8.956	8.944	8.780	8.797	8.753	8.755	4.668	4.678	4.656	4.657

*Fe(III) and H_2O contents calculated stoikiometrically

Table 10 - Representative laser ablation in–situ trace element analyses of mineral phases from the UHP eclogite and metasediments of the Lago di Cignana Unit. All data are reported in μg/g.

	Sample LCG1401						**Sample LCG1414**				**Sample LCG1415**			
	Garnet		**Omphacite**		**Rutile**		**Garnet**		**White Mica**		**Garnet**		**White Mica**	
Li	1.05	1.08	64	61	<0.195	<0.3	2.79	5.3	45	47	20.8	19.8	57	55
Be	<1.21	<1.09	2.04	1.89	<0.218	<0.55	<0.35	<0.34	6.2	7.1	<0.076	<0.292	6.4	6.7
B	<0.39	<0.37	0.7	0.64	<0.26	<0.33	<0.201	<0.2	111	109	0.089	<0.143	100	104
Sc	62	77	27.1	24.1	1.96	1.04	87	29.8	2.06	2.02	75	231	2.07	2.14
V	45	51	340	313	1020	960	11.5	18.8	231	234	30.7	34	220	220
Cr	49	49	33	74	202	252	40	86	122	116	63	59	104	160
Co	27.8	44	21.6	14.6	0.0265	<0.0246	201	189	67	67	107	65	31.4	34
Ni	<0.93	0.98	142	129	15	10.8	2.99	5.2	420	440	1.15	1.41	131	141
Cu	<0.238	0.35	13.3	9.6	1.7	1.37	29.4	19	2.2	1.85	0.315	0.153	2.78	0.78
Zn	56	65	84	76	1.08	0.97	165	216	193	186	108	159	166	184
As	<0.094	<0.093	0.032	0.038	<0.047	<0.045	94	19.4	0.171	0.122	0.0261	<0.0261	0.0216	0.0215
Rb	0.102	<0.0295	0.094	0.0218	<0.0182	<0.0156	<0.022	0.08	430	430	0.015	0.0229	400	420
Sr	0.063	0.064	22.8	23.4	4.1	4.5	0.018	0.0143	8.6	8.3	0.0112	0.0182	19.9	20.6
Y	450	218	0.256	0.4	0.309	0.308	91	146	0.083	0.074	180	302	0.04	0.039
Zr	16.3	7.7	0.55	0.68	55	48	0.34	0.66	0.042	0.051	1.59	51	0.0245	0.023
Nb	<0.019	0.042	<0.0033	<0.0052	275	308	<0.0122	<0.0104	0.89	0.86	<0.0032	0.211	2.2	1.48
Mo	0.39	0.226	<0.0271	<0.043	10.1	6.5	13.2	9.1	<0.093	<0.085	0.281	0.96	<0.0203	<0.0183
Cd	0.73	0.64	0.168	0.126	<0.081	0.167	<0.153	<0.122	<0.168	<0.155	<0.037	<0.142	<0.0266	0.0303
Sb	<0.117	<0.115	0.0251	<0.036	1.47	1.09	<0.078	<0.07	<0.085	<0.079	<0.0124	<0.047	0.0159	0.0151
Cs	<0.0143	<0.0137	0.0211	<0.0035	<0.0108	<0.0094	<0.0137	<0.0145	21.8	22.1	<0.00198	<0.0076	26.3	28.2
Ba	<0.122	<0.116	0.144	0.079	<0.066	<0.08	<0.09	<0.1	920	940	<0.0142	<0.055	800	810
La	<0.0123	<0.0144	0.0061	0.0127	<0.0083	0.0167	<0.0083	<0.0081	0.0186	0.026	<0.00187	<0.0072	0.0055	0.0066
Ce	<0.0181	<0.0173	0.042	0.087	<0.007	0.075	0.0045	<0.0103	0.045	0.039	0.0043	<0.0093	0.00123	0.00156
Pr	<0.0142	<0.0136	0.0118	0.0276	0.0035	<0.0109	<0.0077	<0.0089	<0.0087	<0.0079	0.00292	<0.0071	<0.00131	<0.00115
Nd	<0.071	0.085	0.152	0.257	<0.0135	<0.047	<0.044	<0.035	<0.05	<0.045	0.164	0.073	<0.0097	<0.0086
Sm	0.39	0.48	0.112	0.201	<0.046	<0.056	0.149	0.52	<0.0187	0.0231	2.15	0.82	<0.00282	<0.00215
Eu	0.63	0.56	0.068	0.087	<0.0048	<0.0112	0.18	0.53	<0.0134	<0.012	2	0.83	0.0035	0.0035
Gd	6.7	6.5	0.194	0.311	<0.047	<0.039	1.99	6.6	<0.07	<0.064	26.4	14.6	<0.0094	<0.0082
Tb	4.3	3.5	0.0263	0.048	<0.0054	<0.0091	0.97	2.6	<0.00266	0.00246	6.6	6.6	<0.00127	<0.00111
Dy	63	39	0.095	0.12	<0.037	<0.051	11.3	21.5	<0.0147	<0.0123	41	62	<0.0071	<0.0062
Ho	17.6	8.7	0.0089	0.0134	<0.00255	<0.006	2.95	4.2	<0.00292	<0.00244	6.5	11.4	<0.00045	0.00063
Er	58	24.7	0.013	0.037	<0.0115	<0.0271	10.4	10.3	<0.033	<0.0293	13.7	25.6	<0.00206	<0.00157
Tm	9.1	3.2	<0.00238	<0.0038	<0.006	<0.0102	1.57	1.12	<0.00291	0.0036	1.32	3.15	<0.00045	<0.00035
Yb	66	23.3	<0.0159	0.039	0.0192	<0.041	12	7.1	<0.0191	<0.016	7.4	21.4	<0.00294	<0.00224
Lu	11	4.2	<0.0043	<0.0068	<0.00285	<0.01	1.71	0.92	<0.00312	<0.00261	1.17	4	<0.00049	<0.00037
Hf	0.43	0.181	0.045	0.063	2.41	2	<0.0296	0.0114	<0.033	<0.0301	0.0265	1.64	<0.0079	<0.0071
Ta	<0.0207	<0.0199	<0.00264	<0.0042	16.6	18.5	<0.0068	<0.0085	0.0083	0.0136	<0.00168	0.0262	0.0159	0.0226
W	<0.0225	<0.0207	<0.0157	<0.0248	1.06	1.93	<0.0101	<0.027	1.48	1.34	<0.00214	0.0155	1.39	1.23
Pb	<0.058	<0.06	0.108	0.088	<0.04	<0.047	<0.038	<0.04	3.9	3.8	<0.0117	<0.045	13.8	14.6
Bi	<0.0314	<0.0303	0.0166	0.0121	<0.0151	<0.0183	<0.0175	<0.0175	<0.0193	<0.0177	0.0046	<0.015	0.0043	0.0045
Th	<0.0141	<0.0134	<0.0038	<0.006	<0.0032	<0.011	<0.0045	<0.004	0.0187	0.0295	<0.00229	0.049	0.0037	0.00215
U	0.0236	<0.013	0.0041	<0.0038	1.5	0.148	0.0094	<0.0142	0.0075	<0.0049	0.00242	0.192	<0.00101	<0.00089

Table 11 - Representative laser ablation in–situ trace element analyses of mineral phases from the Cignana serpentinite. All data are reported in µg/g.

	Sample ZSG1403									
	Antigorite		**Ti-Clinohumite**		**Diopside**		**Olivine**		**Magnetite**	
Li	0.0074	<0.0271	2.29	3.12	0.299	0.242	2.6	1.12	1.28	0.9
Be	0.081	0.08	<0.9	<0.57	5.1	5	<0.0205	<0.078	<0.293	<0.142
B	5.1	4.9	7.1	3.3	0.67	0.75	1.63	9.4	0.136	<0.063
Sc	11	9.8	4.1	3.5	25.1	23	1.25	2.13	1.71	1.9
V	48	59	20.4	27.3	5.1	5.2	0.103	0.053	930	960
Cr	2190	2270	30.8	48	68	50	1.81	1.55	39000	32000
Co	57	61	206	211	14.5	14.7	198	208	216	219
Ni	1120	1360	2490	2480	174	177	2830	2770	2740	2750
Cu	2.31	2.06	2.05	2.28	0.85	0.86	1.98	2.11	0.09	<0.042
Zn	46	41	123	120	8	7.8	98	99	360	247
As	0.065	0.169	<0.109	<0.091	0.032	<0.0283	0.009	0.0257	0.054	0.0142
Rb	<0.00276	0.00284	<0.035	<0.0272	<0.0073	0.0109	0.00263	<0.0041	<0.0083	<0.0043
Sr	0.037	0.049	0.192	0.25	118	141	0.00145	0.0117	0.092	0.036
Y	0.47	0.37	0.153	0.143	39	40	0.01	0.281	0.128	0.0056
Zr	0.11	0.159	5.4	2.86	0.188	0.186	0.0089	0.0242	0.72	1.1
Nb	0.069	0.091	94	77	0.0078	0.0272	0.089	0.126	0.6	0.52
Mo	0.0255	0.0274	0.58	0.291	<0.043	0.039	0.202	0.157	2.18	1.87
Cd	0.0308	0.085	<0.246	<0.204	0.145	0.129	0.159	0.046	0.079	0.039
Sb	0.041	0.058	<0.138	<0.129	<0.038	<0.035	0.0122	0.0288	0.054	<0.0191
Cs	<0.00116	<0.00182	0.01	<0.0205	<0.0049	<0.0042	<0.00162	<0.00255	<0.0059	<0.00302
Ba	<0.0123	0.0127	<0.11	<0.098	<0.036	<0.0306	<0.00285	<0.0216	0.23	<0.0162
La	0.032	0.039	0.035	0.0287	1.68	1.85	0.00069	0.0246	0.07	0.0036
Ce	0.122	0.139	0.0259	0.066	7.6	8.2	<0.00141	0.0157	0.056	0.0057
Pr	0.0096	0.0108	<0.0184	<0.0124	1.28	1.29	<0.00083	0.0042	0.0079	<0.00254
Nd	0.037	0.037	0.0305	<0.057	6.3	6.2	<0.00165	0.0203	0.042	0.0034
Sm	0.0161	0.0102	<0.074	<0.0236	2.37	2.4	<0.0056	0.0035	<0.0291	<0.0143
Eu	0.0033	0.0039	<0.04	<0.0245	0.87	0.93	<0.00056	<0.00094	0.0044	0.00142
Gd	0.0278	0.0177	<0.0249	<0.086	3.6	3.7	<0.0073	0.0036	0.0154	<0.00281
Tb	0.004	0.005	<0.0104	0.0049	0.73	0.79	<0.001	<0.00125	0.00127	<0.00039
Dy	0.058	0.035	<0.059	<0.053	5.8	6.2	<0.0044	0.0131	0.0071	<0.00215
Ho	0.0135	0.0139	0.0098	0.0069	1.37	1.45	<0.00145	0.0081	0.0037	<0.00166
Er	0.066	0.064	0.0191	<0.06	4.6	4.7	<0.004	0.072	<0.023	<0.0116
Tm	0.0147	0.0117	<0.0213	0.0108	0.57	0.59	0.00174	0.0314	0.00139	<0.00042
Yb	0.162	0.118	0.223	0.09	3.2	3.4	0.0294	0.51	<0.0089	0.0059
Lu	0.04	0.0278	0.032	0.032	0.31	0.33	0.0099	0.144	<0.0047	<0.00233
Hf	0.0051	0.0111	0.107	0.036	0.0083	0.0095	<0.00114	<0.0052	0.092	0.075
Ta	0.00294	0.0073	6.9	6.4	<0.0034	0.0033	0.0036	0.0061	0.046	0.044
W	0.007	<0.0061	0.7	0.18	<0.0136	<0.0115	<0.00133	<0.00222	<0.016	<0.0076
Pb	0.0197	0.0073	<0.09	<0.074	0.4	0.41	0.0079	0.0093	<0.0222	<0.0119
Bi	0.0069	0.0191	<0.032	<0.0295	<0.0094	<0.0084	0.0253	0.0043	0.0088	0.0045
Th	0.0235	0.043	<0.0157	<0.005	0.0314	0.05	<0.00041	<0.00188	0.0064	0.00164
U	<0.00106	0.0035	<0.0132	<0.0119	<0.0037	0.0038	<0.00043	<0.00225	<0.0069	<0.0034

Table 12 - Representative laser ablation in–situ trace element analyses of mineral phases from Ti–chondrodite and Ti–clinohumite veins hosted in the Cignana serpentinite. All data are reported in µg/g.

	Sample ZSG1402								**Sample ZSG1502**							
	Ti-clinohumite		**Apatite**		**Diopside**		**Chlorite**		**Ti-clinohumite**		**Olivine**		**Antigorite**		**Chlorite**	
Li	2.91	3.08	<0.086	<0.193	<0.66	0.48	<0.44	<0.227	4	3.3	4.9	2.81	<0.127	<0.48	<0.18	0.09
Be	<1.31	<1.68	<0.49	<0.249	3.4	4.5	<1.18	<0.61	<0.57	<1.21	<0.67	<0.38	<0.43	<1.6	<0.4	<0.246
B	2.65	2.68	0.65	1.06	<1.28	0.52	0.98	0.87	1.85	2.96	1.16	4.1	2.17	1.83	0.66	0.68
Sc	5.3	5.6	0.47	0.42	36	42	12.2	8.5	3.3	3.4	2.18	1.64	10.2	8.6	6.2	5.6
V	30.4	38	0.54	0.63	9.6	11.6	117	95	25.2	17.9	0.231	0.103	65	56	80	75
Cr	19.8	42	<2.35	<2.36	115	22.1	1050	1380	33	23	4.3	3.9	1680	1830	2520	860
Co	175	175	<0.039	0.058	15.7	14.4	67	67	188	208	223	223	75	68	76	72
Cu	2.25	10.3	<0.186	1	1.04	0.89	1.56	1.22	1.31	0.78	1.19	1.33	1.78	2.87	1.5	1.21
Zn	116	116	<0.45	<0.45	7.9	7.3	36	35	121	140	104	105	46	58	44	32
As	<0.269	<0.294	4.2	3.9	<0.276	<0.097	<0.136	0.071	<0.057	<0.123	0.36	<0.0237	2.42	0.72	0.078	<0.0204
Rb	<0.072	<0.083	0.274	0.266	<0.094	<0.037	<0.05	<0.0255	<0.0197	<0.042	<0.0237	<0.0128	0.093	<0.075	<0.0142	<0.0092
Sr	0.65	0.7	2440	2500	170	183	0.064	0.052	0.147	0.118	0.118	0.291	0.57	0.37	0.08	0.042
Y	0.52	0.54	2270	2570	72	83	0.0276	0.071	0.141	0.075	0.032	0.307	0.62	0.5	0.0135	0.0127
Zr	4.2	2.33	0.89	0.92	0.243	0.32	0.087	0.09	3.2	5.3	<0.0198	0.125	0.85	0.28	0.046	0.082
Nb	140	190	0.89	0.47	<0.041	0.0133	<0.0251	0.058	14.1	13.8	0.0279	0.079	0.033	<0.037	0.011	<0.0043
In	<0.0288	<0.035	<0.0118	<0.0154	<0.0255	<0.0161	0.0305	0.0271	<0.0089	<0.019	<0.0095	<0.0054	0.0148	<0.0259	0.0147	0.0144
Sn	<0.27	0.43	<0.097	<0.095	<0.271	0.164	2.86	1.49	0.064	<0.136	<0.082	<0.043	0.144	<0.194	0.248	0.208
Sb	<0.305	<0.33	<0.106	<0.103	<0.308	<0.117	<0.151	<0.078	<0.057	<0.122	<0.059	<0.032	0.148	<0.139	<0.036	<0.0234
Cs	<0.055	<0.064	<0.0211	<0.0218	<0.046	<0.0205	<0.033	<0.0167	<0.0144	<0.0307	<0.0124	<0.0069	0.0105	<0.035	<0.0074	<0.0049
Ba	0.37	0.63	<0.165	0.134	<0.39	0.118	<0.235	<0.12	<0.0314	<0.067	<0.126	<0.07	0.234	<0.225	<0.076	<0.033
La	0.279	0.099	940	890	3.8	4.7	<0.041	<0.0211	<0.0042	<0.009	<0.0117	0.0173	0.0137	0.049	<0.007	<0.0055
Ce	0.61	0.217	2460	2260	17.7	19.1	<0.0254	<0.013	0.0049	<0.0095	0.0069	0.036	0.085	0.159	<0.00284	<0.0046
Pr	0.037	<0.038	288	264	3.2	3.4	<0.0068	<0.0034	<0.0034	<0.0072	<0.0035	0.00267	0.0114	0.032	0.00238	<0.0035
Nd	0.38	<0.212	1240	1140	19	17.9	<0.104	<0.053	<0.064	<0.136	<0.054	<0.0309	0.075	0.06	<0.032	<0.0252
Sm	<0.198	<0.243	304	281	7.3	6.9	<0.043	<0.0218	<0.0226	<0.048	<0.062	<0.036	<0.042	<0.158	<0.037	<0.0234
Eu	<0.055	<0.068	50	49	1.49	1.41	<0.0121	<0.0061	0.0073	<0.0141	<0.007	<0.0047	<0.0146	<0.057	<0.0042	<0.0027
Gd	<0.195	<0.24	360	360	9.6	10	<0.044	<0.0219	<0.0227	<0.048	<0.062	<0.036	<0.042	<0.158	<0.037	<0.0234
Tb	<0.0254	<0.0312	57	55	1.65	1.81	<0.0153	<0.0078	0.0034	<0.0066	<0.0033	<0.00221	0.007	<0.0212	<0.00197	<0.00126
Dy	0.051	0.099	360	370	12.1	13.5	<0.0229	<0.0115	<0.034	<0.073	<0.0137	0.034	0.056	<0.088	<0.0083	<0.0053
Ho	<0.032	<0.038	71	81	2.27	2.66	<0.0157	<0.008	<0.0033	0.0077	0.0038	0.0085	0.0178	0.0131	<0.00206	<0.0033
Er	0.076	<0.075	204	249	6.6	8.3	<0.07	<0.036	0.0273	<0.0316	0.0171	0.043	0.106	0.074	<0.0094	0.0088
Tm	0.0203	<0.016	25.4	32	0.73	1.05	0.0061	<0.00277	<0.0081	<0.0173	<0.0107	0.008	0.0103	<0.0301	<0.0064	<0.0051
Yb	0.38	0.5	144	186	4.7	6.3	<0.096	<0.049	0.145	<0.141	0.071	0.14	0.106	<0.135	<0.033	0.021
Lu	0.105	0.104	18.1	22.7	0.52	0.66	0.0128	0.0215	0.0189	0.038	0.036	0.0281	0.035	<0.0219	0.0055	0.0039
Hf	<0.087	<0.107	0.0208	<0.033	<0.034	0.0172	<0.068	<0.035	0.069	0.111	<0.039	<0.0221	0.041	<0.03	<0.0236	<0.0115
Ta	7.5	12.2	0.0116	0.0147	<0.0103	<0.0212	<0.0061	<0.00305	0.72	0.79	<0.0095	<0.0055	<0.0082	<0.033	<0.0057	<0.00139
W	0.096	0.197	0.261	0.136	<0.045	<0.057	<0.106	<0.054	<0.0154	<0.033	0.047	0.149	<0.0137	<0.041	<0.0249	<0.0061
Tl	<0.073	<0.087	<0.0211	<0.0273	<0.046	<0.0261	<0.033	<0.017	<0.0169	<0.036	<0.0151	<0.0087	<0.0091	<0.033	<0.0091	<0.007
Pb	<0.134	<0.156	1.87	1.17	0.9	0.69	<0.088	<0.045	<0.046	<0.098	<0.0274	<0.0153	0.0213	<0.078	<0.0164	<0.0142
Bi	<0.083	<0.096	<0.0265	0.036	<0.101	<0.05	<0.05	<0.0258	<0.0047	<0.01	<0.0128	<0.0073	<0.0115	<0.046	<0.0077	<0.006
Th	<0.085	<0.102	69	76	<0.0266	0.08	<0.0154	<0.0077	<0.0045	<0.0096	<0.0127	<0.0073	<0.0092	<0.035	<0.0076	<0.00194
U	<0.044	<0.057	10.2	16.2	<0.0225	<0.0253	<0.032	<0.0164	<0.0042	<0.0089	<0.0045	<0.00307	<0.0069	<0.0246	<0.00274	<0.0034

Table 13 - Representative laser ablation in–situ trace element analyses of mineral phases from the Zermatt serpentinite. All data are reported in µg/g.

	ZSG1406										
	Serpentine			**Ti-Clinohumite**			**Diopside**			**Magnetite**	
Li	<0.0208	<0.0106	<0.0067	0.215	0.5	1.32	1.07	1.02	1.34	0.35	<0.34
Be	<0.051	<0.044	<0.039	<0.037	<0.068	<0.077	<0.075	<0.086	<0.042	<0.4	<0.41
B	23.3	32	9.9	22.4	21.5	18.9	24.1	23.1	16.4	1.46	0.86
Sc	12.4	12.5	11.3	14.2	29.7	65	7.8	8.6	90	1.03	0.85
V	25.9	25	23.2	19.5	14.8	18.2	17.4	18.2	18.2	198	203
Cr	1640	2630	530	90	60	104	298	330	141	4000	3500
Co	9	8.6	8.2	56	50	37	27.1	31	17.7	86	84
Ni	286	213	210	550	480	380	410	480	320	1920	1690
Cu	9.5	4.4	3.7	2.79	2.52	2.55	46	19.9	2.4	3.2	0.97
Zn	19.5	19.1	15.6	57	50	42	34	33	45	138	134
As	0.51	0.53	0.235	0.0139	<0.0048	0.0078	0.81	0.89	0.0075	0.051	<0.045
Rb	0.0045	<0.00312	<0.00257	<0.0026	<0.0048	<0.0041	<0.0043	<0.0049	<0.00182	<0.0236	<0.0291
Sr	0.0164	0.0225	0.014	0.198	0.205	0.36	0.109	0.098	0.4	0.035	0.044
Y	0.311	0.208	0.221	0.087	0.117	0.12	1.01	1.07	0.138	0.174	0.15
Zr	0.5	0.41	0.295	4.9	4.3	8.3	2.08	2.04	3.9	0.91	0.313
Nb	0.0208	0.0205	0.0195	0.86	1.14	2.93	0.53	0.41	1.87	0.073	0.041
Mo	0.0285	0.0238	0.0289	0.283	0.289	0.36	0.191	0.205	0.39	0.271	0.34
Cd	0.0226	0.026	0.1	0.034	0.0297	<0.023	0.0292	<0.0256	0.0296	<0.182	<0.226
Sb	0.17	0.167	0.096	0.0117	<0.0095	<0.009	0.116	0.122	0.0052	<0.064	<0.089
Cs	<0.00221	<0.00189	<0.0021	<0.00159	<0.00293	<0.00193	0.0047	0.0039	<0.00143	<0.0206	<0.025
Ba	<0.0106	<0.0145	0.0036	0.0311	<0.0212	<0.0044	<0.0294	<0.034	0.01	<0.059	0.038
La	0.006	0.0072	0.0064	0.00249	0.00102	<0.00232	0.047	0.046	<0.00093	<0.0216	<0.0254
Ce	0.0204	0.0154	0.0194	0.0064	0.00163	<0.00202	0.115	0.114	<0.00094	0.033	0.0206
Pr	0.0035	0.0033	0.00274	<0.00093	<0.00172	0.00048	0.0137	0.0152	<0.00091	0.0107	0.005
Nd	0.0153	0.0208	0.0204	0.0104	0.0044	<0.0069	0.108	0.099	<0.00131	0.069	<0.065
Sm	0.0117	0.0113	0.0087	0.0062	<0.01	<0.0081	0.039	0.055	<0.00154	<0.09	<0.099
Eu	0.0032	0.004	<0.00216	<0.00155	<0.00289	<0.00085	0.0095	0.0086	0.00066	<0.0261	<0.0287
Gd	0.0291	0.0154	0.0211	0.009	0.0066	0.0034	0.105	0.099	0.0024	<0.041	0.0265
Tb	0.0038	0.00189	0.0049	0.0012	0.00132	<0.00115	0.0148	0.0167	0.00057	0.0082	0.006
Dy	0.041	0.0174	0.0313	0.006	0.0067	0.0061	0.103	0.143	0.0044	<0.0316	0.027
Ho	0.0105	0.0091	0.0085	0.00219	0.00247	0.00292	0.038	0.042	0.0032	0.0162	0.008
Er	0.043	0.0188	0.0313	0.0095	0.0217	0.0188	0.141	0.116	0.0244	<0.074	<0.085
Tm	0.0055	0.0049	0.0037	0.00227	0.0054	0.0079	0.0273	0.0249	0.0095	<0.0119	<0.0121
Yb	0.054	0.045	0.042	0.0287	0.062	0.105	0.185	0.192	0.131	<0.041	0.035
Lu	0.013	0.0093	0.0065	0.0078	0.0165	0.035	0.043	0.039	0.046	<0.0068	0.0072
Hf	0.028	0.0221	0.01	0.092	0.088	0.164	0.074	0.059	0.084	0.035	<0.0136
Ta	0.00083	0.00136	0.00069	0.0297	0.032	0.099	0.0174	0.0088	0.083	<0.0068	<0.0039
W	0.0078	0.0101	0.0055	0.216	0.0306	0.056	0.34	0.268	0.069	0.0296	0.0172
Pb	0.06	0.0129	0.0165	0.0066	<0.0087	<0.0089	0.0144	0.0229	0.0066	<0.056	<0.071
Bi	0.0062	0.0053	0.0272	0.0173	0.0042	0.0037	<0.0037	<0.0043	0.0082	<0.0226	<0.0266
Th	0.00173	<0.0019	0.0012	<0.000299	<0.00058	<0.0006	<0.00254	0.00299	<0.001	<0.0149	<0.0152
U	<0.00078	<0.00077	0.00147	0.00102	0.00111	0.00138	0.00239	0.00203	0.00073	<0.0096	<0.0105